UNIVERSITY OF LEEDS

Nanostructure engineering for efficient light conversion

Yang Zhou

Submitted in accordance with the requirements for the degree of Doctor of Philosophy

The University of Leeds

Faculty of Engineering and Physical Sciences

School of Electronic and Electrical Engineering

September 2022

Intellectual Property

The candidate confirms that the work submitted is his/her/their own, except where work which has formed part of jointly authored publications has been include. The contribution of the candidate and the other authors to work has been explicitly indicated below. The candidate confirms that appropriate credit has been given within the thesis where reference has been made to the work of others.

Chapter II of Part II is based on work from a jointly authored publication: Inverse-designed semiconductor nanocatalysts for targeted CO_2 reduction in water, by Marco Califano and Yang Zhou, Nanoscale 2021, 13, 10024, where my contribution included performing part of the calculations and the analysis of the results, as well as reviewing the manuscript; Marco Califano's contribution included conceiving and writing the paper, performing part of the calculations, and analysing the results.

Chapter III of Part II is based on work from a jointly authored publication: Decoupling Radiative and Auger Processes in Semiconductor Nanocrystals by Shape Engineering, by Yang Zhou and Marco Califano, The Journal of Physical Chemistry Letters 2021, 12, 9155, where my contribution included performing the calculations, analysing the results and writing the paper; Marco Califano's contribution included conceiving the paper, analysing the results and reviewing/correcting the manuscript.

This copy has been supplied on the understanding that it is copyright material and that no quotation from the thesis may be published without proper acknowledgement.

© 2022 The University of Leeds, Yang Zhou

Acknowledgements

Abstract

In this thesis, I divide my work into two parts: Part I is about the work carried out in collaboration with Nanoco Technologies Ltd, where a study, based on density functional theory (DFT), of the electron transfer during the process of light conversion in luminescent polyoxometalates (POMs) $\{Mo_8O_{26}[C_{18}H_{32}N]_2[C_6H_{16}N]_2\}$ is presented. My calculation results explain the experimental observations, including the electron transfer during the optical absorption and the long lived charged state, well, and I propose a mechanism of the observed high-quantum-yield luminescence in this material. In Part II, a semiempirical pseudopotential method (SEPM) is used to investigate light conversion in: 1) CdTe/CdSe core/arms tetrapods (TPs) (Chapter II), 2) CdTe TPs (Chapter III), and 3) asymmetrical CdTe/CdSe core/arms and CdTe TPs (Chapter IV). My work provides theoretical evidence that, following careful shape engineering, 1) CdTe/CdSe core/arms TPs have the potential to become efficient photocatalytic materials for CO_2 reduction in water, and 2) CdTe TPs may exhibit strong suppression of Auger recombination without compromising the efficiency of radiative recombination, which makes them potentially ideal light-emitting materials. Furthermore, 3) I show that the introduction of geometrical anisotropies in these nanostructures could lead to a further improvement in their light conversion efficiency.

Contents

Part I

Light conversion in

organic-polyoxometalates

Chapter 1

Method

1.1 Density functional theory

Density functional theory (DFT) is an ab initio algorithm utilized to investigate the ground state in many-body systems. It has an advantage over the conventional quantum-chemical approaches based on many-electron wavefunctions in saving computational cost with increasing computational accuracy, which is owed to the charge-density-based solution for the Schrödinger equation [1]. The conventional many-electron time independent Schrödinger equation is represented as (without considering spin):

$$\hat{H}\Psi\left(\mathbf{r_1},\ldots,\mathbf{r_{N_{el}}}\right) = E\Psi\left(\mathbf{r},\ldots,\mathbf{r_{N_{el}}}\right) = [\hat{T} + \hat{V} + \hat{U}]\Psi\left(\mathbf{r},\ldots,\mathbf{r_{N_{el}}}\right), \qquad (1.1.1)$$

where $\hat{T}$ is the kinetic energy operator, $\hat{V}$ is the potential energy operator due to the nuclei, and $\hat{U}$ is the electron-electron interaction energy operator. The coordinates of the electrons are defined by $r_{N_{el}}$ and N_{el} is the number of electrons in the system. The Hamiltonian operator has the following expression in Hartree units:

$$\hat{H}_{el} = \sum_{i=1}^{N_{el}} -\frac{1}{2}\nabla_i^2 + \sum_{i=1}^{N_{el}}\sum_{j=i+1}^{N_{el}} \frac{1}{|\mathbf{r_i} + \mathbf{r_j}|} + \sum_{i=1}^{N_{el}}\sum_{A=1}^{N_{at}} \frac{-Z_A}{|\mathbf{r_i} - \mathbf{R_A}|}, \qquad (1.1.2)$$

where N_{at} is the total number of electrons and nuclei, r_i and R_A are the electronic and nuclear coordinates respectively, and Z_A is the atomic number. The energy of the system is therefore:

$$E_{el} = \int \cdots \int \Psi^* \hat{H}_{el} \Psi d\mathbf{r} \ldots d\mathbf{r_{N_{el}}}$$

$$= \int \Psi^* \left(\sum_{i=1}^{N_{el}} -\frac{1}{2}\nabla_i^2 \right) \Psi d\mathbf{r} + \int \Psi^* \left(\sum_{i=1}^{N_{el}} \sum_{j=i+1}^{N_{el}} \frac{1}{\mathbf{r_i} - \mathbf{r_j}} \right) \Psi d\mathbf{r} + \int \Psi^* \left(\sum_{i=1}^{N_{el}} \sum_{A=1}^{N_{at}} \frac{-Z_A}{\mathbf{r_i} - \mathbf{R_A}} \right) \Psi d\mathbf{r}.$$

$$(1.1.3)$$

In 1964, Hohenberg and Kohn proposed the famous hypothesis (Hohenberg- Kohn Theorem) that provided the framework for DFT [2]:

1. *The external potential $V_{ext}(\mathbf{r})$ is uniquely determined by the particle density $n(\mathbf{r})$.*

2. *The ground state energy is the functional of the particle density $n(\mathbf{r})$, and the particle density that minimises the value of the ground state energy functional is the exact ground-state density $n_0(\mathbf{r})$.*

The energy as a functional of the electron density n is expressed as:

$$E_{el} = F_{HK}[n] + \int V_{ext}(\mathbf{r})n(\mathbf{r})d\mathbf{r} = E_{el}[n] \tag{1.1.4}$$

where V_{ext} is the external potential, and $F_{HK}[n]$, is defined as the universal function, is

$$F_{HK}[n] = E_k[n] + E_{Coul}[n] + E_x[n] + E_c[n], \tag{1.1.5}$$

where $E_k[n]$, $E_{Coul}[n]$, $E_x[n]$, and $E_c[n]$ are the kinetic, Coulomb, exchange, and correlation energies, respectively. According to the variational principle, the ground-state energy E_0 and the corresponding electron density are uniquely determined and calculated by minimising Eq. (1.1.4). And the electron density is normalized to the total number of electrons:

$$\int n(\mathbf{r})d\mathbf{r} = N_{el} \tag{1.1.6}$$

Hence, the Lagrangian functional

$$\Omega_{el}[n] = E_{el}[n] - \mu \left(\int n(\mathbf{r}) d\mathbf{r} - N_{el} \right), \tag{1.1.7}$$

is built to find the ground-state energy E_0. $E_{el}[n]$ reaches its minimum when

$$\frac{\delta \Omega_{el}[n]}{\delta n(\mathbf{r})} = 0, \tag{1.1.8}$$

which leads to

$$\frac{\delta E_{el}}{\delta n(\mathbf{r})} - \mu = 0, \tag{1.1.9}$$

where μ, determined by the electron density and particle energy in the system, is the Lagrange multiplier that is introduced to constrain the number of electrons as N_{el}.

However, only the external potential (potential energy due to the nuclei) in Eq. (1.1.4) could be expressed exactly as a function of the electronic density. The universal functional, the kinetic energy, in particular, is approximated with significant errors due to the lack of an accurate expression. In 1965, Kohn and Sham proposed a fictitious system where the electrons do not interact with each other. This system is defined as having the same electronic density as the interacting system. The advantage of this method is that the kinetic energy of non-interacting electrons is known and can be expressed as functional of the molecular orbitals ψ (the single electron wave functions), and the interaction between electrons is described by the Coulomb interaction in a non-interacting system. To find the electronic density of this factitious system, the total energy functional is written as:

$$E[n] = E_{k,KS}[n] + E_{Coul}[n] + E_{ext}[n] + E_{xc}[n], \tag{1.1.10}$$

where

$$E_{k,KS}[n] = 2 \sum_{j=1}^{N_{el}/2} \int \psi_j^*(\mathbf{r})(-\frac{1}{2}\nabla^2)\psi_j(\mathbf{r})d\mathbf{r}, \tag{1.1.11}$$

$$E_{Coul}[n] = \frac{1}{2} \iint \frac{n(\mathbf{r_i})n(\mathbf{r_j})}{|\mathbf{r_i} - \mathbf{r_j}|}d\mathbf{r_i}d\mathbf{r_j}, \tag{1.1.12}$$

$$E_{ext}[n] = \int V_{ext}(\mathbf{r})n(\mathbf{r})d\mathbf{r}, \tag{1.1.13}$$

$$E_{xc}[n] = (E_k[n] - E_{k,KS}[n]) + (E_{ee}[n] - E_{Coul}[n]), \tag{1.1.14}$$

where E_{ee} is the electron-interaction energy in real system. The electron density is expressed in terms of molecular orbitals for the non-interacting electrons as:

$$n(\mathbf{r}) = \sum_{j=1}^{N_{occ}} |\psi_j(\mathbf{r})|^2. \tag{1.1.15}$$

where N_{occ} is the total number of occupied orbitals. According to the variational theorem and the Lagrangian algorithm, the molecular orbitals that minimise the energy have to satisfy the equation:

$$\frac{\delta \Omega_{KS}[n]}{\delta \psi_j^*(\mathbf{r})} = (\frac{\delta E_{k,KS}}{\delta n} + \frac{\delta E_{Coul}}{\delta n} + \frac{\delta E_{ext}}{\delta n} + \frac{\delta E_{xc}}{\delta n})\psi_j(\mathbf{r}) - \epsilon_j \psi_j(\mathbf{r}) = 0. \tag{1.1.16}$$

Combining Eqs. (1.1.11), (1.1.12) and (1.1.16) gives:

$$\left[-\frac{1}{2}\nabla^2 + \int \frac{n(\mathbf{r_j})}{|\mathbf{r_i} - \mathbf{r_j}|}d\mathbf{r_j} + v_{ext}(\mathbf{r}) + v_{xc}(\mathbf{r}) \right] \psi_j(\mathbf{r}) = \epsilon_j \psi_j(\mathbf{r}). \tag{1.1.17}$$

Here, the only unknown is the local exchange-correlation potential v_{xc}, which could be approximated with the local density approximation (LDA) or the generalised gradient approximation (GGA). This strategy turns Eq. (1.1.17) into a single electron Schrödinger equation that can be solved by self-consistent field (SCF).

1.2   Van der Waals interactions

The method that accounts for the van der Waals (vdW) effect within DFT is the van der Waals density functional (vdW-DF), where an additional functional is added to the correction term of the Kohn-Sham density equation. The new correction term can be simply expressed as:

$$E_c[n] = E_c^0[n] + E_c^{nl}[n], \tag{1.2.1}$$

where $E_c^0[n]$ is local and approximated to the correlation energy obtained from the local density approximation (LDA) method giving:

$$E_c^0[n] \approx E_c^{LDA}[n], \tag{1.2.2}$$

$E_c^{nl}[n]$ is the non-local term that describes the vdW interactions by introducing the long-range effects approximated as[3], [4]:

$$E_c^{nl} \approx \int_0^\infty \frac{du}{4\pi} tr \left[S^2 - \left(\frac{\nabla S \cdot \nabla V}{4\pi e^2} \right)^2 \right],$$ (1.2.3)

where u is the imaginary frequency, V the interelectronic Coulomb interaction, $S \equiv 1 - \epsilon$ and ϵ is the appropriately approximated dielectric function.

Combining the local correlation terms with vdW correction functional in Kohn-Sham equation, the overlapping part need to be subtracted. Then the vdW-DF energy functional was proposed as [3]:

$$E^{VDW-DF}[n] = E^{KS}[n] + E_c^0[n] + E_c^{nl}[n] - E_c^{KS}[n].$$ (1.2.4)

Considering a more accurate description of hydrogen bonds is expected by using GGA rather than LDA [5], the function above could be expressed more accurately as:

$$E^{VDW-DF}[n] = E^{GGA}[n] + E_c^{GGA}[n] + E_c^0[n] + E_c^{nl}[n].$$ (1.2.5)

1.3 Time-dependent density functional theory

Time-dependent density functional theory (TDDFT) is an extension of DFT used to study the excited states by introducing a time-dependent external potential. Similarly to DFT, it is based on two theorems, proposed by Runge and Gross [6]:

1. The external time-dependent potential $V_{ext}(\mathbf{r}, t)$ is a unique function of the time-dependent electron density $n(\mathbf{r}, t)$;

2. If a function A is defined as:

$$A = \int_{t_0}^{t_1} \left\langle i \frac{\partial}{\partial t} - \hat{H}(t)\Psi(t) \right\rangle dt,$$ (1.3.1)

then it can be expressed as a functional of the density as:

$$A[n] = S[n] - \int_{t_0}^{t_1} dt \int d\mathbf{r} \, n(\mathbf{r}, t) V_{ext}(\mathbf{r}, t),$$ (1.3.2)

where $S[n]$ is the universal time-dependent density functional. The variational principle for TDDFT states that only the exact electron density leads to a minimum of $A[n]$. Applying the

Kohn-Sham's *ansatz* to TDDFT yields the following expression for $S[n]$:

$$S[n] = S_0[n] + S_{Coul}[n] + S_{xc}[n], \tag{1.3.3}$$

where S_0 is the functional for non-interacting electrons,

$$S_{Coul}[n] = -\frac{1}{2} \int_{t_0}^{t_1} dt \iint \frac{n(\mathbf{r_i}, t) n(\mathbf{r_j}, t)}{|\mathbf{r_i} - \mathbf{r_j}|} d\mathbf{r_i} d\mathbf{r_j} \tag{1.3.4}$$

is the Coulomb interaction in the time-dependent system for non-interacting electrons, and S_{xc} is the time-dependent exchange-correlation term. Hence, the time-dependent KS potential can be expressed as:

$$
\begin{aligned}
V_{KS}[n](\mathbf{r}, t) &\equiv V_{Coul}(\mathbf{r}, t) + V_{xc}(\mathbf{r}, t) + V_{ext}(\mathbf{r}, t) \\
&\equiv \int \frac{n(\mathbf{r_j}, t)}{|\mathbf{r_i} - \mathbf{r_j}|} d\mathbf{r_j} - \frac{\delta S_{xc}[n]}{\delta n(\mathbf{r}, t)} + V_{ext}(\mathbf{r}, t).
\end{aligned}
\tag{1.3.5}
$$

However, the big challenge remains the approximation of the exchange-correlation term, for which two approaches are mainly used: (i) The most popular is the *Adiabatic* approximation, which defines that the density at a specific time alone determines the XC potential at that time; (ii) the other approximation considers this unknown term as time-independent and equivalent to the one in the ground state. Applying the variational principle with the Lagrangian algorithm, the time-dependent KS equation is defined as:

$$i\frac{\partial}{\partial t}\psi_i(\mathbf{r}) = \left[-\frac{1}{2}\nabla^2 + V_{KS}[n](\mathbf{r}, t) \right] \psi_i(\mathbf{r}) \equiv \hat{H}_{KS}\psi_i(\mathbf{r}), \tag{1.3.6}$$

and the time-dependent density is decided by the time-dependent wavefunctions of valence electrons v in occupied states *occ*:

$$n(\mathbf{r}, t) = \sum_{v \in occ} |\psi_v(\mathbf{r}, t)|^2. \tag{1.3.7}$$

The excited-state energy of the system is calculated through the linear response function, $\tilde{\chi}_{AB}$, which is extracted from TDDFT and many-body perturbation theory [7] as the frequency func-

tion of the incident phonon:

$$\tilde{\chi}_{AB}(\omega) = \sum_{n\in exc} \left[\frac{\langle\Psi_0|\hat{A}|\Psi_{exc}\rangle \langle\Psi_{exc}|\hat{B}|\Psi_0\rangle}{\omega - (E_{exc} - E_0) + i\epsilon} - \frac{\langle\Psi_0|\hat{B}|\Psi_{exc}\rangle \langle\Psi_{exc}|\hat{A}|\Psi_0\rangle}{\omega + (E_{exc} - E_0) + i\epsilon} \right], \qquad (1.3.8)$$

where the subscripts 0 and exc refer to the ground and the excited state respectively. $\hat{A}$ and $\hat{B}$ are one-body operators. From the equation above, the poles of $\tilde{\chi}_{AB}$ are

$$E_{exc} = E_0 \pm (\omega + i\epsilon). \qquad (1.3.9)$$

The time-dependent density matrix is defined as:

$$\hat{\rho}(t) = \sum_{v\in occ} |\psi_v(t)\rangle\langle\psi_v(t)|, \qquad (1.3.10)$$

which can be divided into unperturbed and time-response parts:

$$\hat{\rho}(t) = \hat{\rho}^0 + \hat{\rho}'(t). \qquad (1.3.11)$$

Generally, the time-dependent Kohn-Sham equation also can be separated into unperturbed and time-response parts:

$$\hat{H}_{KS}(t) = \hat{T}_0 + V_{Hxc}^0(\mathbf{r}) + V_{ext}^0(\mathbf{r}) + V_{Hxc}'[\hat{\rho}'](\mathbf{r},t) + V_{ext}'(\mathbf{r},t), \qquad (1.3.12)$$

where $V_{Hxc}'[\hat{\rho}'](\mathbf{r},t)$ is the linear correction to the Hartree-plus-XC potential written as:

$$V_{Hxc}'[\hat{\rho}'](\mathbf{r},t) = \int d\mathbf{r}'dt' \left[\frac{1}{|\mathbf{r}-\mathbf{r}'|} + f_{xc}(\mathbf{r},\mathbf{r}';t-t') \right] n'(\mathbf{r}',t'), \qquad (1.3.13)$$

where f_{xc} is defined as the XC kernel. Eq. (1.3.10) expressed with density matrix reads:

$$i\frac{d\hat{\rho}(t)}{dt} = \left[\hat{H}_{KS}[\hat{\rho}](t), \hat{\rho}(t) \right], \qquad (1.3.14)$$

where $[\bullet, \bullet]$ indicates the commutator. Combining Eqs. (1.3.11), (1.3.12) and (1.3.14) yields:

$$i\frac{d\hat{\rho}'(t)}{dt} = [\hat{H}^0_{KS}, \hat{\rho}'(t)] + [V'_{Hxc}[\hat{\rho}'(t)], \hat{\rho}^0] + [\hat{V}'_{ext}, \hat{\rho}^0]$$

$$= \mathcal{L}\hat{\rho}'(t) + [\hat{V}'_{ext}, \hat{\rho}^0], \tag{1.3.15}$$

where

$$\mathcal{L}\hat{\rho}' = [\hat{H}^0_{KS}, \hat{\rho}'(t)] + [V'_{Hxc}[\hat{\rho}'(t)], \hat{\rho}^0] \tag{1.3.16}$$

defines the Liouvillian operator $\mathcal{L}$. The expression (1.3.15) in frequency domain reads:

$$(\omega - \mathcal{L})\hat{\rho}'(\omega) = [\hat{V}'_{ext}(\omega), \hat{\rho}^0] \tag{1.3.17}$$

The dipole is given as:

$$\mathbf{d}(\omega) = -(\mathbf{r}, \hat{\rho}'(\omega)). \tag{1.3.18}$$

where $(\bullet, \bullet)$ refers to the inner product of two operators. The dynamical polarizability is written as

$$\alpha_{ij}(\omega) \equiv \frac{\partial d_i(\omega)}{\partial E_j(\omega)}, \tag{1.3.19}$$

which, by combining Eqs. (1.3.17) and (1.3.18), becomes:

$$\alpha_{ij}(\omega) = -4\left(\hat{X}_i, (\omega - \mathcal{L})^{-1} \cdot [\hat{X}_j, \hat{\rho}^0]\right), \tag{1.3.20}$$

where $\hat{X}_i$ is the i-th component of the dipole operator. To solve Eq. (1.3.20), the standard batch representation (SBR) [8], [9] is introduced rewriting the equation as:

$$\alpha_{ij}(\omega) = -\left(x_i, (\omega - L)^{-1} \cdot y_j\right), \tag{1.3.21}$$

where x_i, y_j, and L are the SBR for $\hat{X}_i$, $[\hat{X}_j, \hat{\rho}^0]$, and $\mathcal{L}$ in Eq.(1.3.20) respectively, such that:

$$\hat{X}_i \xrightarrow{\text{SBR}} x_i \triangleq \begin{pmatrix} \{\hat{Q}\hat{X}_i\psi^0_v(\mathbf{r})\} \\ \{0\} \end{pmatrix} \tag{1.3.22}$$

$$[\hat{X}_j, \hat{\rho}^0] \xrightarrow{\text{SBR}} y_j \triangleq \begin{pmatrix} \{0\} \\ \{\hat{Q}\hat{X}_j\psi^0_v(\mathbf{r})\} \end{pmatrix} \tag{1.3.23}$$

$$\mathcal{L} \xrightarrow{\text{SBR}} L \triangleq \begin{pmatrix} 0 & D \\ D + 2K & 0 \end{pmatrix} \tag{1.3.24}$$

where $\hat{Q}$ is the projector over the empty-state manifold, and D and K are the super-operators defined as:

$$D \cdot \{a_v(\mathbf{r})\} = \{(\hat{H}^0 - \varepsilon_v^0)a_v(\mathbf{r})\} \tag{1.3.25}$$

$$K \cdot \{a_v(\mathbf{r})\} = \{4\psi_v^0(\mathbf{r}) \sum_{v'} \int \kappa(\mathbf{r}, \mathbf{r}')\psi_{v'}^0(\mathbf{r}')\mathbf{a}_{\mathbf{v}'}(\mathbf{r}')d\mathbf{r}'\}, \tag{1.3.26}$$

where $\kappa(\mathbf{r}, \mathbf{r}')$ refers to the kernel of Hartree-plus -XC energy.

The significant difference between the Turbo-Lanczos and Turbo-Davidson algorithms is that the calculation of the dynamic polarizability based on the former is less memory-consuming as it considers occupied states only [9]. Hence, Turbo-Lanczos is normally applied to large systems where Turbo-Davidson suffers from memory issues. But since it does not include unoccupied states, Turbo-Lanczos cannot provide any information on the specific states involved in an energy transition, while Turbo-Davidson can. The technical details of Turbo-Lanczos and and Turbo-Davidson are presented in Appendix A and B respectively.

Chapter 2

DFT study of octamolybdate-based polyoxometalates

2.1 Introduction

Blue light-emitting materials are in high demand for the display industry, especially organic light-emitting diodes which are widely used in cell phones and television screens nowadays [10], [11]. Although much effort has been put into developing a true-blue light emitter, low efficiency and poor stability are still the bottlenecks for the application of these materials [12]– [14], which are mainly due to the increased number of non-emissive states in wide band-gap semiconductors [15] and the large Stokes shift between the absorption and emission spectra [16], [17]. In addition, higher energy UV excitation typically involves several states, resulting in complicated absorption and emission spectra. Another problem is that the excitation wavelength is energetic enough to cause degradation in many known materials [18]–[20].

One of the most promising materials for blue quantum dots are metal oxides, such as MoO_3. Such materials are usually very stable against moisture and corrosion as well as under UV irradiation. They are also easy to produce in large scale, and, most importantly, produce bright luminescence [21], [22]. And, to meet the typical requirement of practical applications, they need to be shaped into small clusters.

Nanoco Technologies Ltd has developed a series of octamolybdate-based polyoxometalates (POMs) as blue-light luminophores to meet the commercial demand for efficiency and stabil-

ity, where molybdenum oxide and octamolybdate complexes [($MoO_3 \cdot H_2O$) molybdic acid, {$Mo_8O_{26}[C_4H_9NH(C_2H_4OH)_2]_4 \cdot xH_2O$} octamolybdate N-tert-butyldiethanolamine complex, {$Mo_8O26[C_6H_{13}NH_3]_4 \cdot xH_2O$} hexylammonium octamolybdate] were used as the Mo source, and well-known aliphatic alkylamines were employed as secondary ligands due to strong H bonding interactions, increasing the mobility of molybdate in organic solution [23], [24]. Pyridinium salts were added simultaneously with the aliphatic amine as in case of molybdic acid, or in case of pre-ligated molybdenum hexacarbonyl by *in situ* pyridinium generation. Such ligands provide spacing between the octamolybdate clusters, which reduces charge and energy transfer between the latter. This synthesis method allows different pyridinium ligands (with varied length and substitution on both N and C sites on the aromatic ring) to be incorporated into the structure, thus providing different levels of interaction between octamolybdates.

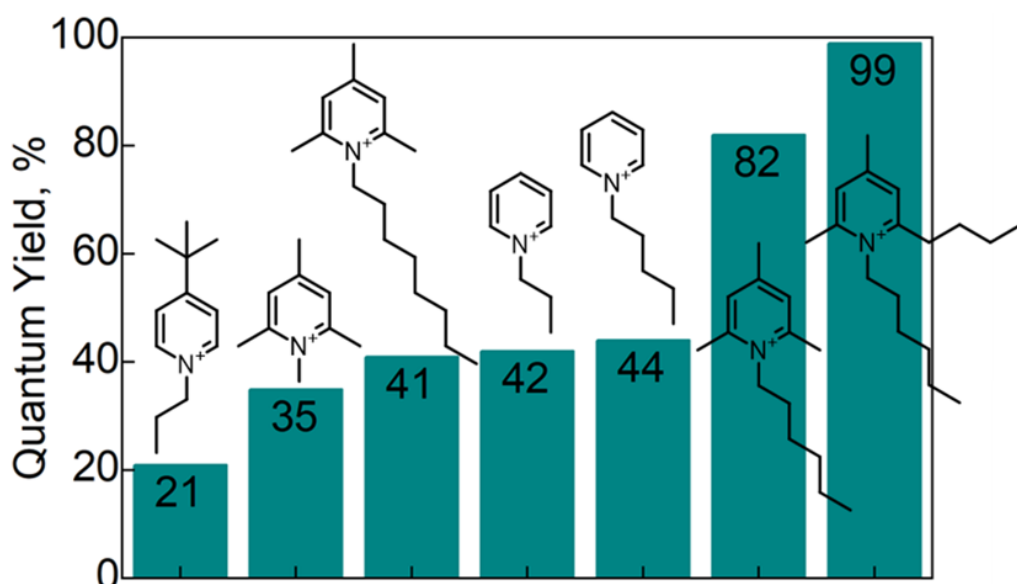Figure 2.1: Quantum yield dependence on the pyridinium ligand molecule under 360 nm excitation [25]

They found that all the samples in solution showed luminescence under 360 nm excitation, with a quantum yield (QY) strongly dependent on the structure of the pyridinium ligands (see Fig. 2.1). Among all the samples, the one with the pyridinium ring coplanar with octamolybdate showed an extremely high QY of 99.9%.
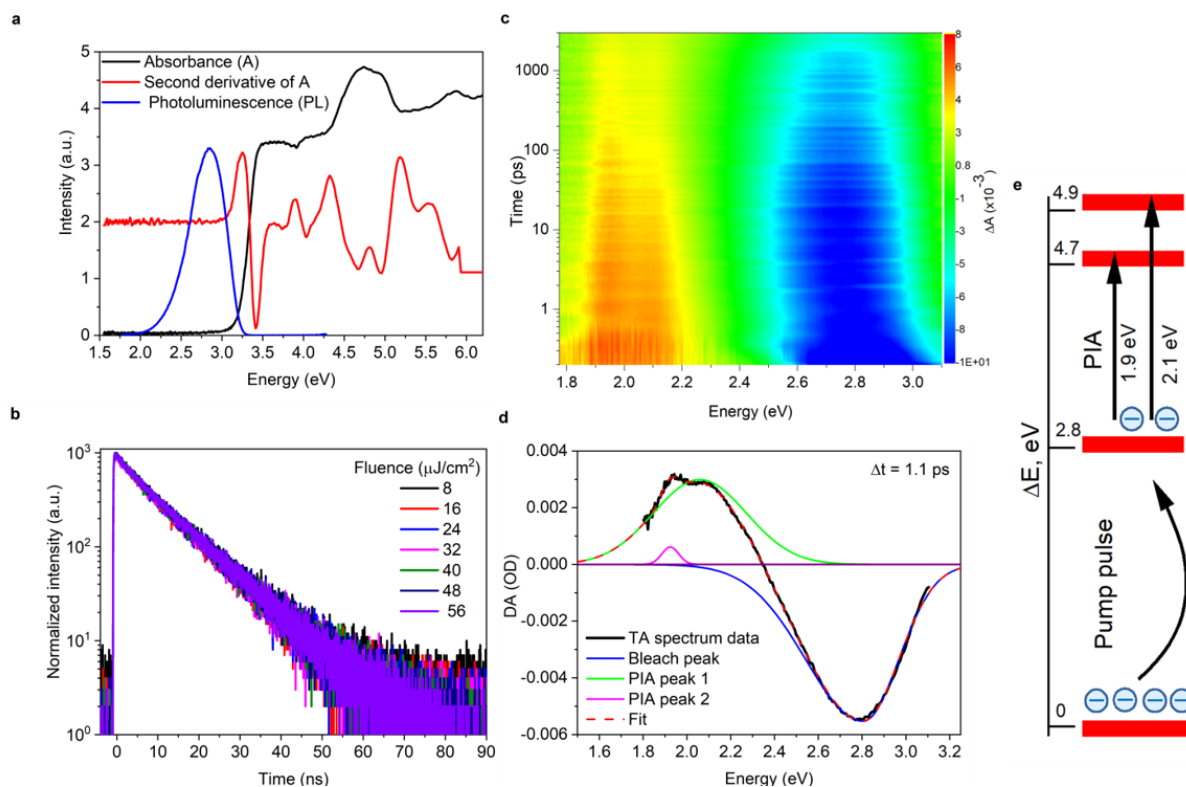
Figure 2.2: Optical measurements on the high quantum yield material. (a) Absorbance spectrum, and its second derivative, and PL spectrum (excitation at 3.45 eV). (b) PL decay transients for a range of excitation fluences at 3.2 eV and an emission wavelength of 2.85 eV. (c) Transient absorption (TA) map for excitation at 3.2 eV showing both positive and negative differential absorption (ΔA) i.e. photo-induced absorption (PIA) and bleach features, respectively. (d) TA spectrum for a pump-probe delay of Δt = 1.1 ps. (e) Schematic depiction of energy levels involved in the photo-induced absorption (PIA) occurring at 1.9 eV and 2.1 eV following photoexcitation by the pump pulse, corresponding to absorption into levels located at 4.7 eV and 4.9 eV by electrons located in 2.8 eV state [25].

This brightest material, $Mo_8O_{26}[C_{18}H_{32}N]_2[C_6H_{16}N]_2$, attracted their attention and they carried out further research on it. The steady-state absorbance and photoluminescence (PL) spectra of this sample were measured (Fig. 2.2). The absorbance spectrum shows a sharp edge at 3.2 eV (390 nm) and a prominent feature centred about 4.8 eV (260 nm), which the second derivative spectrum reveals to be composed of two overlapping peaks located at 4.7 eV and 4.9 eV (264 nm and 253 nm). A pronounced increase in the absorbance around 3.2 eV has previously been assigned to intramolecular photo-induced oxygen-to-molybdenum charge transfer in POMs, with its position varying with the chemical composition and structure of the octamolybdate and associated ligands [26], [27]. The PL spectrum is dominated by a single broad peak centred at 2.85 eV (435 nm), corresponding to a Stokes' shift of 0.4 eV from the band edge, with a full width at half maximum of 0.13 eV. The decay transient obtained at the PL

peak, presented in Fig. 2.2b, is independent of excitation fluence over the range from 8 μJ/cm^2 to 56 μJ/cm^2, consistent with a recombination process that is free of the influence of any saturable charge trapping site. A single broad negative absolute differential absorption (ΔA) (i.e. a bleach) feature centred at 2.85 eV (435 nm) and a two-component positive ΔA feature (a photo-induced absorption, PIA), composed of a dominant peak located at 2.1 eV superimposed with a minor peak located at 1.9 eV, were observed experimentally (Fig. 2.2c and d), where a 3.2 eV (385 nm) pump pulse and white light continuum probe pulse were used. The two PIA features correlate well with the excited state absorption from the emitting state to the broad absorption peaks observed at 4.7eV and 4.9 eV i.e. absorption at 1.9 eV and 2.1 eV respectively by electrons already in a state at about 2.8 eV, present due to photoexcitation by the pump pulse. The bleach feature located at 2.8 eV spectrally overlaps with the PL peak, indicating that it is due to state filling via Pauli blocking and/or overlapping stimulated emission. Since this feature is not observed in the steady-state absorbance spectra, which shows no significant features at energies below 3 eV, it appears that absorption is occurring below the apparent band gap indicating the presence of optically forbidden transitions, as commonly observed in biological structures and quantum dots [28].
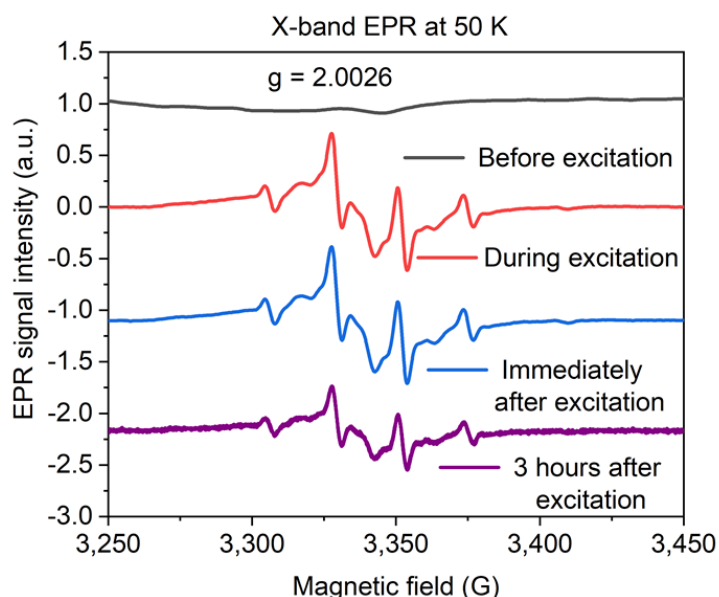

Figure 2.3: EPR spectroscopy. The bright-blue luminescent sample subjected to EPR analysis showing no distinctive signal when not illuminated (top), instantly developing a specific (g=2.0026) signal upon UV (365 nm) illumination present during and after excitation for at least 3 h [25].

In the Electron Paramagnetic Spectroscopy measurement (Fig. 2.3), whereas no distinctive signal was observed before illumination, all samples show an EPR peak upon UV (365 nm) illumination with a specific signal of proportionality factor g = 2.0026 during and after excitation for at least 3 hours, which suggests the existence of a long-lived charge state. Nanoco believed this long-lived charge state is on pyridinium and the hyperfine interaction of the electron with one ^{14}N ($l = 1$) and two ^{1}H ($l = \frac{1}{2}$) nuclei in the pyridine ring of the ligand leads to the multi-line structure, leaving the octamolybdate in an oxidised $(Mo_8O_{26})^{3-}$ state.

Discovering the secret behind such a high QY in this material would allow a better control over the optical transitions in many other nanomaterials and the creation of nanostructures with novel optical properties. Hence, cooperating with Nanoco, we started our research to study this novel material from the theoretical aspect of nanostructure engineering. Employing quantum mechanical modeling, we explored the properties of light conversion at the molecular level. Meanwhile, another POM, {Mo$_8$O$_{26}$[C$_6$H$_{16}$N]$_4$·2CH$_3$OH}, also attracted our interest as it was found to be completely non-luminescent, despite having a very similar structure to the bright-emitting one. We believe that finding the origins of the different performance between these two materials would help complete our understanding of the luminescence mechanism.

With the advantage of high computational accuracy, without expensive cost when dealing with the problem of a many-body system, density-functional theory (DFT) was chosen to study the ground state of these materials. For the excited states properties, such as optical absorption, I, instead, used time-dependent density-functional theory (TDDFT), which allows the calculation of the full spectrum of a system with only a marginal increase of computational cost compared to DFT [29].

In this chapter, I first show the molecular structure of bright-blue luminescent and non-luminescent samples measured experimentally, which provide the atomic positions and lattice parameters for my simulation. Then I present the calculation results, where I study the properties of the ground and the excited states of these samples and use them as a guide to explain the experimental observation. Finally, the influence of vdW interactions on the calculation results are discussed.
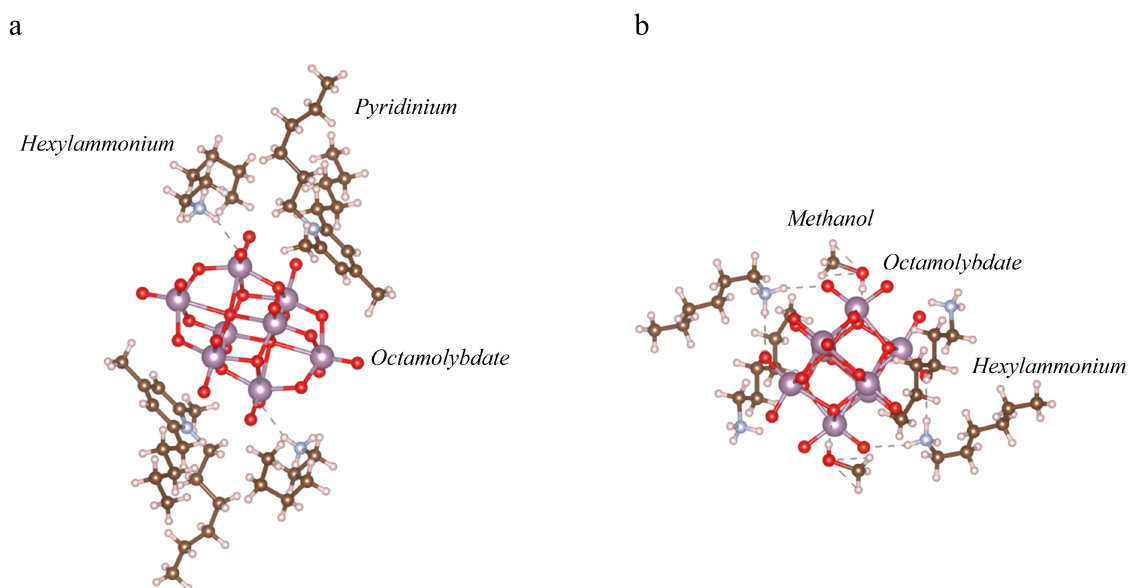
a

b

Figure 2.4: Molecular structure of (a) bright-blue luminescent sample, (b) non-luminescent sample. Colour code: white spheres, hydrogen; brown spheres, carbon; red spheres, oxygen; silver spheres, nitrogen; lilac spheres, molybdenum.

2.2   Results and Discussion

I focus on two samples of organic-polyoxometalate hybrids: $\{Mo_8O_{26}[C_{18}H_{32}N]_2[C_6H_{16}N]_2\}$ and $\{Mo_8O_{26}[C_6H_{16}N]_4 \cdot 2CH_3OH\}$, a bright-blue luminescent sample with extremely high quantum efficiency of 99.9% and a non-luminescent sample, respectively. The molecular structure and the atomic positions of these two samples were both measured experimetally by Nanoco, and the unit cells of our simulated systems were built accordingly, as presented in Fig. 2.4. The luminescent material consists of three major components: (1) octamolybdate anion $[Mo_8O_{26}]^{-4}$, the core component in the POMs with flexible photoactive properties, coplanar with (2) two pyridinium ligands $[C_{18}H_{32}N]^{-1}$ (each in opposing "polar sites" on the cluster), where a n-hexyl chain is bound to the pyridinic nitrogen, an extended n-pentyl chain is bound to the C-2 (ortho) carbon with further two methyl groups each bound to the C-4 (para) and C-6 (ortho) carbon atoms on the pyridinium ring, and together with (3) two hydrogen bonding hexylammonium ligands $[C_6H_{16}N]^{-1}$ in a trans-configuration (each in opposing "equatorial" sites on octamolybdate). The non-luminescent material is also centered on the octamolybdate ligands, but replacing pyridinium with hexylammonium and a methanol molecule.

In general, the mechanically stable equilibrium configuration of a molecular system is obtained

by performing relaxation calculations which minimize the inter-atomic force and stress, leading the system to its minimum energy [30], [31]. The relaxation calculation is completed when the atoms reach the positions where the force acting on them are minimised corresponding to the most stable structure. The relaxation calculation can be performed on either crystal structure (k-point mesh) or molecular structure (Gamma point only). I chose the latter, as I planed to start my study of these POMs from their molecular structure first. Besides, since the key component for explaining the luminescence in this system is the octamolybdate, the positions of Mo and O should be as close as possible to the experimental ones. And, according to Ref.[32], the length of Mo-O bonds after geometric optimization is closer to the experiment when the relaxation calculation is applied to the supercell model (modelled as an isolated molecule). Hence, for all of the samples in this study, the relaxation calculations were performed in the supercell model, using a $35 \times 35 \times 35$ Å super cell, where the Broyden–Fletcher–Goldfarb–Shanno (BFGS) algorithm was used in the computation. However, the original molecular structure of the samples shown in Fig. 2.4 was measured experimentally and therefore should not need to be optimized. Nevertheless, I decided to divide the calculations into two sets based on the atomic positions before and after structural relaxation. I aimed to explore the differences between them and to see which better explained the experiment results. By running these two sets of calculations, I expected to obtain a deeper understanding of the mechanism behind the high luminescence quantum yield observed in this system.

The simulated systems outlined above are labelled as S_{ij} for simplicity, where $i = 1$ for the blue-luminescent sample and $i = 2$ for the non-luminescent sample, whereas $j = 1$ indicates the system without the geometric optimization (unrelaxed system) and $j = 2$ stands for the one with geometric optimization (relaxed system).

2.2.1 The ground state

The electronic structure (see Fig. 2.5) is obtained within the DFT framework, using the Quantum Espresso package [33] . To reduce the domination of basis set and make computation achievable for a large system, I used ultrasoft pseudopotentials (USPP) with the Perdew-Burke-Ernzerhof (PBE) functional [34]–[37], which allows the use of require smaller cut-off energies (60 Ry was chosen after convergence test). The unit cell of the system for all systems (S_{11}, S_{12}, S_{21}, and S_{22}) is defined as a large cubic cell with lattice constant of 35 Å. This

2.2. Results and Discussion
Chapter 2. DFT study of
octamolybdate-based polyoxometalates

choice guarantees the system is surrounded by sufficient vacuum for periodic boundary condition calculations. Martyna-Tuckerman correction is applied to evaluate Coulomb energies and force, which eliminates the errors caused by dealing with a cluster/molecule in an infinitely replicated periodic system [38]. The electronic structure is calculated at the Gamma point.
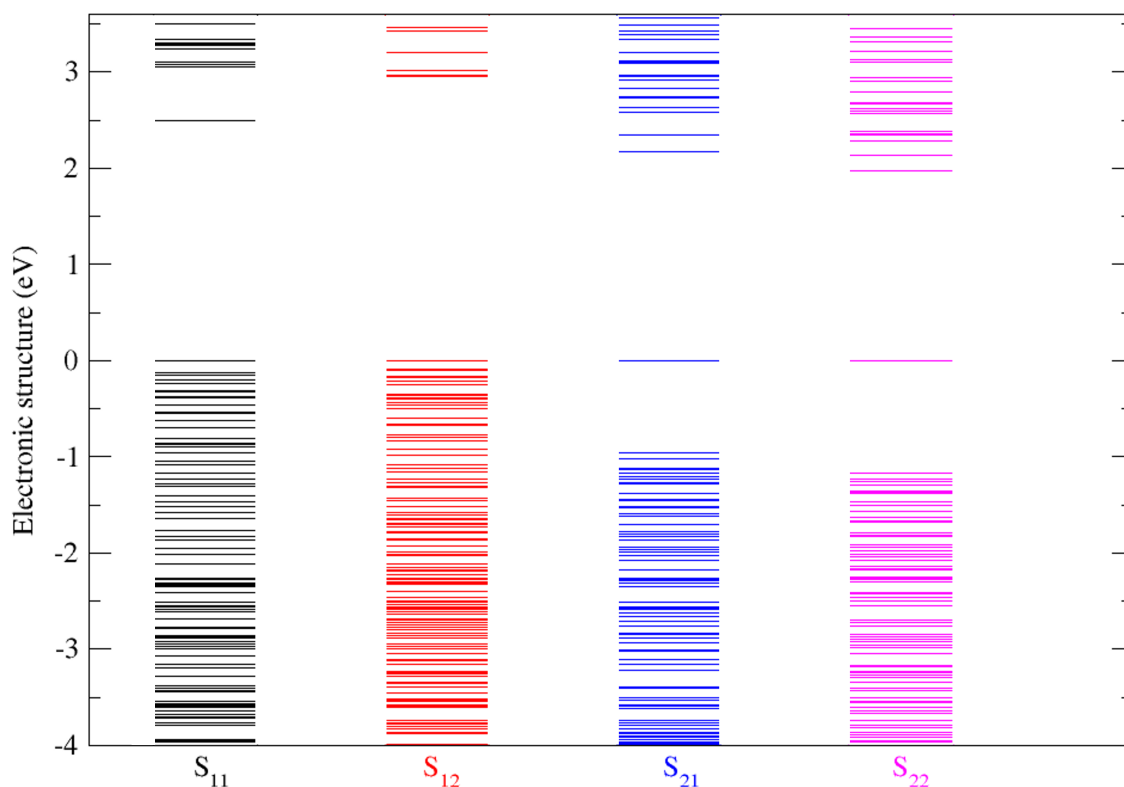
Figure 2.5: Electronic structure of the bright-blue luminescent and non-luminescent samples before and after structural relaxation. The energy level of HOMO is aligned to 0 eV.

A significant difference between the two materials in electronic structure, as illustrated in Fig. 2.5, is the presence of an "isolated" HOMO (two-fold degenerate) in the non-luminescent sample, where a wide gap between this state and HOMO-2 is found. An isolated LUMO is also found in the bright-blue luminescent sample, but it is removed after structural optimization, while relaxation has a more limited influence on the electronic structure of non-luminescent sample. Structural optimization also affects the band gap: it increases from 2.50 eV in S_{11} to 2.96 in S_{12}; in contrast, it decreases slightly from 2.17 eV in S_{21} to 1.97 eV in S_{22}.

Fig. 2.6 and 2.7 indicate that, for the bright-blue luminescent sample, the occupied states close to the band edge are mainly derived from the oxygen p-orbitals of the octamolybdate (the oxygen atoms further apart from pyridinium dominate the HOMO). The absence of an overlap between molybdenum and oxygen orbitals favours a dynamic transfer of the electrons in these
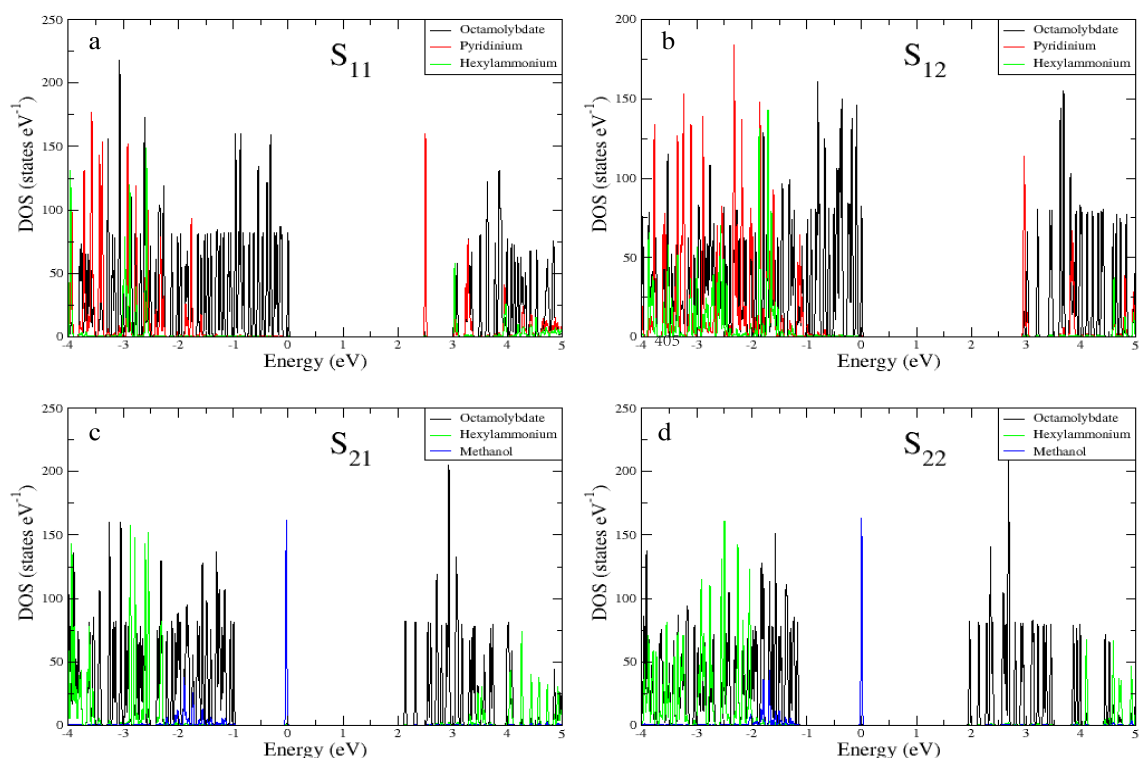
Figure 2.6: Partial density of states (PDOS) of bright-blue luminescent (a) and (b), non-luminescent samples (c) and (d) based on the atomic positions before (a), (c), and after (b), (d) the relaxation. HOMO is aligned to 0 eV as reference.

occupied states without bonding to molybdenum, while the hybrid orbitals reveal a bonding between Mo d states and O p states at lower energy (below -2 eV) [32].

The composition of the LUMO in the non-luminescent sample remains the same after structural optimization and derives mostly from the octamolybdate. In the unrelaxed bright-blue luminescent sample, the LUMO is isolated from other states and is contributed to by C p orbitals and N p orbitals from pyridinium (Fig. 2.7a) exhibiting no overlap with the HOMO. This makes an electron transfer between HOMO and LUMO difficult in a pristine state, but, once the electron is excited to the LUMO, it may result in a long-lived charged state on pyridinium as what observed from EPR spectroscopy measurement (Fig. 2.3). In the relaxed structure S_{12}, there is a small component from the d-orbital of molybdenum in the LUMO (Fig. 2.7b). The overlap between HOMO and LUMO in octamolybdate will induce the intramolecular oxygen-to-molybdenum charge transfer when the electron is excited from HOMO to LUMO, but since the LUMO is still dominated by C p-orbital of pyridinium, this transition may exhibit a weak oscillator strength in the pristine state as well. So far we have been considering the system ground state. The calculation of the optical absorption spectra (OAS) and the simulation of ox-

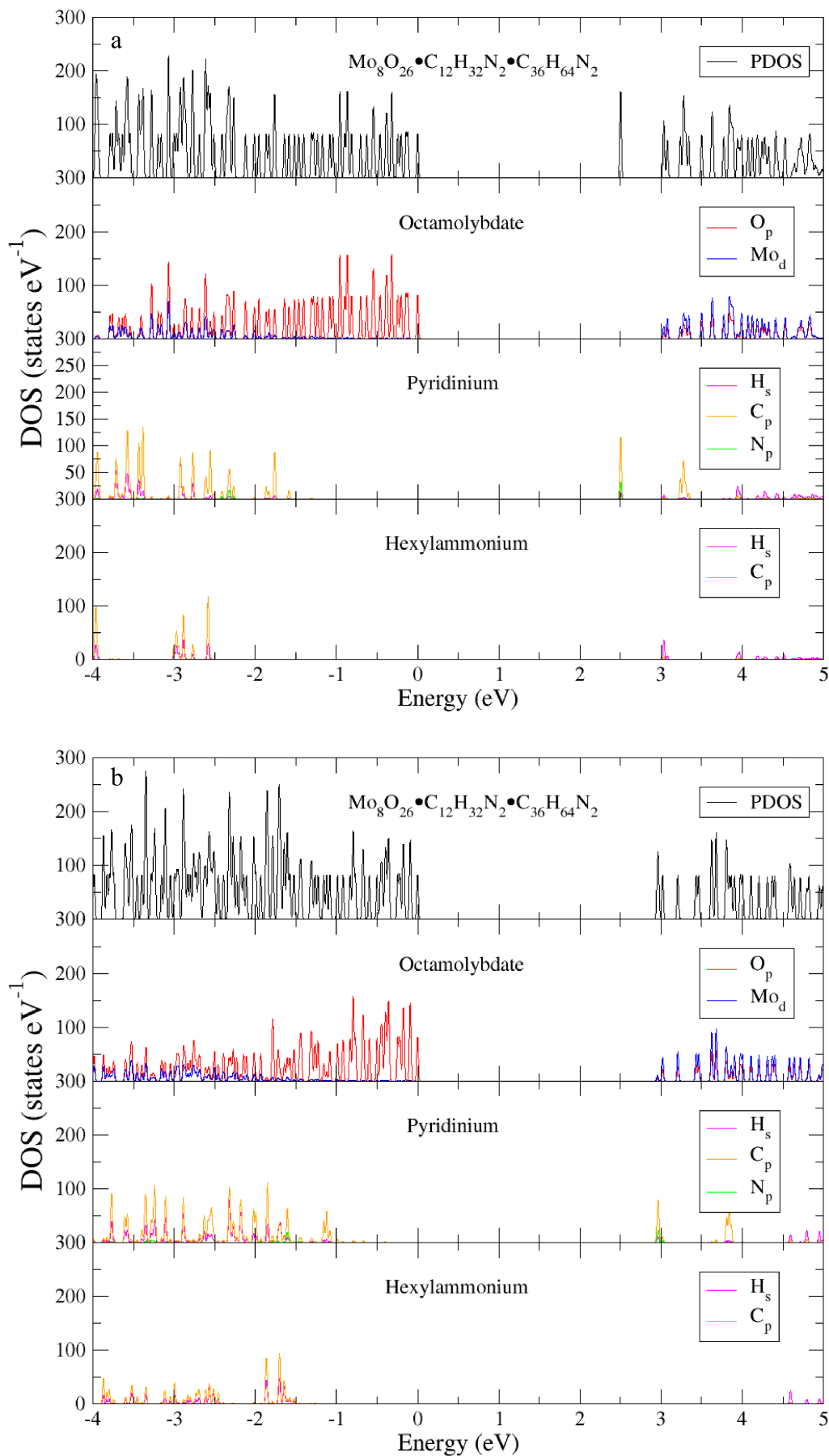Figure 2.7: PDOS of spd orbitals for the bright-blue luminescent sample (a) before and (b) after structural optimization.

idized/reduced states of the octamolybdate required for studying the photo-induced optical
properties of these two samples deals instead with excited states.

2.2.2 The excited states

The excited states calculations were performed based on two TDDFT approaches: turbo Lanczos (TL) and turbo Davidson (TD), separately. Although considering electron interaction is
theoretically necessary when simulating a multi-atom system, it is interest to test which case,
including or excluding the electron interaction in the calculation, was closer to experiment. The
code for turbo Davidson provided by QE allows us to simulate the condition of non-interacting
electrons, which is achieved by ignoring the interaction terms when solving Casida's equation,
leading to a system consisting of independent particles (IP). Hence, the calculation based on
the TD algorithm is split into two cases, with and without the electron interaction.
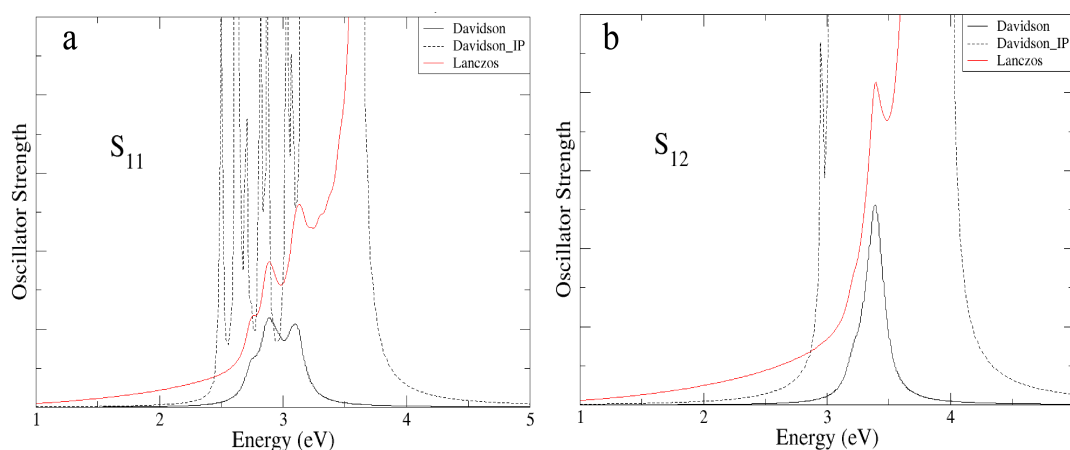
Figure 2.8: OAS of bright-blue luminescent sample (a) before structural relaxation (S_{11}) and
(b) after structural relaxation (S_{12}), obtained from TD (black line) and TL (red line) algorithm.
Solid and dotted lines refer to TD calculations with or without interaction, respectively. The
Oscillator strength is used to describe the linear absorption coefficient here.

Sixty-four lowest-energy transitions (resulting from a combination of 8 highest occupied states
and 8 lowest unoccupied states) were included in the calculation, which are sufficient to characterize the spectral features of the region where the first absorption peak occurs.

The simulated OAS presented in Fig. 2.8 indicate the consistency between the results of the TD
algorithm with electron interactions (solid black lines) and the TL algorithm (solid red lines)
in the lower energy range, where the curves exhibit the same features and, in particular, the
first peak at the same point (2.88 eV for S_{11} and 3.39 eV for S_{12}). Unfortunately, due to the

2.2. Results and Discussion
Chapter 2. DFT study of
octamolybdate-based polyoxometalates

System	Transition energy(eV)	Transitions	Contribution(%)
S_{11}	2.88	HOMO-2 $\rightarrow$ LUMO	49.63
		HOMO-2 $\rightarrow$ LUMO+1	49.56
S_{12}	3.39	HOMO-5 $\rightarrow$ LUMO	1.26
		HOMO-4 $\rightarrow$ LUMO	13.64
		HOMO-5 $\rightarrow$ LUMO+2	1.62
		HOMO-2 $\rightarrow$ LUMO+2	81.77
S_{21}	2.38	HOMO $\rightarrow$ LUMO	49.42
		HOMO-1 $\rightarrow$ LUMO	49.73
S_{22}	2.20	HOMO $\rightarrow$ LUMO	50
		HOMO-1 $\rightarrow$ LUMO	50

Table 2.1: The transition between molecular orbitals contributing to the first peak of the optical absorption spectrum (see Fig.2.8), and their corresponding contribution.

expensive calculation cost, the energy window accessible by the TD algorithm is limited by the number of eigenstates included in the calculation, which results in the TD curve dropping to zero at about 4 eV. Compared with TD, TL can produce a more complete OAS due to the exclusion of occupied states. The features of the TL spectra relative to S_{11} and S_{12} indicate further absorption at a shorter wavelength in agreement with experiment (see Fig. 2.2). For S_{11}, the TD OAS without electron interactions is characterized by a curve exhibiting multiple peaks where the first peak is red-shifted relative to the one with electron interactions. It is a result of weak correlation between the eigenstates in the system without electron interactions, and, of the presence of a large inter-atomic force in the unrelaxed system. Therefore, the system behaves more like a cluster of independent particles rather than one single molecule, each of which leads to different transitions at different energies hence to multiple absorption peaks. As the energy of the first peak in the OAS is equal to the band gap in an independent-particle system when considering Gamma point only, the first peak exhibits a red-shift in Fig. 2.8 (from 2.88 eV to 2.50 eV in S_{11} and from 3.39 eV to 3 eV in S_{12}). In contrast to S_{11}, S_{12} experiences a weaker inter-atomic force after structural optimization, hence, the independent-particle approximation produces fewer peaks in the OAS presenting a more consistent result with the interacting electron case.

Significantly, the location of the first peak in the OAS (about 3.39 eV) produced from S_{12} agrees well with the experiment. The transitions involved in this peak, listed in Table. 2.1, are mainly from HOMO-2 to LUMO+2 (81.77%). Fig. 2.9b indicates that these two states overlap around the octamolybdate, which, as I discussed above, explains the intramolecular photo-induced oxygen-to-molybdenum charge transfer in POMs observed in the experiment. Fig. 2.9b also
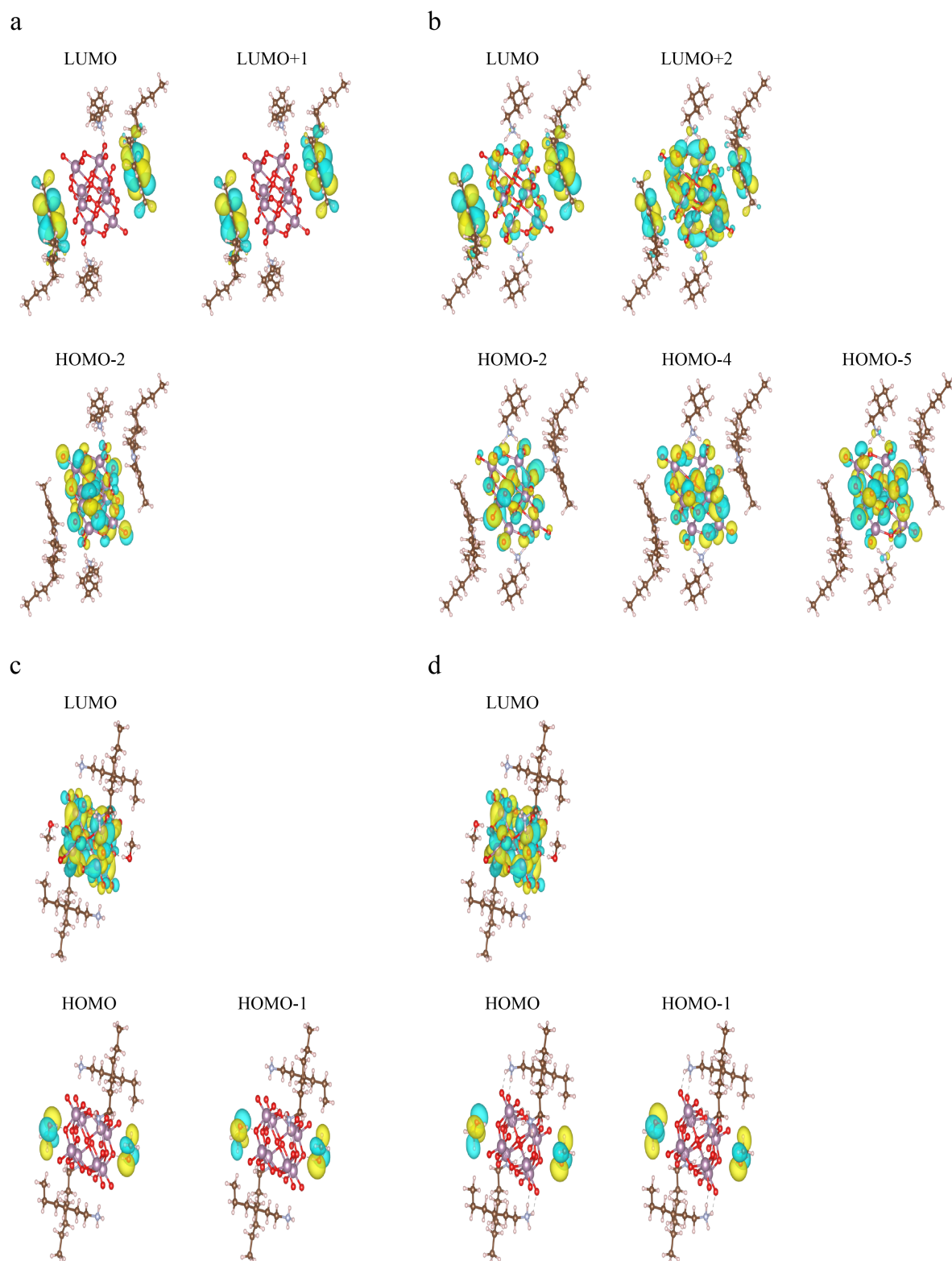
Figure 2.9: The key MOs contributing to the first peak of calculated absorption spectrum for S_{11} (a), S_{12} (b), S_{21}(c), and S_{22} (d).

shows that the LUMO+2 is partially around pyridinium, leading to the electron-hole separation (the hole on octamolybdate and the electron on pyridinium). It should be mentioned that the electron in LUMO+2 can easily relax to the LUMO due to their strong overlap. A large portion of the LUMO is located around the pyridinium, resulting in a higher probability for the electron to localise on this ligand. However, the partial localisation of the LUMO's charge density on the octamolybdate, could favour a faster electron-hole recombination as the HOMO is all localised on the octamolybdate. This contrasts with the long PL lifetime observed experimentally (see Fig. 2.3). On the other hand, there is no overlap between HOMO-2 and LUMO/LUMO+1 that provide the main contribution to the first peak of optical absorption for S_{11} (see Table. 2.1 and Fig. 2.9), which leads to a very low QY hence to the low optical strength of the transition. Correspondingly, we see a weaker oscillator strength as represented in Fig. 2.8a (S_{11}) than the one in Fig. 2.8b (S_{12}). Therefore, although the first peak of the OAS occurs at an energy 0.57 eV lower than the experiment, this case provides a better explanation for the observed long luminescence-lifetime. Whether we consider S_{11} or S_{12}, the electron transfer from octamolybdate to pyridinium dominates the optical excitation. Physically it means that optical excitation provokes an intermolecular charge transfer between octamolybdate and pyridinium, which results in an oxidized state of the octamolybdate $(Mo_8O_{26})^{3-}$ and in the charging of the pyridinium ring with one electron. This is only possible if the pyridinium ring is positioned flat on the octamolybdate – exactly the position it has in both structures before and after structural optimization. Long chained alkyl substituents on positions 1(N) and 2(C) determining the ring containing the N charge adhere strongly to octamolybdate anionic surfaces by inducing surfactant-like bonding directionality due to molecular polarisation. The ring is further determined to adopt a flat positioning due to the presence of *methyl* substitutions on 4(C) and 6(C) positions prohibiting short-range orthogonal(sideways) contact. This explains the sensitivity of the QY to the structure of pyridinium shown in Fig. 2.1.

The absorption for the non-luminescent sample, according to our calculation, is due to the transition between the HOMO/HOMO-1, residing on the methanol, and the LUMO, localised on the octamolybdate, whose wave functions do not overlap. In this case, as the methanol is a stable neutral molecule, the electron in HOMO/HOMO-1 is hard to excite. The corresponding OAS is considerably weaker than in the bright-blue luminescent sample as shown in Fig. 2.10 where the results relative to the relaxed systems (S_{12} and S_{22}) are chosen for the comparison as they are closer to experimental spectra. The electron transfer to octamolybdate from methanol
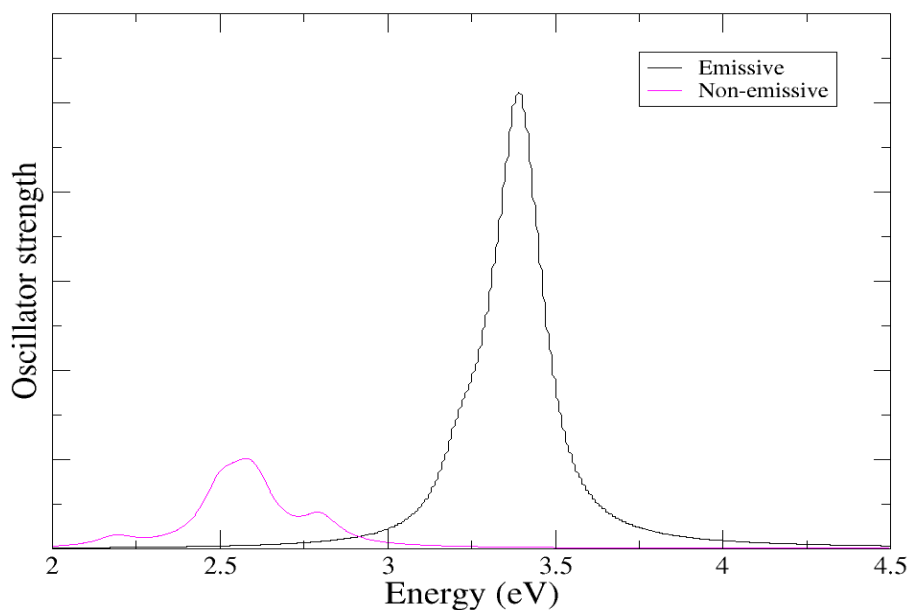
Figure 2.10: The comparison of OAS between bright-blue luminescent (S_{12}) and non-luminescent (S_{22}) sample, relative to the relaxed systems.

results in the reduced state $(Mo_8O_{26})^{5-}$.

The octamolybdate, acting as the potential electron donor or acceptor, respectively in the bright-blue luminescent and non-luminescent system, is closely linked to the process of excitation. I believe figuring out the influence due to the different states of octamolybdate (oxidized and reduced) on the photo-luminescence should help us shed light on the luminescent mechanism. Therefore, two systems consisting of the octamolybdate alone are built in a 25 × 25 × 25 Å supercell. As the pristine state of octamolybdate presents 4 negative charges, the systems defined by the number of charges for simulating electron donor and acceptor are: (1) $[Mo_8O_{23}]^{3-}$ for the case where the octamolybdate acts as an electron donor (bright-blue luminescence), and (2) $[Mo_8O_{23}]^{5-}$ for the case where the octamolybdate acts as an electron acceptor (non-luminescence).

For system (1), where the oxidized state $(Mo_8O_{26})^{3-}$ is caused by an electron transfer to pyridinium, the effective HOMO and LUMO reside both on the octamolybdate, thus exhibiting a large overlap and strong PL (see Fig. 2.11 left panels). In contrast, in system (2), the charge configuration of the reduced state $(Mo_8O_{26})^{5-}$ indicates that only the HOMO is localized on the octamolybdate but not the LUMO, leading to suppressed emission. The discussions above, is consistent with the observed bright-blue luminescence of $\{Mo_8O_{26}[C_{18}H_{32}N]_2[C_6H_{16}N]_2\}$ and poor luminescence of $\{Mo_8O_{26}[C_6H_{16}N]_4·2CH_3OH\}$.
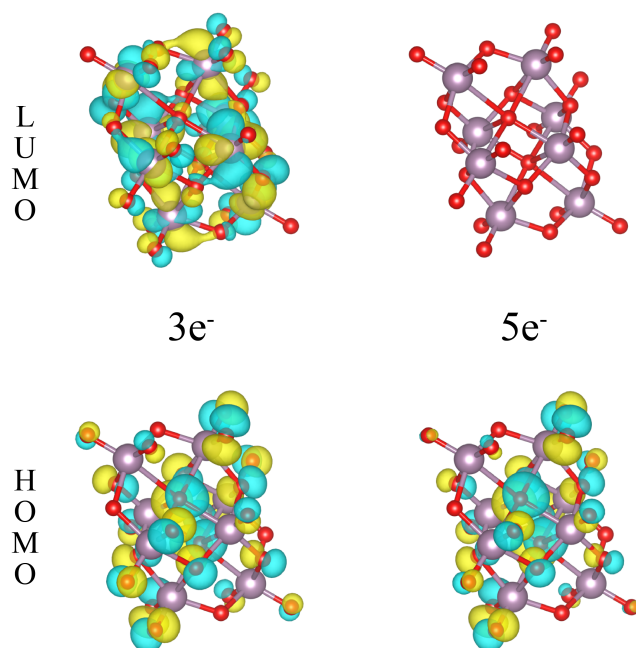
Figure 2.11: The MOs of HOMO and LUMO obtained from $(Mo_8O_{26})^{3-}$ (left) and $(Mo_8O_{26})^{5-}$ (right).

2.3 Van der Waals effect

I investigated the influence due to vdW interactions on geometries, PDOS, and OAS, where the vdW interactions were introduced using the van der Waals density functional (vdW-DF) supplied by QE.

	Total force at the beginning of structural relaxation (Ry/au)	Δx (Å)	Δy (Å)	Δz (Å)
GGA-PBE	2.48	0.32	0.34	0.23
vdW-DF-PBE	2.38	0.19	0.16	0.17

Table 2.2: Total force (the square root of the sum of the squares of all the forces acting on each atom) in the system at the beginning of structural relaxation and average shift of atomic positions along x, y, and z compared to the experiment.

The geometric optimization calculations were performed again, replacing GGA with vdW-DF. As indicated in Table. 2.2, at the beginning of structural relaxation, the total force acting on the system is about 2.48 Ry/au when using GGA, and it decreases to 2.38 Ry/au in the case of vdW-DF. After structural relaxation, the rearrangement of the atomic positions is less significant when including vdW interactions. I attribute this to the fact that the total force is large before the relaxation due to the incomplete environmental conditions simulated in the

calculations, which lack: vdW interactions, the effect of the presence of a (polarisable) solvent surrounding the molecules, and the presence of periodic boundary conditions. Introducing vdW interactions by using vdW-DF brings the simulated environment closer to the experimental conditions, which decreases the total force acting on it before the relaxation. Also, due to this reason, the calculated rearrangement of the atomic positions, that aims to minimise the force acting on atoms, exhibits a better agreement with experiment [39].
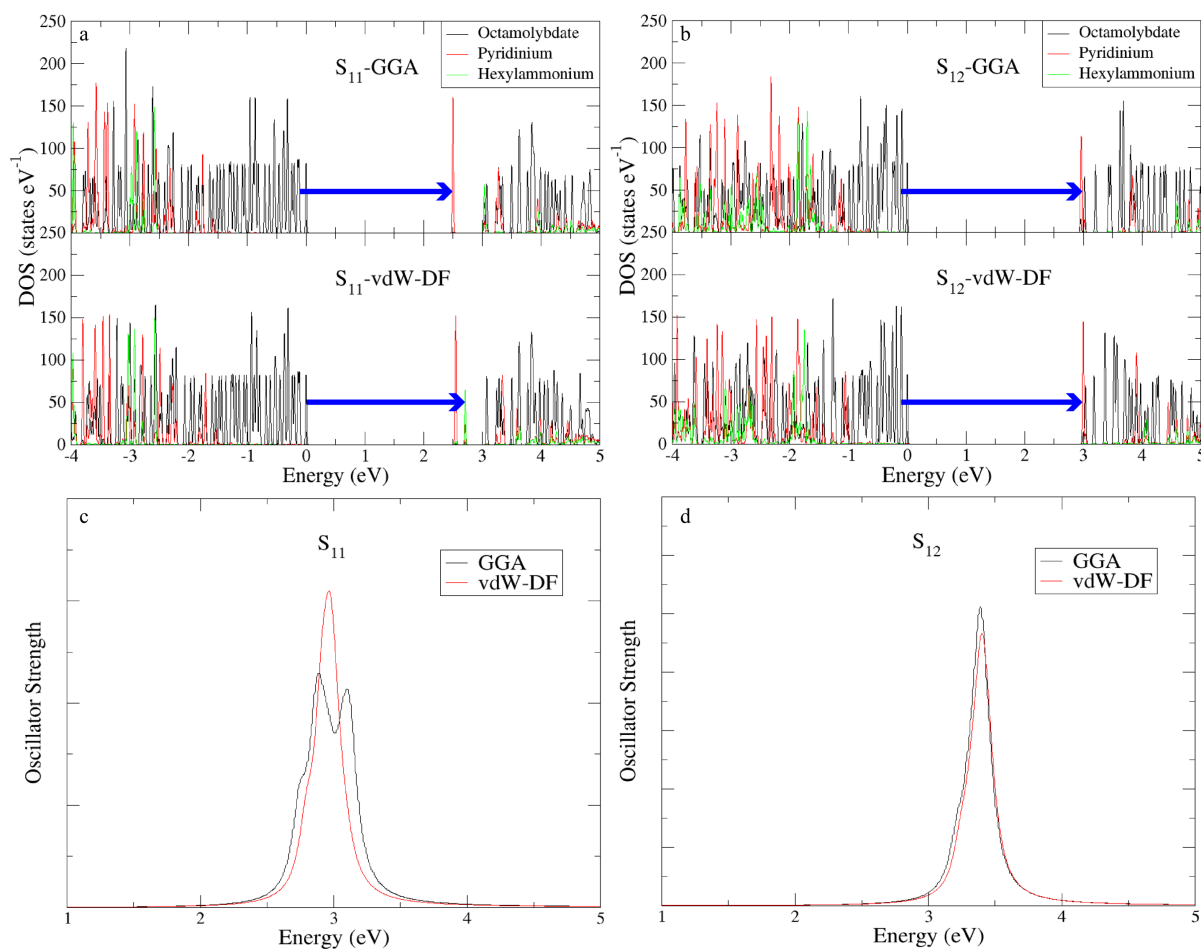
Figure 2.12: PDOS of bright-blue luminescent sample (a) before (S_{11}) and (b) after (S_{12}) structure relaxation calculated from GGA (top panel) and vdW-DF (bottom panel), where the blue arrows indicate the transition contributing to the first peak of OAS (obtained from TD algorithm) presented in (c) and (d): For S_{11}, from HOMO-2 to LUMO in the case of GGA, and from HOMO to LUMO+2 in the case of vdW-DF; For S_{12}, from HOMO-2 to LUMO+2 in both cases of GGA and vdW-DF.

To test the influence of the vdW interactions on PDOS and OAS, the unrelaxed system (S_{11}) and the system with atomic positions obtained from the relaxation calculation based on GGA (S_{12}) were chosen. PDOS and OAS were calculated using either vdW-DF or GGA: the results are compared in Fig. 2.12. We see that the vdW interactions have little influence on the PDOS for

either S_{11} or S_{12}. However, for S_{11}, the unoccupied state contributed to by the hexylammonium
(green line in Fig. 2.12a) exhibits a red-shift, from the hybrid orbital of octamolybdate (located
at 3.02 eV in Fig. 2.12a top panels) to the hybrid orbital of pyridinium (located at 2.71 eV in
Fig. 2.12a bottom panels).
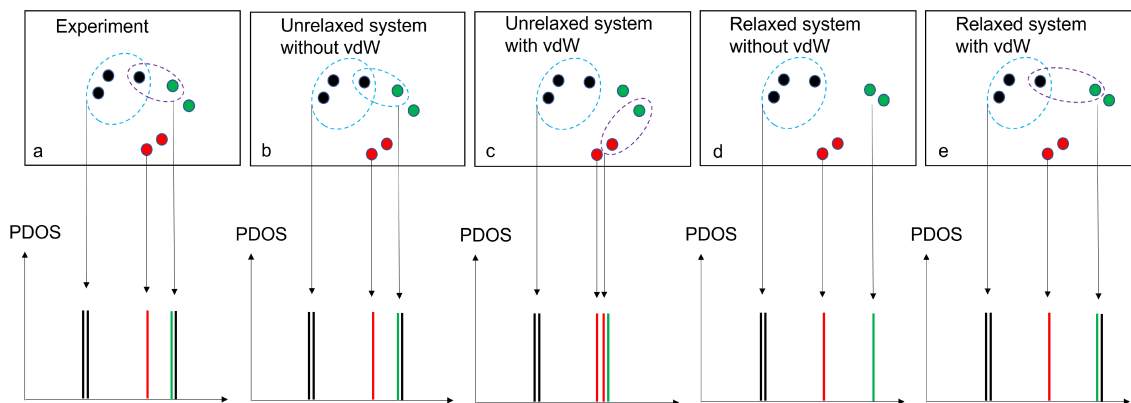
Figure 2.13: Schematics of PDOS derivation in (a) experiment with true short- and long-range
interactions, unrelaxed system (S_{11}) (b) without and (c) with vdW-DF, and relaxed system (S_{12})
(d) without and (f) with vdW-DF. The blue (purple) dashed ellipses represent short (long)-
range interactions; black, red and green solid circles represent octamolybdate, pyridinium and
hexylammonium atoms, respectively.

This could be the result of the fact that the modelled system is built using the experimen-
tal atomic positions, which were determined by the effect of vdW interactions in the first
place. The long-range interactions are missing in the unrelaxed system without vdW-DF (see
Fig. 2.13b), but since the H atom in hexylammonium is close enough to the Mo atom in octa-
molybdate, virtual short-range interactions (rather than long-range interactions which are at
play in the experimental conditions) are introduced in DFT calculation and produce the unoc-
cupied state contributed to by octamolybdate and hexylammonium at 3.1 eV in Fig. 2.12a top
panels. The vdW-DF introduces further long-range interactions (Fig. 2.13c), on top of the ones
already indirectly accounted for by using the experimental atomic positions (which were ar-
rived at under the influence of vdW interactions), resulting in a double counting that artificially
increases the strength of the interactions between pyridinium and hexylammonium. This leads
to the presence of an unoccupied state (LUMO+2) contributed to by pyridinium and hexylam-
monium. As indicated in Fig. 2.12b, this unoccupied state dominates the optical absorption
leading to the significant difference with the OAS calculated without considering vdW inter-
actions (using GGA). The transition corresponding to the first peak, in this case, is from HOMO
to LUMO+2 indicating that the optical absorption is determined by hexylammonium, which

is in contrast to experimental observation. In S_{12}, the distance between pyridinium and hexylammonium (indicated by the distance between the nitrogen atom in pyridinium and that in hexylammonium) increases (N-N increases to 6.34 Å in S_{12} from 5.36 Å in S_{11}), and it is out of the range of both long-range vdW interactions introduced by vdW-DF and virtual short-range interactions from DFT calculations (see Fig. 2.13d and e). The PDOS obtained from S_{12} in the case of vdW-DF, hence, is produced with the correct long-range interactions (Fig. 2.13e) and doesn't exhibit the unexpected orbital shift, and the orbitals dominating the optical absorption remain the same as in the case without vdW interactions (HOMO-2 and LUMO+2). Therefore, the introduction of vdW interactions leads to a negligible effect on the OAS for S_{12} (see Fig. 2.12d), where the location of the first peak shifts from 3.39 eV (GGA) to 3.40 eV (vdW-DF), closer to experimental observation.

2.4 Conclusions

In summary, I studied two samples, a bright-blue luminescent and a non-luminescent POM synthesized by Nanoco, using DFT as implemented in the Quantum Espresso suite of codes, where two sets of calculations, based on the systems with the atomic positions before and after structural optimization, were performed. In the system built directly from the experimental structure (before structural optimization) of the bright-blue sample, the HOMO and the states nearby (e.g. HOMO-1 and HOMO-2) are all formed by the O p-orbital of octamolybdate, and the LUMO is an "isolated" state derived from the N p-orbital of pyridinium that is located about 0.6 eV below LUMO+2 (LUMO is two-fold degenerate). Due to this unique electronic structure, there is no overlap between HOMO-2 and LUMO, the main orbitals contributing to the transition corresponding to the first peak in the OAS. This explains the long luminescence lifetime observed experimentally, as the LUMO would be a long-lived charge state once it is occupied by the electron. In contrast, in the system after structural optimization, the LUMO, contributed to by not only the N p-orbital of pyridinium but also by the Mo d-orbital of octamolybdate, is not "isolated" any more. The transition from HOMO-2 to LUMO+2 dominates the first peak of the OAS that occurs at 3.39 eV, close to the experiment (3.45 eV). The iso-surfaces of these two orbitals overlap around the octamolybdate, and in this region, the HOMO-2 is from the O p-orbital while LUMO+2 is from the Mo d-orbital, which explains the intramolecular photo-induced oxygen-to-molybdenum charge transfer observed experimentally. The octamolybdate in the bright-blue luminescent sample, whether before or after relaxation, plays the role of electron donor. Once an electron is transferred to a long-lived charge state (e.g. localised on an "isolated" state from pyridinium), the oxidized state of octamolybdate $(Mo_8O_{26})^{3-}$ is produced, in which both HOMO and LUMO reside exhibiting a large overlap, which leads to the strong PL measured experimentally.

In contrast, I found the electronic structure of the non-luminescent sample to be insensitive to structural optimization. HOMO (two-fold degenerate) and LUMO, the orbitals that dominate the first peak of the OAS, are contributed to by methanol and octamolybdate respectively exhibiting no overlap. Hence, a pronouncedly weaker optical absorption is obtained compared with that calculated for the bright-blue luminescent sample. In contrast to the bright-blue luminescent sample case, the octamolybdate in the non-luminescent sample is treated as the electron acceptor while the methanol is the electron donor during the excitation. I attribute

the poor luminescence of this sample to two reasons: 1) The methanol doesn't favour electron transfer as it is a neutral molecule with a stable electronic structure, and 2) in the reduced octamolybdate $(Mo_8O_{26})^{4-}$, there is no overlap between HOMO and LUMO.

Substituting GGA with vdW-DF in relaxation calculations brings the relaxed atomic positions closer to experiment, which is the result of the fact that the experimental structure was formed under the effect of vdW interactions. Including vdW interactions reduces the total force on the atoms at the beginning of structural relaxation so that they are closer to the position where the total force is minimised. In contrast to the significant influence on the structural relaxation, the vdW interactions have a negligible effect on the PDOS. However, for S_{11}, the use of vdW-DF causes a 'double counting' of vdW interactions and results in an unexpected unoccupied state appearing around the band edges, which dominates the transition contributing to the first peak of the OAS and leads to a disagreement with experimental observation. As the electron is transferred from octamolybdate to hexylammonium in this case, which is evidently in contrast with the experiment, such unexpected unoccupied states around the band edges were not investigated further. While for S_{12}, since the distance between pyridinium and hexylammonium increases due to the relaxation, the correlations between them are free from the vdW interactions induced by vdW-DF and do not produce any additional unoccupied state around the band edges. Nevertheless, in this case, use of vdW-DF does not have a significant influence on the OAS but leads to a 10 meV blue shift of the first absorption peak.

Future work

Future work will be devoted to improving the accuracy of our calculation results by: 1) introducing in the modelling a set of parameters to account for the presence of a solvent surrounding the molecules in the experimental sample; 2) using other approaches, *e.g.* GW and Bethe-Salpeter approximation, to calculate the optical properties and to find out the most appropriate one without compromising the accuracy and efficiency. I also plan to extend the research object to other transition-metal-substituted POMs, such as $SiW_{11}Mn^{4-}$ which is potentially a high-performance material to be used as a photoanode [40].

Some of the results from this chapter will be submitted soon for publication, as a result of a collaboration with the National Graphene Institute, the Department of Physics and Astronomy (both at the University of Manchester), Nanoco Technologies Ltd and the Institute for Functional Intelligent Materials,

National University of Singapore, in a paper titled 'Ultrabright, stable metal-organic blue quantum dots' by Virgil Gavriliuc, Ruben Ahumada-Lazo, Samantha Hardman, Georgia Kime, Adam Brookfield, Floriana Tuna, Steve Daniels, Nicky Savjani, Nathalie Gresty, Yang Zhou, Marco Califano, Nigel Pickett, David Binks, and Kostya S. Novoselov.

Part II

Light conversion in Tetrapods

Introduction

Branched nanocrystals, and tetrapods (TPs) in particular, [41] have recently emerged as highly versatile nanostructures for a wide range of applications [42] thanks to their unique mechanical and optoelectronic properties deriving from their peculiar geometry, coupled with their ease of fabrication and processability. In this second Part of the thesis I will present an investigation into the properties of homogeneous and core/arms TPs, highlighting some of their most interesting applications.

I will start with the study of CdTe/CdSe core/arms tetrapods (TPs) that are found to have great potential as building blocks for photo-catalytic cells for efficient CO_2 reduction owing to their particular configuration and electronic properties. In the following Chapter III, I will focus on homogeneous CdTe TPs (same material for core and arms) and show how in these nanocrystals a strong suppression of Auger processes can be achieved without affecting the radiative recombination. In both chapters, the TPs are assumed to have an ideal structural configuration where all 4 arms are symmetric and have the same size. However, in real samples, geometrically anisotropic branched nanocrystals can occur either accidentally or deliberately during the growth process. Hence, in Chapter III, the investigation of the effect of anisotropic growth in the width or the length of a single arm on the electronic and optical properties of CdTe/CdSe core/arms TPs and CdTe TPs is presented.

Chapter 1

Method

1.1 The semiempirical pseudopotential method

The semiempirical pseudopotential method (SEPM) [43] is used to solve the Schrödinger equation and obtain wavefunctions for systems containing millions of atoms. Compared with the traditional empirical pseudopotential method (EPM) [44], SEPM is more flexible for different crystal structures, and produces more accurate wavefunctions [45]. Besides, although SEPM is based on the calculation result from DFT in the local-density-approximation (LDA), SEPM can reproduce observed excitation energies by adjusting the potential, overcoming the shortcomings of the DFT [45].

1.1.1 Solving the Schrödinger equation

The continuous empirical pseudopotential is represented as [46]

$$v^{EPM}(q) = \frac{a_1(q^2 - a_2)}{a_3 e^{a_4 q^2} - 1} \tag{1.1.1}$$

The screened local effective potential $V_{loc}(\mathbf{r})$ produced from DFT [45] can be divided into an anion-centered and a cation-centered contribution assuming zinc blende structure with origin midway between cation and anion:

$$V_{loc}(\mathbf{r}) = \sum_n \left[v_{anion}(\mathbf{r} - \mathbf{R}_n + \mathbf{r_0}) + v_{cation}(\mathbf{r} - \mathbf{R}_n - \mathbf{r_0}) \right], \tag{1.1.2}$$

where n is the index for the primitive unit cell, $\mathbf{R}$ is the corresponding lattice vector, and $\mathbf{r_0}$ is the vector from intermediate point of cation and anion to anion. As the [111] facets of zinc blende structure is atomically identical to [0001] facets of wurtzite structure, Eq. (1.1.2) fits both of these structures. Fourier transforming this equation yields [46]

$$V_{loc}(\mathbf{G}) = \frac{1}{\Omega} \int_{\Omega} \left[v_{anion}\left(\mathbf{r}'\right) e^{i\mathbf{G}(\mathbf{r}'-\mathbf{r_0})} + v_{cation}\left(\mathbf{r}'\right) e^{i\mathbf{G}(\mathbf{r}'+\mathbf{r_0})} d\mathbf{r}' \right] \tag{1.1.3}$$

$$= \frac{cos(\mathbf{r_0} \cdot \mathbf{G})}{\Omega} v_+(G) - i\frac{sin(\mathbf{r_0} \cdot \mathbf{G})}{\Omega} v_-(G), \tag{1.1.4}$$

where

$$v_+(G) = v_{anion}(\mathbf{G}) + v_{cation}(\mathbf{G}),$$
$$v_-(G) = v_{anion}(\mathbf{G}) - v_{cation}(\mathbf{G}). \tag{1.1.5}$$

If the atomic potentials of anion and cation have inversion symmetry, then $v_+(G)$ and $v_-(G)$ can be calculated as:

$$v_+(G) = \frac{\Omega}{cos(\mathbf{r_0} \cdot \mathbf{G})} Re\{V_{loc}(\mathbf{G})\},$$
$$v_-(G) = \frac{\Omega}{sin(\mathbf{r_0} \cdot \mathbf{G})} Im\{V_{loc}(\mathbf{G})\}. \tag{1.1.6}$$

$V_{loc}(\mathbf{G})$ is obtained from DFT calculation, from which one obtains $v_+(G)$ and $v_-(G)$. As $v_{anion/cation}$ are well represented by $v_{anion/cation}(|\mathbf{G}|)$ [43], [46], $v_+(|G|) \rightarrow v_+(G)$ and $v_-(|G|) \rightarrow v_-(G)$ (spherical approximation). Two smooth curves are made to fit the $v_+(|G|)$ and $v_-(|G|)$ points separately from $G = 0$ a.u to G_{max} that leads to the convergence of $v_+(|G|)/v_-(|G|)$ (energy level of zero) giving a continuous expression for them. Then, according to Eq. (1.1.5), continuous semiempirical pseudopotentials can be obtained for each atom type α under the spherical approximation [45], [46]. The crystal potential therefore can be obtained as:

$$V_{loc}^{SEPM}(\mathbf{r}) = \sum_{\alpha,j,n} v_\alpha(r - R_n - r_{\alpha,j})$$

$$= \frac{1}{\Omega} \sum_{\alpha,j,n} \int_{\Omega} v_\alpha(|\mathbf{G}|)e^{-i(\mathbf{r}-\mathbf{R_n}-\mathbf{r}_{\alpha,j})\mathbf{G}} d^3 G, \tag{1.1.7}$$

where j is the atom index and $\mathbf{r}_{\alpha,j}$ is the basis vector for atom j of type α in unit cell n. The

Schrödinger equation based on the semiempirical pseudopotential is given by:

$$\hat{H}\psi_i(\mathbf{r}) = \{-\frac{\nabla^2}{2} + V_{loc}^{SEPM}(\mathbf{r}) + \hat{V}_{nl} + \hat{V}_{SO}\}\psi_i(\mathbf{r}) = \varepsilon_i\psi_i(\mathbf{r}) \tag{1.1.8}$$

in Hartree units. $\hat{V}_{nl}$, the non-local part of the ab initio ionic pseudopotential, is introduced to improve local-potential-based EPM given as [47]:

$$\hat{V}_{nl}(\mathbf{r}) = \sum_{\mathbf{R_i}} \hat{v}_{nl}(\mathbf{r} - \mathbf{R_i})$$

$$= \sum_{\mathbf{R_i}} \sum_{lm} |P_{lm}(\mathbf{R_i})\rangle \, v_l(|\mathbf{r} - \mathbf{R_i}|) \, \langle P_{lm}(\mathbf{R_i})| \, , \tag{1.1.9}$$

where $|P_{lm}(\mathbf{R_i})\rangle$ are projectors of angular momentum lm centred at the atomic positions $\mathbf{R_i}$. $\hat{V}_{SO}$ is the potential describing the non-local spin-orbit interaction for each atom type α in the system written as [48], [49]

$$\hat{V}_{SO} = \sum_{i\alpha} \hat{v}_{\alpha}^{SO}(R_i)$$

$$= \sum_{i\alpha} \sum_{lm} v_{l,\alpha}^{SO}(r - R_i) \times |P_{lm}(\mathbf{R_i})\rangle \, \mathbf{L} \cdot \mathbf{S} \, \langle P_{lm}(\mathbf{R_i})| \, , \tag{1.1.10}$$

where $\mathbf{L}$ is the spatial angular momentum operator, and $\mathbf{S}$ is the spin operator constructed from Pauli matrices. The wavefunctions $\psi_i(\mathbf{r})$ are expanded in terms of plane waves as:

$$\psi_i(\mathbf{r}) = \sum_{\mathbf{G}} c_i(\mathbf{G}) e^{\mathbf{i}(\mathbf{k}+\mathbf{G})\cdot\mathbf{r}}. \tag{1.1.11}$$

The Schrödinger equation is solved by combining the Eq. (1.1.6)-Eq. (1.1.11).

1.1.2 Configuration interaction

Configuration interaction (CI) is used to obtain the excitation where the correlation of ground state is decoupled from that of excited state. According to that, the single exciton wavefunction is given as [50], [51]:

$$\left|\Phi_{h_i,e_j}\right\rangle = b_{h_i}^\dagger c_{e_j}^\dagger |\Phi_0\rangle \, , \tag{1.1.12}$$

where i and j index hole and electron respectively, $b_{h_i}^\dagger$ is the creation operator for holes and $c_{e_j}^\dagger$ the creation operator for electrons, and $|\Phi_0\rangle$ the Slater determinants in the ground state. The

excitation wavefunctions $|\Psi\rangle$, hence, is expressed as:

$$|\Psi\rangle = \sum_{h_i, e_j} A(h_i, e_j) \left| \Phi_{h_i, e_j} \right\rangle, \tag{1.1.13}$$

where A are the expansion coefficients. The matrix elements between Slater determinants can be written as:

$$\left\langle \Phi_{h_i, e_j} \left| H \right| \Phi_{h_{i'}, e_{j'}} \right\rangle = \left(\varepsilon_{e_j} - \varepsilon_{h_i} \right) \delta_{h_i h_{i'}} \delta_{e_j e_{j'}} + \left\langle e_j h_{i'} \left| v \right| h_i e_{j'} \right\rangle - \left\langle e_j h_{i'} \left| v \right| e_{j'} h_i \right\rangle, \tag{1.1.14}$$

with

$$\left\langle e_j h_i \left| v \right| h_{i'} e_{j'} \right\rangle = \iint \psi_j^*(\mathbf{r}_e) \psi_i^*(\mathbf{r}_h) v(\mathbf{r}_e, \mathbf{r}_h) \psi_{i'}(\mathbf{r}_e) \psi_{j'}(\mathbf{r}_h) d\mathbf{r}_e d\mathbf{r}_h \tag{1.1.15}$$

where $v(\mathbf{r}_e, \mathbf{r}_h)$ is the screened Coulomb interaction given as:

$$v(\mathbf{r}_e, \mathbf{r}_h) = e^2 \int \epsilon^{-1}(\mathbf{r}_e, \mathbf{r}) |\mathbf{r} - \mathbf{r}_h|^{-1} d\mathbf{r}. \tag{1.1.16}$$

The dielectric function $\epsilon^{-1} = \epsilon_{el}^{-1} + \epsilon_{ion}^{-1}$ is divided into a high-frequency part (electronic contribution ϵ_{el}^{-1}) and a low-frequency part (ionic contribution ϵ_{ion}^{-1}) whose Fourier transforms are written as [51]

$$\epsilon_{el}^{-1}(k) = \frac{k^2 + q^2 \sin(k\rho_\infty)/(\epsilon_\infty k \rho_\infty)}{k^2 + q^2},$$

$$\epsilon_{ion}^{-1}(k) = \left(\frac{1}{\epsilon_0} - \frac{1}{\epsilon_\infty} \right) \left(\frac{1/2}{1 + \rho_h^2 k^2} + \frac{1/2}{1 + \rho_e^2 k^2} \right), \tag{1.1.17}$$

where q is the Thomas-Fermi wavevector, ϵ_∞ and ϵ_0 are the high-frequency and low-frequency dielectric constants respectively, ρ_∞ the solution of $\sinh(q\rho_\infty)/(q\rho_\infty) = \epsilon_\infty$ and $\rho_{h,e} = (\hbar/2m_{h,e}^* \omega_{LO})^{1/2}$, with $m_{h,e}^*$ the hole and electron effective masses and ω_{LO} the bulk longitudinal-optical-phonon frequency.

1.1.3 Observables calculation

Optical absorption

Optical absorption is relative to the transition of an exciton between the initial state i and final state f along with the annihilation of an electron-hole pair. The optical transition dipole matrix

element of an excitonic complex χ to the excitonic complex $\chi - 1$ given as:

$$M_{if}^{\hat{e}}(\chi) = \left\langle \Psi^{(f)}(\chi - 1) \middle| \hat{e} \cdot \mathbf{p} \middle| \Psi^{(i)}(\chi) \right\rangle, \tag{1.1.18}$$

where $\mathbf{p}$ is the momentum operator and $\hat{e}$ the polarization vector of the electromagnetic field [52], [53]. The oscillator strength characterized by χ and $\hat{e}$ is expressed as:

$$\alpha^{(\hat{e})}(\omega, T; \chi) \propto \sum_{i,f} |M_{if}^{\hat{e}}(\chi)|^2 P_i(T; \chi) \delta\left(\omega - \omega_{if}(\chi)\right) \tag{1.1.19}$$

where $P_i(T; \chi)$ is the occupation probability of $\left| \Psi^{(i)}(\chi) \right\rangle$ at temperature T and is given as:

$$P_i(T; \chi) = N \exp\left\{ -\left[E^{(i)}(\chi) - E^{(0)}(\chi) \right] / k_B T \right\}, \tag{1.1.20}$$

and N is a normalization constant determined by requiring $\sum_i P_i = 1$.

Radiative lifetime

The radiative lifetime τ_{if} for the transition from the excited state $\Psi^{(i)}$ to the ground state $\Psi^{(f)}$, is obtained in the framework of standard time-dependent perturbation theory as [54]:

$$\frac{1}{\tau_{if}(\chi)} = \frac{4nF^2 \alpha \omega_i^3}{3c^2} |M_{if}|^2, \tag{1.1.21}$$

where α is the fine structure constant, n the refractive index of the surrounding medium, ω_i the frequency of the emitted photon, c the speed of light, and $F = 3\varepsilon / (\varepsilon_{dot} + 2\varepsilon)$ is the screening factor with $\varepsilon = n^2$. The quantum dot dielectric constant ε_{dot} is obtained from a modified Penn model as [51]:

$$\varepsilon_0^{dot}(R) = \varepsilon_\infty^{dot}(R) + (\varepsilon_0^{bulk} + \varepsilon_\infty^{bulk}) \tag{1.1.22}$$

and

$$\varepsilon_\infty^{dot}(R) = 1 + (\varepsilon_\infty^{bulk} - 1) \frac{\left[E_{gap}^{bulk} + \Delta E \right]^2}{\left[E_{gap}^{dot}(R) + \Delta E \right]^2} \tag{1.1.23}$$

for low and high frequency respectively, where $\varepsilon_0^{bulk}(\varepsilon_\infty^{bulk})$ is the bulk low (high) -frequency dielectric constant, E_{gap}^{dot} is the bandgap energy in the quantum dot, and ΔE is the energy difference between the bulk bandgap E_{gap}^{bulk} and the energy of the first pronounced peak in the bulk absorption spectrum. The thermally averaged lifetime is calculated by assuming Boltzmann

occupation of higher-energy excitation levels as:

$$\frac{1}{\langle \tau \rangle} = \frac{\sum_i (1/\tau_i) e^{-\Delta E_i / K_B T}}{\sum_i e^{-\Delta E_i / K_B T}} \tag{1.1.24}$$

Auger lifetime

A general phenomenological formula for the Auger rates can be derived under the standard time-dependent perturbation theory as:

$$W_i = \frac{\Gamma}{\hbar} \sum_n \frac{|\langle i|\Delta H|f_n\rangle|^2}{(E_{f_n} - E_i)^2 + (\Gamma/2)^2}, \tag{1.1.25}$$

where E_i and E_{f_n} are the eigenenergies of the initial $|i\rangle$ and final $|f_n\rangle$ Auger electronic states, ΔH is the Coulomb interaction, and $\hbar/\Gamma$ is the lifetime of the final states.

Auger cooling (AC) is responsible for the extremely efficient electron thermalization observed in nanocrystals, which occurs via an electron-hole scattering mechanism, where a hot electron in the energy level ϵ_{e_p} relaxes to the ground state (ϵ_{e_s}) by transferring its excess energy to a hole in its ground state (ϵ_{h_s}) and exciting it to a deeper state (ϵ_{h_n}). The AC rate derived from Eq. (1.1.25) is written as [55]

$$\tau^{-1} = \frac{\Gamma}{\hbar} \sum_{n\alpha} \frac{|J(h_s, e_p; h_n, e_s)|^2}{(\Delta E + \epsilon_{h_n} - \epsilon_{h_s})^2 + (\Gamma/2)^2}, \tag{1.1.26}$$

where n is the number of final states included in the calculation with the spin specified by the symbol $\uparrow$ and $\downarrow$, $\Delta E = \epsilon_{e_p} - \epsilon_{e_s}$ is the energy decrease of the electron, and the Coulomb integral $J(j, k, l, m)$ is given as:

$$J(j, k, l, m) = \sum_{\sigma,\sigma'} \int \int \phi_j^*(\mathbf{r},\sigma) \phi_k^*(\mathbf{r}',\sigma') \frac{e^2}{\bar{\epsilon}(\mathbf{r},\mathbf{r}')|\mathbf{r} - \mathbf{r}'|} \phi_l(\mathbf{r},\sigma)\phi_m(\mathbf{r}',\sigma')d^3rd^3r' \tag{1.1.27}$$

where ϕ_i is the single-particle wave function, and $\bar{\epsilon}(\mathbf{r},\mathbf{r}')$ is the dielectric function changing from $\bar{\epsilon}_{in}(\mathbf{r},\mathbf{r}')$ within the nanostructure, to 1, outside it, according to

$$\frac{1}{\bar{\epsilon}(\mathbf{r},\mathbf{r}')} = 1 + \left(\frac{1}{\bar{\epsilon}_{in}(\mathbf{r},\mathbf{r}')} - 1\right) m(r)m(r'), \tag{1.1.28}$$

where $m(r)$ is a mask function ranging from 1 (inside the dot) to 0 (outside the dot).

Auger recombination (AR) is another Auger process, where the recombination of an electron-

hole pair in the presence of excess electrons and/or holes is accompanied by a (non-radiative) energy transfer to one of the 'spectator' particles, which is excited to a higher energy state. The decay rates for hot electron and hot hole in Auger recombination are expressed as [55]:

$$\frac{1}{\tau_e} = \frac{1}{\hbar} \sum_n \frac{\Gamma}{(\epsilon_{gap} - \epsilon_{e_n} + \epsilon_{e_s})^2 + (\Gamma/2)^2} \times |J(e_{s,\uparrow}, e_{s,\downarrow}; e_n, h_s) - J(e_{s,\downarrow}, e_{s,\uparrow}; e_n, h_s)|^2 \qquad (1.1.29)$$

and

$$\frac{1}{\tau_h} = \frac{1}{\hbar} \sum_n \frac{\Gamma}{(\epsilon_{gap} - \epsilon_{h_n} + \epsilon_{h_s})^2 + (\Gamma/2)^2} \times |J(h_{s,\uparrow}, h_{s,\downarrow}; h_n, e_s) - J(h_{s,\downarrow}, h_{s,\uparrow}; h_n, e_s)|^2 \qquad (1.1.30)$$

respectively, where the subscript $\uparrow, \downarrow$ indicates the spin-degenerate Kramer doublets, and ϵ_{gap} is the energy gap between VBM and CBM. The total lifetime for the Auger recombination is calculated as:

$$\frac{1}{\tau_{e-h}^{2 \to 1}} = \frac{2}{\tau_e} + \frac{2}{\tau_h} \qquad (1.1.31)$$

Chapter 2

Inverse-designed semiconductor nanocatalysts for targeted CO_2 reduction in water

2.1 Introduction

The importance of improving air quality in our cities is becoming increasingly clear, not only for obvious environmental reasons and to mitigate the effects of global warming, but also for health concerns as climate change has been shown [56] to directly promote or aggravate respiratory diseases, which, in turn, increase vulnerability to viral infections, such as Covid-19.

Carbon dioxide (CO_2) is the primary greenhouse gas emitted through human activities, accounting for over 80% of all human-related greenhouse gas emissions in 2018 in the US alone, and for over 65% globally [57], having increased from about 6.5 billion metric tonnes in 2000 to over 10 in the last decade [58], its main source being the combustion of fossil fuels for transportation and energy.

One of the most promising techniques to decrease environmental CO_2, apart from capture and sequestration, is its photocatalytic reduction. Such processes exploit semiconductor materials as catalysts to chemically reduce CO_2, generally in the presence of water. The main products are CH_4, CH_3OH, CO and $HCOOH$ (in order of increasingly negative potential vs normal

hydrogen electrode - NHE). Other products, derived from the C-C coupling reaction, do not exhibit comparable activity and selectivity, because the corresponding reduction reactions are thermodynamically unfavourable [59] and consume different numbers of electrons and protons [60]. The main steps for this reaction to take place are [61]: (i) light absorption and photogeneration of electron-hole pairs; (ii) carrier migration to the catalyst's surface; (iii) reduction of CO_2 by the electron and oxidation of H_2O (to O_2) by the hole. The efficiency of the CO_2 reduction is therefore determined by the efficiency of the following processes: (i) light harvesting, (ii) charge separation; (iii) surface reaction. Semiconductors are good light absorbers for photons of sufficiently high energy to exceed the bandgap [52] (i), and, through nanostructuring, their energy bands can be engineered [62] both to enhance their light harvesting properties [63] and to correctly match the redox potentials for specific reactions [61] (iii), e.g., so that their conduction band minimum - CBM - be located above the redox potential for CO_2 reduction, and their valence band maximum - VBM - be below the redox potential for H_2O oxidation[61]. Furthermore, long carrier lifetimes can be obtained in indirect-band materials [52], so that the photogenerated electron and hole do not recombine (ii) before reaching the surface and reacting with CO_2 and H_2O. Alternatively, carrier separation (ii) can easily be achieved in type II heterostructures, by combining two materials with suitably chosen band structures, or at the interface between different crystalline phases of the same material [64]–[66]. It is therefore not surprising that semiconductors have become increasingly popular catalysts for CO_2 reduction [59], [61], [67].

Historically TiO_2 has been the material of choice for this reaction due to its low cost, non-toxicity, stability against photoirradiation, and chemical inertness [68]. However, TiO_2 is far from ideal for this application: for example, as bulk TiO_2 absorbs in the near UV [69] (and at even higher energies when nanostructured), it can convert only a fraction (3-4% at most) of the available solar photons into electron-hole pairs, resulting in poor light harvesting efficiency (i). Furthermore, the carriers' recombination times in bulk TiO_2, varying from sub-ps [70] to a few tens of ns [71], are fast compared with typical redox reaction times, leading to reduced charge separation efficiencies (ii). It should therefore not be impossible to find a material that can surpass TiO_2's photocatalytic efficiency and replace it as catalyst of choice for CO_2 reduction.

This is precisely what we set out to do in this chapter: to apply inverse-design principles [72] to engineer a semiconductor nanocatalyst with potential for unprecedented efficiency for the

following reaction

$$CO_2 + 8H^+ + 8e^- \rightarrow CH_4 + 2H_2O \qquad (2.1.1)$$
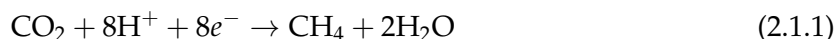
i.e., CO_2 reduction to CH_4. We choose this specific reaction because, having the least negative redox potential, the formation of CH_4 is thermodynamically the most favourable of all most common CO_2 reduction reactions [61]. However, it is a complex reaction and may involve intermediate steps [60]: indeed three different pathways are commonly reported in the literature for CO_2 methanation [73], [74], involving dissociation into CO (carbide pathway), synthesis of HCOO (formate pathway), or COOH (carboxyl pathway), depending on the specific catalyst and on the reaction conditions. Nevertheless, there are many examples of nanostructured semiconductor photocatalysts that produce CH_4 as a main (see, e.g., the review by Xie *et al.* [61]), or even exclusive [75] product of CO_2 reduction in water. Furthermore, a study by Yui *et al.* [76] has concluded that CO_2 can be reduced to CH_4 at a single site through an 8-electron process, rather than at two separate sites, first through a 2-electron and then through a 6-electron process. Indeed, the different C, H and O affinities of a photocatalyst can heavily affect the adsorption/desorption of reactants/intermediates and the sequence of hydrogenation and deoxygenation, resulting in different product pathways and selectivities [77].

Unfortunately, however, reaction (2.1.1) is *kinetically* less favourable than the competing reduction of water

$$2H^+ + 2e^- \rightarrow H_2 \qquad (2.1.2)$$

which has a comparable (although slightly higher) redox potential but only requires two electrons, instead of eight. The reduction of CO_2 to CH_3OH has a very similar reduction potential (see maroon dashed line in Fig. 2.2), but, involving six electrons, is kinetically less favourable than that of water (There are other possible CO_2 reduction reactions, involving C_{2+} products - ethylene, ethanol, propanol, ethane - with intermediate potentials between those of reactions (2.1.1) and (2.1.2), however, they all involve greater changes in both Gibbs free energy and standard enthalpy [59], making them thermodynamically less favourable). Therefore (1) thermodynamic selectivity for CO_2 reduction vs the competing H_2O reduction [60] (which would, at the same time also ensure selectivity vs CO_2 to CH_3OH reduction), and (2) availability of eight isoenergetic electrons at one time for the $CO_2 \rightarrow CH_4$ reaction, are essential attributes to the ideal catalyst. Indeed, as in all three common methanation pathways mentioned above the redox potential for the initial step is higher than that for water reduction (2.1.2) [61], property

(1) would also ensure selectivity for direct CH_4 formation. We note that TiO_2 can provide no such selectivity, as the position of its bulk CBM is higher than the redox potential for water reduction [61]. Furthermore, the presence of a noble or coinage metal co-catalyst (often used to increase the rate of CH_4 formation) was observed [78] to enhance the formation of H_2 more than that of CH_4, leading to an even poorer selectivity of the reacted electrons for CO_2 reduction. It is worth stressing the importance of achieving high selectivity, as the formation of undesired byproducts (a) subtracts precious photogenerated electrons from the main reaction, lowering the yield of the target products, and (b) raises the challenging problem of separating the different products from the resulting mixture [60].

Size and shape of the catalyst also play a fundamental role in determining its efficiency. In the case of TiO_2 nanoparticles with diameters between 4.5 and 29 nm, for instance, the highest yields were obtained with a size of 14 nm [79]. This was interpreted as the result of a competition between two main factors: surface area (determining the availability of surface sites for CO_2 adsorption), and band-gap-dependent light absorption efficiency [79]. It would therefore be beneficial to be able to decouple the catalyst's size, or, more specifically, its surface area, from its band gap. Indeed, independently increasing the volume, while keeping a nearly constant band-gap, will also increase absorption through an increase in the absorption cross section. This leads to the next entries in the 'wish-list' for our ideal catalyst: (3) a large contact area for CO_2 adsorption and reaction with the electrons and (4) the possibility to tune the band gap independently from it. Also desirable would be (5) the availability of electrons and holes at different locations on the surface for the two redox reactions to take place. Finally, we would like properties (i)-(iii) and (1)-(5) to be exhibited over a wide size window. In other words, it should be possible to produce catalysts with these properties using chemical growth methods with realistic size dispersions.

In what follows we will show that a catalyst exhibiting all requisites to be able to efficiently reduce CO_2 to CH_4, plus the 'wish-list' attributes listed above (including the ability to deliver eight electrons in one go), exists and can be synthesized with the present experimental capabilities, making it a potential game-changer of the CO_2 reduction technology. We start by focussing on property (2), as it is the most crucial requisite enabling the achievement of high reduction efficiencies, and is, nevertheless, not featured by any of the photocatalysts in use today. In order to be able to deliver eight electrons, all at a given potential, a four-fold
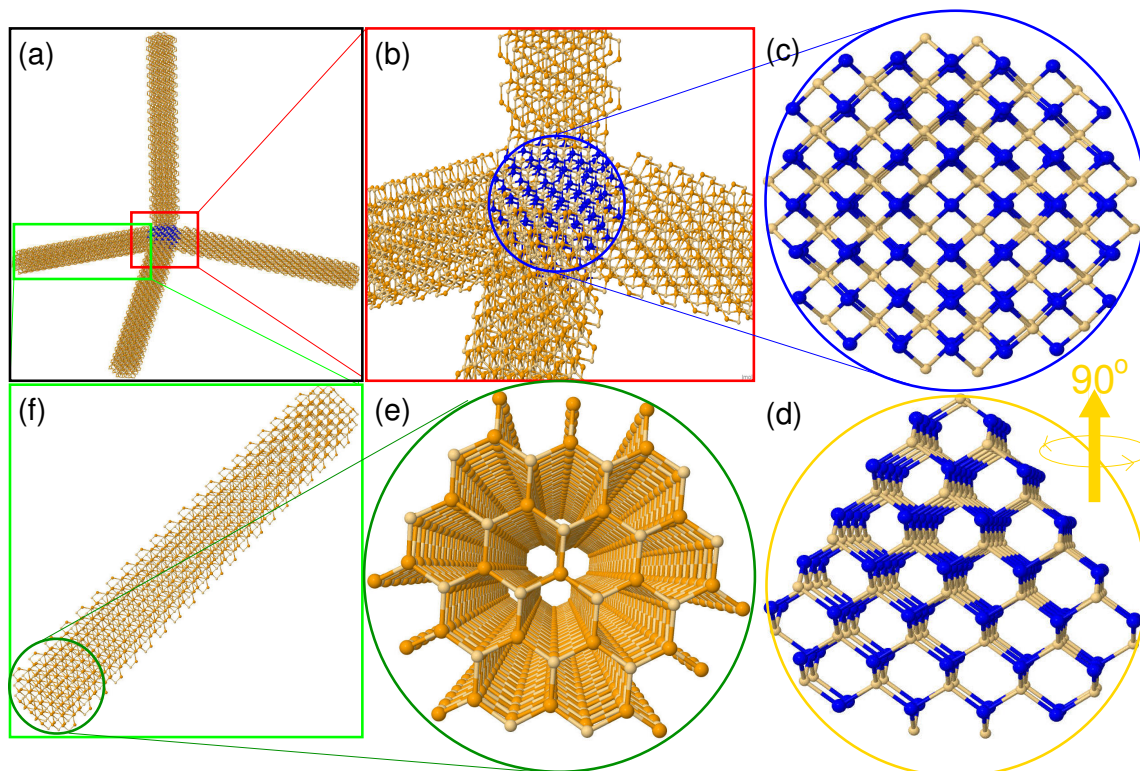
Figure 2.1: Our CdTe/CdSe core/arm tetrapods (a) have a central zinc blende tetrahedral core with four (111) facets made of CdTe, (b)-(d), from which four wurtzite CdSe rod-like arms protrude, (e)-(f).

degenerate ground state is needed. There are two possible strategies to achieve this goal: engineering the material's band structure or its shape. A bulk material with its CBM at the L point in the Brillouin zone would guarantee the required four-fold degeneracy for the ground state. However its absorption efficiency (i) may be low, as its band gap is likely to be indirect. PbSe could be a good candidate, as its VBM is also located at the L point, making it a peculiar direct-band-gap material [80]. However, bulk PbSe absorbs in the infra-red (i.e., not where the solar irradiance peaks, (i)) and its band structure does not satisfy (iii), one of the fundamental requirements for CO_2 reduction, as its CBM lies *below* the redox potential for that reaction. Nanostructuring could solve this problem (but only for very small dot sizes with $R \leq 1$ nm [62]), at the expense, however, of reducing considerably the surface area available for CO_2 adsorption and of losing the four-fold degeneracy of the CBM[1]. A better alternative is shape engineering: a nanostructure with four identical regions where the CBM is localised would ensure its four-fold degeneracy. At the same time, such a structure would also enable the simultaneous absorption of eight photons. A tetrapod (TP, see Fig. 2.1) [41], [81], is there-

---

[1]According to our calculations [62], the energy separation from the CBM of the next two states (CBM+1 and CBM+2) is about 10 meV, becoming about 100 meV for CBM+3.

2.1. Introduction
Chapter 2. Inverse-designed semiconductor
nanocatalysts for targeted CO_2 reduction in water

fore what we will focus on. Unfortunately, however, in a TP made of a single material, due to the type II band alignment between the zinc-blende core and the wurtzite arms (both CBM and VBM in the bulk wurtzite structure are higher than those in the bulk zinc-blende structure for the same material), the CBM is always localised in the core, not in the four arms [41], [81], [82]. In order to achieve the desired localisation in the arms, the core should be made of a different material having a higher CBM than the arm material. Step (ii) - charge separation and long carrier lifetimes - can be achieved if the core material also has a higher VBM than the arm material, resulting in core-confined holes, and hence in their spatial separation from the electrons. Such a structure would also ensure electrons and holes to be available at different locations on the surface for the two redox reactions to take place (property (5)), and, provided the arms were suitably long, a large contact area to be available for CO_2 adsorption and reaction with the electrons (property (3)), and a large absorption cross section, enabling the simultaneous absorption of eight solar photons. Finally, in TPs, attribute (4) is easily satisfied, as the band gap has been shown [41], [81], to be largely independent of the arm length. Selectivity vs H_2O reduction (attribute (1)) is also crucial and can be achieved by careful engineering of the core size and arms diameter.

Heterostructured (or core/arms) TPs of different materials (ZnTe/CdSe [83], ZnTe/CdS [83], [84], ZnTe/CdTe [85], ZnSe/CdS [84], CdSe/CdS [86], CdSe/CdTe [85]) have been synthesized experimentally for over 10 years [42], the seeded growth approach being the most successful method for fabricating more uniform and reproducible structures. Among the different core/arm material pairs, the most popular is CdSe/CdS [86], where the type I band alignment existing between the CdSe core and the CdS arms [87] is exploited to funnel to the core region the electron-hole pairs photogenerated in the arms, endowing these structures with excellent light-harvesting properties that make them ideally suited for applications such as light concentrators, solar cells, and LEDs. According to their bulk band structure, ZnTe/CdTe TPs are also expected to exhibit a type I band alignment [87], however, with both electrons and holes localised in the arms. Unfortunately, as it was discussed above, this kind of band alignment does not suit our purpose as it does not promote charge separation. Furthermore, a high density of structural defects, with alternating regions of wurtzite and sphalerite phases, was recently identified in nanostructures whose arms were made of CdTe by both HRTEM analysis and theoretical modelling [85]. Due to the different position of the band edges in zinc-blende and wurtzite, the presence of such mixed phases creates local potential wells that could trap the

electron, preventing it from reaching the surface and react with CO_2.

ZnTe/CdSe, ZnTe/CdS and ZnSe/CdS have all a type II (or quasi-type II, in the case of ZnSe/CdS) band alignment in the bulk [87], and hence the electron is expected to be confined in the arms and the hole in the core (or throughout the whole structure for ZnSe/CdS). The position of their CBM in the bulk is also above the redox potential for CO_2 reduction, making them good candidates as catalysts for this reaction. It has been recently observed [88] that, in mixed cation materials such as these, substantial cation exchange takes place in the core, yielding alloyed structures. The quantum fluorescence emission/absorption spectra and the electronic structure could be tuned by carefully selecting the alloy composition [89]–[91]. Unfortunately, however, The exact composition (hence band alignment) of alloyed structures is difficult to predict and control. Moreover, as the location of the CBM in bulk CdS is already above the redox potential for H_2O reduction, TP catalysts with CdS arms can exhibit no selectivity (1) vs this reaction.

Considering same-cation hetero-nanostructures, CdSe/CdTe TPs have a type II band alignment, but with the electrons confined to the CdSe core. As CdSe can be grown as both seed and arms material and CdTe is also suitable to be grown as seed [85], a possible choice yielding a type II structure with the desired carrier localisation is a CdTe/CdSe [92] TP.

Furthermore, as the ability to chemisorb CO_2 plays a crucial role in the efficiency of its photocatalytic reduction to CH_4, and since surface functionalization with organic amines has been proved a successful strategy to enhance such chemisorption in the case of TiO_2 [93], the use of CdSe as arm material, for the surface of which a variety of amine groups can routinely be employed as passivants [62], [94], could be an effective choice to further enhance the photocatalytic reduction efficiency in these hetero-nanostructures.

2.2 Results and Discussion

We modelled CdTe/CdSe hetero-nanostructures with different arm diameters D (from 1.9 nm to 2.8 nm) and arm lengths L (from 3.5 nm to 14 nm), and the structural relaxation that may occur at the core/arms junction and at the surface is neglected here. All our energies are calculated with respect to vacuum. The calculations were performed using periodic boundary conditions in which the unit cell (in this case called a "supercell") contained the whole TP and

Structure	D (nm)	L (nm)	Volume (atoms)
TP1	1.9	14	7027
TP2	2.1	14	8115
TP3	2.8	7.0	8005
TP4	2.1	3.5	2227
TP5	2.8	3.5	4289
TP6	1.9	3.5	1907

Table 2.1: The structures considered in this chapter (diameter D, length L and number of atoms). Color highlights common features.

sufficient vacuum around it to avoid wave function overlap between neighbouring supercells. For simplicity and ease of notation we will refer to these structures as TPn: TP1 and TP2 have the same arm length $L = 14$ nm, but different diameters (1.9 nm and 2.1 nm), hence different volumes (TP1 with 7027 atoms and TP2 with 8115 atoms [2]); TP3 has shorter ($L = 7$ nm, i.e., half the length of TP1 and TP2), but thicker ($D = 2.8$ nm) arms, and a volume (8005 atoms) only slightly smaller than TP2; TP4 has the same arm diameter as TP2 ($D = 2.1$ nm) but a quarter of its length ($L = 3.5$ nm), and nearly a quarter of its volume (2227 atoms); TP5 and TP6 have the same diameters as, respectively, TP3 ($D = 2.8$ nm) and TP1 ($D = 1.9$ nm), but shorter arms than both ($L = 3.5$ nm) yielding volumes of 4289 and 1907 atoms, respectively (see Table 2.1). These nanostructures cover therefore a wide range of aspect ratios L/D, from 1.25 to 7.27. We note that, although initial attempts to grow CdTe/CdSe core/arms TPs yielded structures with short, tapered arms [85], in principle the seeded growth method has the potential to produce CdTe/CdSe with the characteristics modelled in this chapter, provided suitable mixtures of surfactants are employed. We hope that the present study will spur further research to improve the synthetic processes, leading to the same degree of control that is available with TP made of other materials [85].

We selected TPs whose CBM was above the redox potential for CO_2 reduction, but, at the same time, lower than the redox potential for the reduction of H_2O to H_2 (see top dashed lines in Fig. 2.2). This ensures the required selectivity vs water reduction (property 4), which is expected to be suppressed in these nanostructures by virtue of their band structure alone. In contrast, other semiconductor nanostructures usually require some degree of surface manipulation to enhance their photocatalytic reduction yields of CO_2 in the presence of H_2O. As a consequence, unlike with TiO_2 [78] or other semiconductors, in the case of CdTe/CdSe

---

[2]We employ atom numbers to unequivocally express the volume, as opposed to using conventional units of nm^3, as volume estimates that use the latter are based on an assumed perfect geometrical (i.e., usually cylindrical) shape for the arms, that is never realised at the atomistic level.

core/arms TPs the use of both solid-liquid or solid-vapour reaction modes should be possible
and should yield similar rates of CH_4 formation, adding further flexibility to the design of the
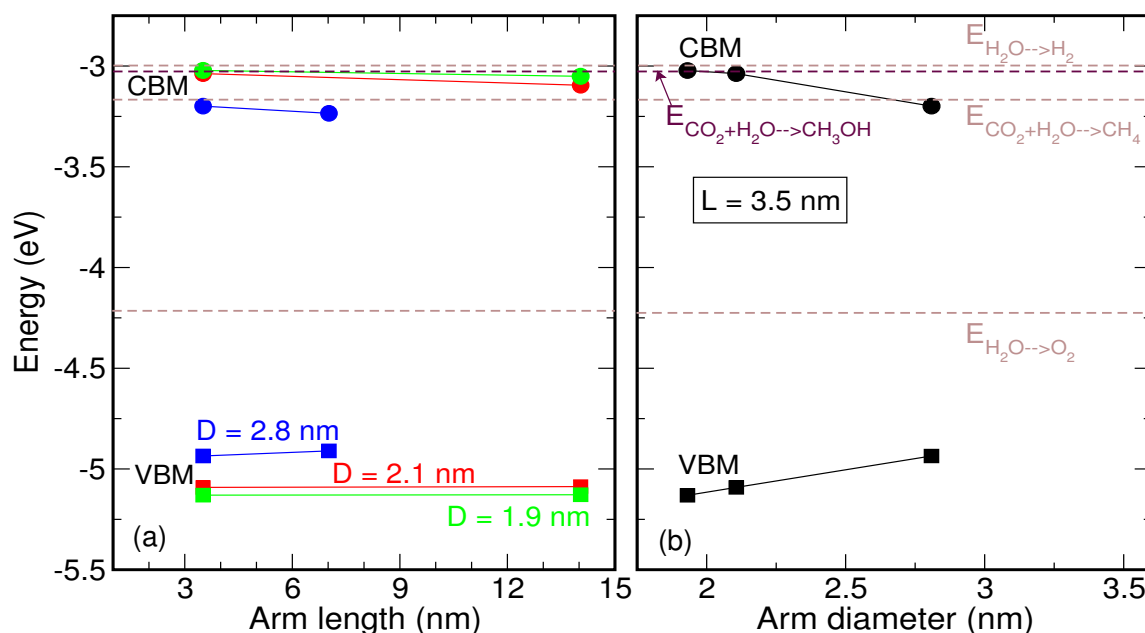reactor.

Figure 2.2: Valence (squares) and conduction (circles) band edge energies, calculated with re-
spect to vacuum, as a function of TP size: (a) arm length L, for different values of the diameter
$D = 1.9$ nm (green symbols), 2.1 nm (red symbols) and 2.8 nm (blue symbols); (b) arm diame-
ter D, for $L = 3.5$ nm (black symbols). The solid lines are a guide to the eye. The dashed lines
mark the position of the redox potentials for the reduction of H_2O to H_2 (-2.997 eV, top brown
line), the reduction of CO_2 to CH_3OH (-3.027 eV, maroon line) and to CH_4 (-3.167 eV, middle
brown line), and the oxidation of H_2O to O_2 (-4.215 eV, bottom brown line), at pH=7. Their
position relative to vacuum was obtained by shifting the values reported in Ref.[61] (Figure
2) using as a reference level our calculated position of the CBM of bulk CdSe [3] (-3.49 eV, also
confirmed experimentally [62]).

The results presented in Fig. 2.2 also suggest that the TP geometry can be easily engineered for
the position of its CBM to lie above (i.e., to be more negative vs NHE than) the reduction poten-
tial of other catalytic reactions for CO_2 reduction (e.g., to CH_3OH, HCHO, CO, and HCOOH,
in order of increasingly negative potentials). This will, however, inevitably compromise all
selectivity, as water reduction (and CH_4 formation) will be competing with those reactions.

We want to emphasise the importance of accurate band edge engineering in these systems, an
example of which is provided by the comparison between the photocatalytic performance of
commercial WO_3 microcrystals and nanosheets of the same material: the former, whose CBM

---

[3]In other words, Ref [61] provides the position of the CBM of bulk CdSe at pH=7. We calculated the position of
the CBM in bulk CdSe with respect to vacuum. The difference between these two positions was used to shift the
reduction potentials from Ref [61] and obtain them with respect to vacuum in our plots.

is 0.29 eV more positive than the reduction potential of CO_2 to CH_4, could produce no CH_4;

the latter, however, whose CBM, owing to increased confinement, is 0.47 eV higher than that

of the microcrystals (and just 0.18 eV higher than the CO_2/CH_4 reduction potential) resulted

in successful catalysis of CO_2 into CH_4 [95]. Similarly, in the case of $Na_2V_6O_{16}$ nanoribbons

[96] successful CO_2 reduction to CH_4 in water was achieved despite their CBM position being

just 0.17 eV above the CO_2/CH_4 reduction potential.

Very recently, spherical CdSe nanocrystals (NCs) exhibited remarkable size-tunable selectivity

in the photocatalytic reduction of CO_2 [97]. Li and co-workers showed [97] that, by varying the

NC size, the position of the CBM could be tuned to lie between the potential for H_2 evolution

and that for CH_3OH generation, resulting in over 70% selectivity towards the latter product.

They also found that the observed potentials for both reactions (defined as *'the potentials at

which the electron has just started H_2 and CH_3OH production'*) were more reducing than the theo-

retical values. In particular the difference between the observed potential for CO_2 reduction to

CH_3OH (~ -0.4 V vs NHE [97]) and its value at pH 7 (-0.38 V vs NHE [59], [61]), attributed by

the authors [97] to kinetic factors including the activation energy and the overpotential, was

only ~ 0.02 V. Furthermore, they reported the presence of considerable amounts of CH_4 in the

reaction products, which were independent of the NC size, as the potential for CO_2 reduction

to CH_4 is far below the position of the NCs' CBM, for all sizes considered in the experiment

[97]. Interestingly, for NC sizes sufficiently large that no CH_3OH was produced, (i.e., when the

CBM dropped below the potential for CO_2 reduction to CH_3OH), the selectivity achieved for

CH_4 was 79% [4]. These results suggest that much higher selectivities for CO_2 reduction to CH_4

should be achievable by carefully engineered CdTe/CdSe TPs with suitable arm size and CBM

position. Very importantly, they also provide an estimate for the magnitude of the activation

energies and overpotentials for such a reaction (~ 0.02 V) in these nanostructures.

We verified that the TP's CBM originated from the CdSe arms and the VBM from the CdTe core

by decomposing each structure into an isolated CdTe core and an isolated CdSe arm, and run

electronic structure calculations on each separately. In other words, we run two separate cal-

culations, one for an isolated CdSe rod (the TP arm) and one for an isolated CdTe tetrahedron

(the TP core) (see Fig. 2.3).

---

[4]We calculate the selectivity S as $S_{CH_4} = 8R_{CH_4}/(2R_{CO} + 6R_{CH_3OH} + 8R_{CH_4} + 2R_{H_2})*100\%$, where R represents
the productive rate of the observed products (in the specific case: CO, CH_3OH, CH_4 and H_2), and its coefficient is
the number of electrons consumed in the multi-electron reaction [60].

As a consequence, we found that in all TPs considered: (a) the holes are confined in the core, whereas the electrons are localised in the arms (Fig. 2.4), as desired; (b) the band gap is smaller than that of both core and arm (but still in the visible region of the spectrum), and can be tuned over a wide range of energies by an appropriate choice of core and arm sizes.
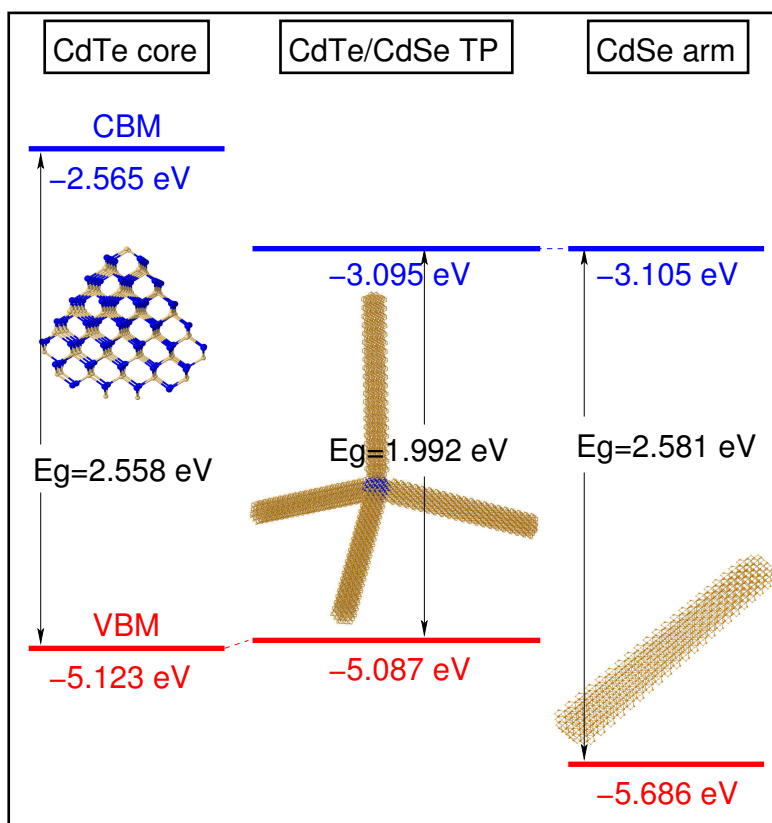

Figure 2.3: Valence and conduction band edge energies, calculated with respect to vacuum, for a CdTe core (left), a CdTe/CdSe core/arms TP (centre), and a CdSe arm (right), with D = 2.1 nm and L = 14 nm, showing the origin of the TP's band edges to be the core (for the VBM) and the arm (for the CBM). [The slight difference in the position of the VBM in core and TP is due to the fact that, in the latter, the confinement provided by the CdSe arms is weaker than that provided by the capping groups in the core only case]. As a consequence, the band gap in type II heterostructures can be smaller than that of both core and arm.
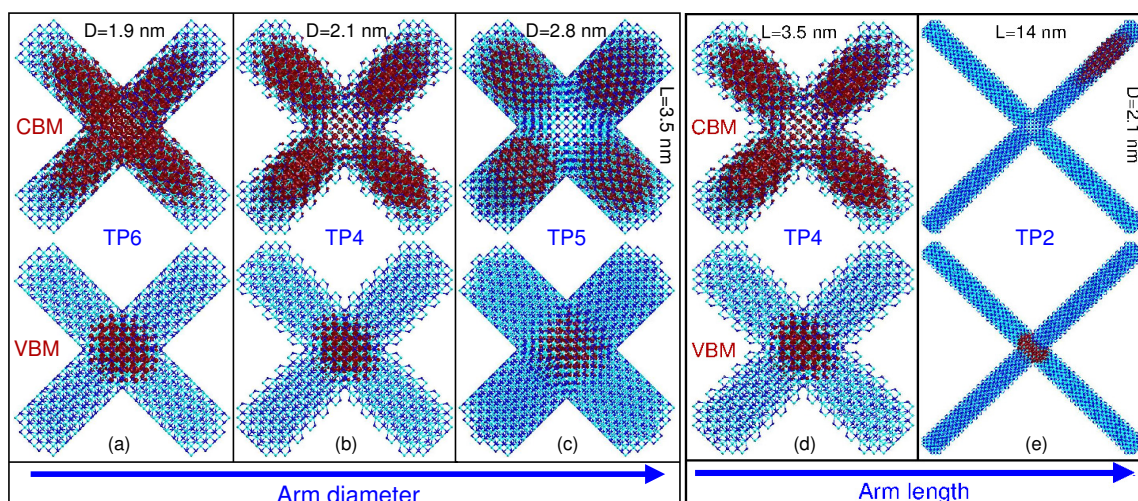
Figure 2.4: Valence (bottom) and conduction (top) band edge charge densities (red), calculated for different values of the arm diameter $D = 1.9$ nm (a), 2.1 nm (b) and 2.8 nm (c), for $L = 3.5$ nm, and for different values of the arm length $L = 3.5$ nm (d) and 14 nm (e), for $D = 2.1$ nm. Cyan dots represent Cd, blue dots represent Se and Te atoms.

However, structures with small diameters ($D \lesssim 2.1$ nm) and short arm lengths ($L \lesssim 3.5$ nm), exhibit two features that would affect their exploitation as efficient photocatalysts: (I) a considerable portion of the CBM charge density is found in the core (Fig. 2.4); (II) the CBM does not exhibit the expected four-fold degeneracy (Fig. 2.5 and Fig. 2.6).
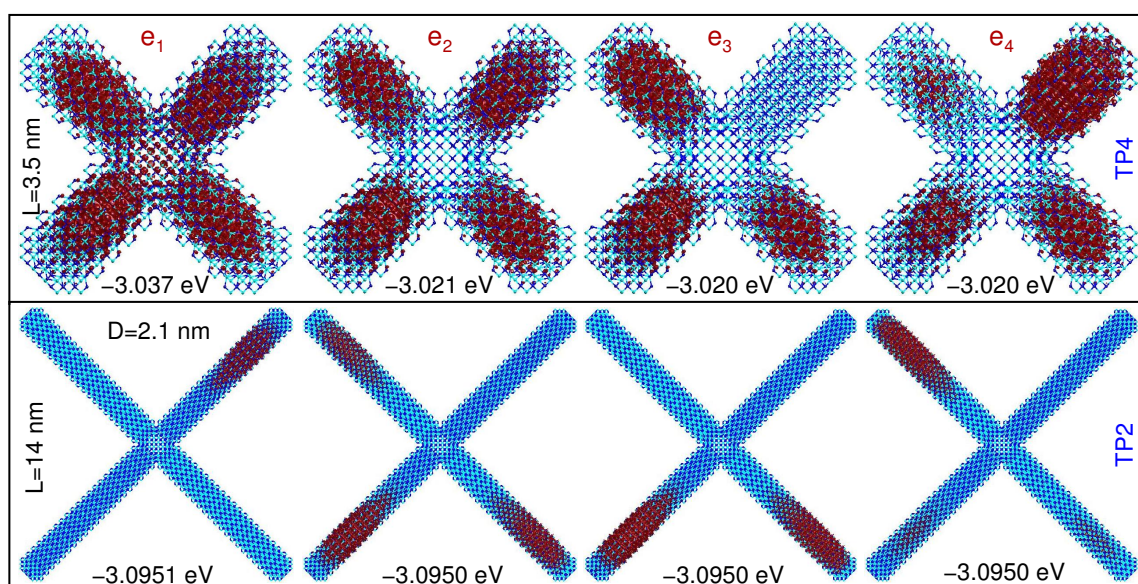

Figure 2.5: Lowermost four conduction band state charge densities (red), calculated in TPs with $D = 2.1$ nm and (top) $L = 3.5$ nm (TP4), and (bottom) $L = 14$ nm (TP2). Also reported are the corresponding energies, relative to vacuum. Cyan dots represent Cd, blue dots represent Se and Te atoms.

The large overlap between ground state electron and hole wave functions resulting from (I)

yields radiative recombination times of the same order of magnitude (i.e., tens on ns), as those observed in CdSe nanocrystals of similar diameters or calculated for CdTe TPs with similar dimensions (Fig. 2.7); whereas, as a consequence of (II), some of these nanostructures may fail to simultaneously deliver the eight isopotential electrons needed for an efficient CO_2 reduction. It has to be noted that, although the energy separation $\Delta E_{cb_{1-4}}$ between the first (cb_1 = CBM) and the fourth (cb_4 = CBM+3) electron state of all of these nanostructures is much smaller than in spherical nanocrystals with similar diameters (about 600 meV in CdSe), where it is much larger than the difference between the redox potentials for CO_2 and H_2O reduction, it may still lead (especially for TPs with thinner arms) to a loss of selectivity (4): i.e., if the energy of the excited electron is above the redox potential for water reduction (top dashed line in Fig. 2.2), the latter reaction will be more likely to occur than the reduction of CO_2 (if considering the two to eight electron ratio for the two reactions). We also note that, although the large separation $\Delta E_{cb_{1-4}}$ in spherical structures can be reduced by increasing the nanocrystal's radius, this occurs at the expense of lowering the position of the CBM and decreasing the band gap. In the case of CdSe, for example, the radius increase needed to reduce $\Delta E_{cb_{1-4}}$ below 100 meV leads to a lowering of the CBM of over 600 meV (which brings it below the redox potential for CO_2 reduction) and to a decrease of the band gap of over 1 eV [62].
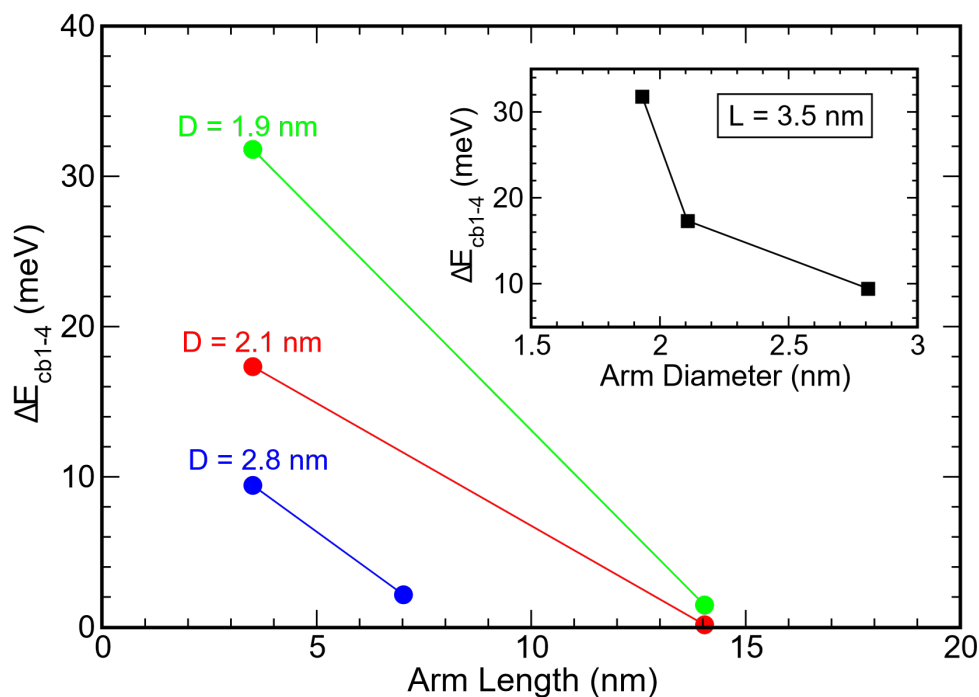

Figure 2.6: Energy separation $\Delta E_{cb_{1-4}}$ between the first (cb_1 = CBM) and the fourth (cb_4 = CBM+3) electron state as a function of TP size: arm length L, for different values of the diameter D = 1.9 nm (green symbols), 2.1 nm (red symbols) and 2.8 nm (blue symbols) - mainframe; arm diameter D, for L = 3.5 nm (black symbols) - inset.

Our results suggest that the non-zero amplitude of the electron-hole wave function overlap found in short- and thin-armed TPs, despite the presence of a charge-separating band alignment at the CdTe/CdSe interface, is due to a lack of available volume for the electron to 'expand' into. Indeed, the position of the electron charge density moves away from the core region as soon as the arms' volume increases (Fig. 2.4). In CdTe/CdSe core/arms TPs, the increase in L also leads to a nearly vanishing $\Delta E_{cb_{1-4}}$, which decreases from about 17 meV (for $L = 3.5$ nm) to 0.1 meV (for $L = 14$ nm), in structures with $D = 2.1$ nm, ensuring the desired four-fold degeneracy of the CBM. Importantly, as it is the case with uniform-composition TPs [41], within this length window the position of the CBM only varies by a few tens of meV (see Fig. 2.2), and hence so does the band gap (as the VBM is nearly constant). This has the double benefit of increasing the absorption cross section with volume, whilst maintaining absorption in the visible. Furthermore, from Fig. 2.2 we can also see that, in this size range, crucially the CBM remains between the redox potentials for H_2O and CO_2 reduction to CH_4 (top brown dashed lines), ensuring excellent selectivity for the latter reaction.
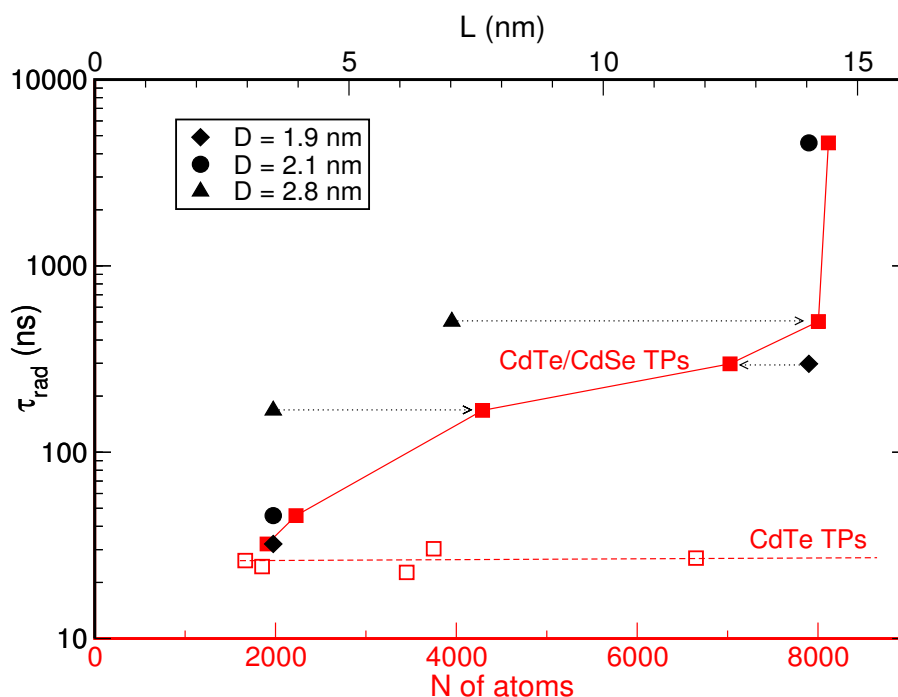
Figure 2.7: Radiative recombination lifetimes, calculated at room temperature as a function of volume indicated by the total number of atoms in the TP (red symbols, bottom x axis) and as a function of arm length (black symbols, upper x axis) in TPs with $D = 1.9$ nm (red squares and black diamonds), 2.1 nm (red squares and black circles) and 2.8 nm (red squares and black triangles). The lifetimes calculated in homogeneous CdTe TPs are also shown (empty red squares) for comparison. The dotted arrows connect symbols relative to the same structure.

We also find that a simple increase in the arm diameter from 1.9 nm to 2.8 nm, yields an

over five-fold increase in radiative lifetime, even for a very short arm ($L = 3.5$ nm). Most remarkably, however, in structures with $D = 2.1$ nm, the calculated room temperature radiative lifetime increases by over two orders of magnitude, from 45 ns to 4.6 μs, when increasing L by a factor of 4, from 3.5 nm to 14 nm (filled black circles in Fig. 2.7).

This is in striking contrast with the behaviour of conventional CdTe TPs, where, for similar increases in either D or L, we find no appreciable variation in the calculated radiative recombination time, which remains at around 25 ns (red empty squares in Fig. 2.7), i.e., comparable to that of spherical nanocrystals, owing to the fact that both CBM and VBM are localized in the core (so that there is little change in their overlap with increasing total volume). Even in CdSe/CdS TPs with an aspect ratio of L/D as large as 10 the observed radiative lifetime is only a factor of 3 longer than in spherical CdSe nanocrystals with similar diameters [86]. As a comparison, the measured recombination time in TiO_2 nanoparticles, CO_2's reduction catalysts of choice, is sub-nanosecond [98].

The radiative recombination lifetimes we predict for CdTe/CdSe core/arms TPs with more than 8000 atoms are therefore longer than (or comparable to) the typical redox reaction times ($> 10^{-8}$ s) [61] - which are usually too slow to compete with the radiative lifetimes ($\sim 10^{-9}$ s) exhibited by common semiconductor nanocrystals or conventional same-composition TPs. This should allow the charge carriers sufficient time to reach the surface (which is conveniently close, given the small arm diameter, and provides a huge contact area for CO_2 adsorption (3), due to the considerable arm length), and react with CO_2 and H_2O before recombining. Furthermore, the long arms of these nanostructures present many facets with different orientations, providing large amounts of undercoordinated surface metal atoms, which have been shown [99] to be extremely efficient in transferring electrons to adsorbed reactants, resulting in high catalytic activity and selectivity. Such coordinatively unsaturated Cd atoms also serve as trapping sites for efficient adsorption of CO_2 molecules [100], leading to a significant improvement in their photocatalytic reduction [101].

Long radiative lifetimes are of limited utility in the presence of fast non-radiative recombination pathways. In colloidal nanocrystals, the most efficient of such processes is Auger recombination (AR), where the recombination of an electron-hole pair in the presence of excess electrons and/or holes is accompanied by a (non-radiative) energy transfer to one of the 'spectator' particles, which is excited to a higher energy state (see Fig. 2.8). Typical AR lifetimes
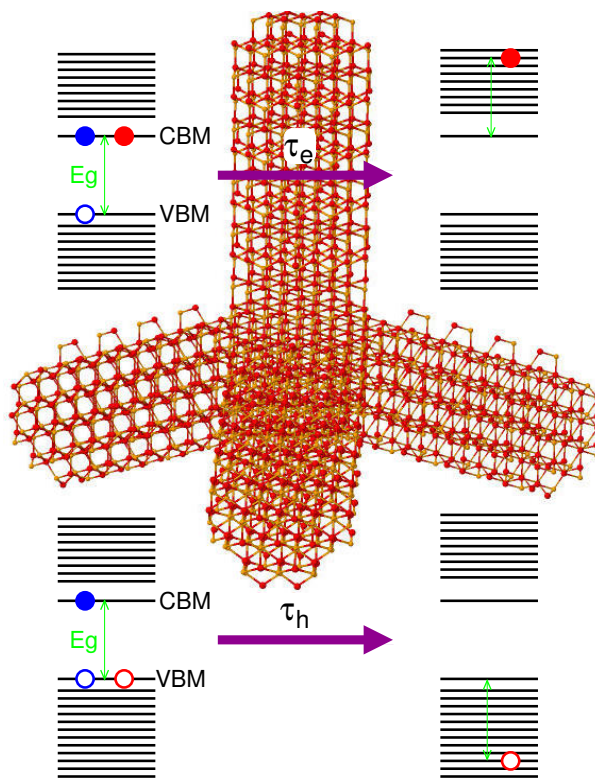
Figure 2.8: Schematics of the Auger Recombination processes in the presence of an excess
electron (top panels) or an excess hole (bottom panels)[55].

in CdSe spherical dots with diameters of 2.4 nm are of the order of a few picoseconds [102],
and decrease with decreasing dot size. We find that in CdTe/CdSe core/arms TPs the weak
electron-hole wave function overlap also leads to strong AR suppression. Our calculated AR
times are one to over two orders of magnitude longer than in spherical nanostructures with
similar diameters, and increase with arm length, ranging (in TPs with $D = 2.1$ nm), from about
40 ps (for $L = 3.5$ nm) to about 800 ps (for $L = 14$ nm).

We want to stress that this twenty-fold increase with arm length is not due to a simple volume
scaling, as the increase in AR times observed in spherical CdSe nanocrystals for a similar vol-
ume increase is only of a factor of less than 5 [102]. Interestingly the AR lifetime associated
with excess electrons (τ_e) is of the order of ten microseconds, whereas that associated with ex-
cess holes (τ_h) is shorter than 1 ns and dominates the total calculated AR time, in the case of
a CdTe/CdSe TP with $L = 14$ nm (for $L = 3.5$ instead, the two contributions are more sim-
ilar to each other - of the order of 200 ps for τ_e and 40 ps for τ_h). The origin of such a large
disparity is the different contribution from arm and core states to the calculation of the two
lifetimes: τ_e involves three arm-delocalised electron and one core-localised hole wave function
(the initial state is a hole in the VBM and two electrons in the CBM, the final state is an excited

electron), which have little overlap with each other, whereas in the calculation of τ_h three out
of four wave functions are relative to core-localised holes (the initial state is an electron in the
CBM and two holes in the VBM, the final state is an excited hole), and therefore exhibit a much
larger overlap. In contrast, in CdTe TPs, where both CBM and VBM can access the core region,
and the charge densities of electrons and holes are distributed more uniformly throughout the
nanostructure, we calculate $\tau_e \approx \tau_h$. These results strongly suggest that, owing to their specific
band alignment at the heterojunction and the availability of a large volume for the CB wave
functions to spread, CdTe/CdSe TPs with long arms favour the accumulation of electrons.

There has been some debate regarding which geometrical feature, arm length [103] or TP vol-
ume [104], most affects the TP properties. Our results clearly show that both the excitonic
structure and the optical properties are determined by the TP volume, more than by the arm
length alone. To show this, we will focus on four of our structures: TP1, TP2, TP3, and TP4
(see above). If arm length were the critical structural feature determining the TP properties,
we should find similar results for TP1 and TP2 (if it were the diameter, our results should be
similar for TP2 and TP4, as they would if the volume were irrelevant). If, however, TP volume
were more important, then TP2 and TP3 should exhibit a similar behaviour.

Both excitonic structure and optical properties in semiconductor nanostructures are deter-
mined by the electron-hole coupling (quantified by their wave function overlap). A quanti-
tative measure of this overlap is provided by the direct Coulomb matrix elements (J_{vc}) and
by the dipole matrix elements (M_{vc}), calculated between valence (v) and conduction (c) states.
The former represent the electron-hole attraction energy that binds the exciton, and is the main
component determining the excitonic red shift, compared to the single-particle picture [105],
while the latter determines the nanostructure's optical properties, among which the radiative
recombination lifetimes. We calculated that in TP2 J_{vc} is very small (18 meV) and has the same
value for $v =$ VBM, and $c =$ CBM, CBM+1, CBM+2, and CBM+3, (as a comparison, in a spher-
ical CdSe nanocrystal with the same diameter of 2.1 nm we calculate $J_{VBM,CBM} \sim 400$ meV),
whereas in TP1 and TP4 $J_{VBM,CBM}$ (= 39 meV and 105 meV, respectively) is different from
$J_{VBM,CBM+j}$ (= 26 meV, and 82 meV, respectively, for $j = 1, 2, 3$), evidencing (A) a larger over-
all electron-hole coupling in TP1 and TP4 than in TP2, and (B) a different degree of overlap
between the VBM and the lowermost four CB states in those structures. In contrast, in TP3
$J_{VBM,CBM}$ and $J_{VBM,CBM+j}$ are very similar, their difference being of only about 3 meV.

These features have a direct effect on the TPs' excitonic structure: due to the four-fold degeneracy of its CBM, and to the constant value of the overlap between VBM and CBM+j (for $j = 0, 1, 2, 3$), TP2 exhibits an almost perfect 32-fold degenerate ground state exciton (obtained from the combination of four CBM and two VBM states and including the spin degeneracy), with the whole fine structure contained within only 6 meV (i.e., the energetic separation between excitons 1 and 32 is only 6 meV. As a comparison, in a spherical CdSe nanocrystal with the same diameter of 2.1 nm we calculate such a separation to be over 600 meV). Despite a similar and nearly perfect four-fold degeneracy of the CBM (the difference between the energetic position of CBM and CBM+3 is here only 1.5 meV), in TP1 the lowermost 32 excitonic states are instead spread over 39 meV, compared with only 19 meV in TP3, and 80 meV in TP4, reflecting the behaviour found in J$_{vc}$ in the three structures. We conclude that arm length is important (see TP2 vs TP4), but volume is even more so (see TP1 vs TP2).

Turning now our attention to the optical properties, we, again, find that the volume, not the arm length, determines the radiative recombination lifetimes in these hetero-nanostructures (Fig. 2.7). Indeed, we calculate the longest lifetime (4574 ns) in TP2 (8115 atoms), followed by TP3 (503 ns, 8005 atoms), TP1 (298 ns, 7027 atoms), and TP4 (45.7 ns, 2227 atoms), confirming the strongest electron-hole couplings to occur in TP4 (which has the smallest volume and arm length) and TP1 (which has the same arm length as TP2, but a smaller volume), compared to the other two structures.

2.3 Conclusions

In conclusion, our electronic structure calculations have shown that CdTe/CdSe core/arms TPs with arms' diameters of about 2.1 nm ($1.9 \leq D < 2.8$) and arms' lengths ≥ 14 nm can be extremely efficient light harvesters (i) with large absorption cross sections in the visible part of the spectrum, exhibit charge separation (ii) where electrons and holes are localised in different spatial regions of the hetero-nanostructure (5), leading to long carriers' lifetimes (compared to both homogeneous TPs and typical redox reaction times), provide short charge migration pathways from the bulk phase to the surface, and a very large surface area rich in coordinatively unsaturated metal atoms promoting reactant adsorption (3) and reaction (iii), which can be increased independently from the band gap (4), exhibit high selectivity for CO_2 reduction vs the competing H_2O reduction (1), and, finally, are capable to provide eight isoenergetic elec-

trons at one time (2). They therefore present themselves as ideal catalysts for CO_2 reduction to CH_4, exhibiting potential for unprecedented selectivity and for unparalleled efficiency. We stress the word *potential* here, however, as, despite all of the TPs' remarkable thermodynamical and dynamical properties listed above, deriving from their electronic structure, optical properties and charge dynamics, it is important to highlight that adsorption/desorption properties of reactants and intermediates also play a fundamental role in determining the product's selectivity and yield. The modelling of such properties is beyond the capability of our approach and the scope of the present work. Nevertheless, the available literature suggests the presence of coordinatively unsaturated metal atoms (such as the Cd atoms abundant on the TP's surface) to facilitate reactant adsorption, leading to high reduction rates. Furthermore, the high selectivity for CH_4 production achieved by large CdSe NCs, and the very low overpotentials and activation energies measured in these systems, provide further support to our claims. We therefore hope these results will stimulate further research, such as detailed catalytic analysis and experimental implementation of TP-based photocatalytic cells, aimed at verifying the effective selectivity and efficiency of these versatile nanostructures for CO_2 reduction to CH_4.

Chapter 3

Decoupling Radiative and Auger Processes in Semiconductor Nanocrystals by Shape Engineering

3.1 Introduction

Semiconductor nanocrystals (NCs) have attracted widespread attention as light-emitting materials and have been utilized in fluorescent bio-labelling [106], LEDs [107] and lasers [108], thanks to their peculiar size-dependent optical and electronic properties [63], [109], [110]. Indeed, their emission can span the whole visible spectrum [111], [112] achieving nearly unitary photoluminescence quantum yields [113]. Ironically, the same properties that make these systems attractive for lighting applications are also responsible for the efficiency of the non-radiative recombination mechanisms that plague them, which is commonly attributed to the suppression of momentum conservation and the enhancement of Coulomb interaction occurring in strongly confined systems [114]. In particular, in the presence of high doping concentrations or high excitation powers, Auger recombination (AR) that has been described in last chapter effectively competes with radiative recombination (RR), leading, among other effects, to fluorescence intermittency [115], and limiting optical gain [108]. Another related process, Auger cooling (AC), is responsible for the extremely efficient electron thermalization observed in NCs, which occurs via an electron-hole scattering mechanism, where a hot electron relaxes to the ground state by transferring its excess energy to a hole in its ground state and exciting

61

it to a deeper state, proving detrimental for applications in intraband infrared photodetection and hot-electron solar cells [116]–[118].

Therefore, devising effective strategies to overcome such extremely efficient non-radiative processes, enabling the creation of population inversion and the attainment of the theoretically achievable optical gain in nanocrystals, is one of the priorities that has occupied the NC synthesis community for long time.

As the Auger rates depend on the coupling integral, that contains both initial and final states, i.e., the wave functions of both electron and hole, the approach most commonly used is based on the reduction of their overlap in real space.

This can be achieved through structure modification: (i) elongation - the synthesis of nanorods with large aspect ratios of length over radius has been shown to promote spatial separation of electron and hole wave functions, leading to a reduction in AR rates [119]; (ii) asymmetrical heterostructuring - dot-in-a-rod (dot@rod) structures, where the the spherical quantum dot is embedded in a rod-shaped shell made of a different material and is generally located close to one of the rod's extremities, achieve a localization of the hole in the core whereas the electron is delocalized throughout the rod, leading to a reduction in the AR rates [120]; (iii) symmetrical heterostructuring - the growth of a shell of a different semiconductor material, with a specific electronic structure, around the spherical nanocrystal core, can lead to a type II (or quasi type II) band alignment at the heterointerface, resulting in complete (or partial) spatial segregation of electron and hole, each confined to a different material [121], [122], markedly suppressing Auger processes [123], [124]. However, the synthesis methods for some of these structures are complex (as it is the case for successive ion layer adsorption and reaction - SILAR), inevitably increasing both growth time and energy consumption [122], [125] and consequently the processing cost.

In contrast to structure and size engineering, the modification of the conduction band states' wave function composition in reciprocal space, which leads to a decreased overlap with the holes' wave function *in k-space*, is another approach recently proposed to suppress Auger processes [126]. Unfortunately all of these methods, by reducing el-h overlap, also lead to an undesired suppression of RR [127], making these systems well suited for solar energy harvesting applications (such as PV or photocatalysis), but not for applications as light emitters (LEDs and lasers). The close link existing between AR and RR is exemplified by the peculiar scaling

$\tau_{AR} \propto V\tau_{RR}$ (where V is the NC volume), observed in CdTe/CdSe core/shell NCs [123].

Devising strategies to suppress Auger processes, while retaining, at the same time, the high radiative rates and PL quantum yields that characterise these systems, is therefore crucial for the effective exploitation of their full potential as emissive media. Here we show that this is indeed possible and can be achieved by structure manipulation, and, in particular, by combining elongation (i) with symmetrical growth (iii), in branched homostructures, also known as tetrapods (TPs).

Thanks to their easy fabrication and processability, and their versatile electronic and optical properties, tetrapod-shaped nanocrystals have recently attracted large interest [41], [42], [83]. In this family, CdTe TPs are the simplest structures in terms of synthesis and size control[41]. Their electronic structure, charge dynamics [128], optical [129], mechanical and electrical [130] properties have been investigated both experimentally and theoretically however, to the best of our knowledge, Auger processes have not been explicitly considered nor systematically studied.

In this chapter we present a theoretical characterisation of CdTe TPs covering a wide range of aspect ratios $0.8 \leq \rho \leq 6.7$ (including experimentally relevant ones[84]–[86]), of arm length (L) over arm diameter (D), for 1.75 nm $\leq L \leq 14$ nm and 1.75 nm$\leq D \leq 3.5$ nm, containing from about 1000 to over 6600 atoms. In the previous Chapter we used the same theoretical framework to design heterostructured, core/arms TPs for selective CO_2 reduction to CH_4. In that Chapter the main aim were to achieve (i) charge separation between core and arms (to ensure that the photogenerated electron and hole did not recombine before reaching the surface and reacting with CO_2 and H_2O), and (ii) an accurate conduction band minimum positioning between the reduction potentials of CO_2 to CH_4, and of H_2O to H_2 (to guarantee good selectivity). This was achieved using TPs with a CdTe core and CdSe arms, which resulted, *inter alia*, in orders of magnitude decrease in the RR rate with increasing arm length, as a consequence of the different localisation of the ground state electron and hole (the latter being localised in the core and the former in the arms), caused by the type II band alignment at the CdTe/CdSe interface.

The question we will address here is, instead, whether AC and AR can be suppressed efficiently *without* affecting RR, therefore achieving a complete decoupling between radiative and Auger processes.

3.2 Results and Discussion

The variation of the band edges with L (for a fixed $D = 2.1$ nm), D_{arm} (assuming the same core diameter and $L = 3.5$ nm), and D_{core} (for a fixed arm diameter of 2.1 nm and length of 3.5 nm) is presented in Fig. 3.1. We find that both CBM and VBM positions are nearly unchanged (they shift, respectively, by 10 meV and 26 meV), for an almost one order of magnitude increase in L, from 1.75 nm to 14 nm (Fig. 3.1, mainframe), whereas they shift by hundreds of meV (305 meV and 144 meV, respectively), for a much smaller increase (from ~ 2 nm to 3.5 nm) in the TP's arm diameter D (Fig. 3.1 inset, red symbols).
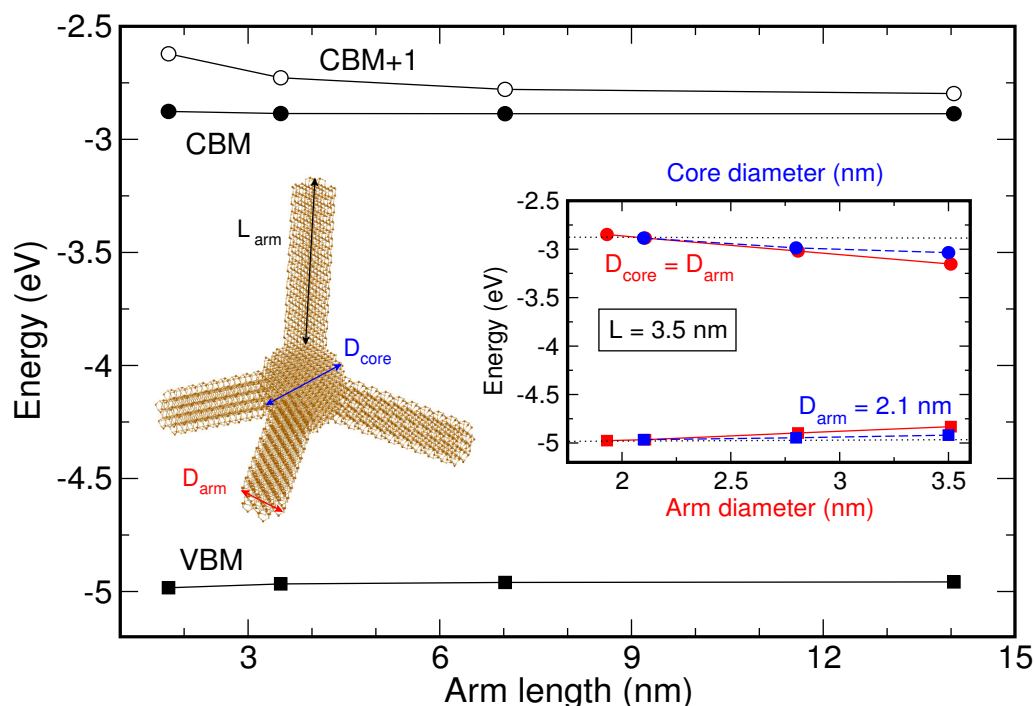

Figure 3.1: CdTe TP valence (squares) and conduction (circles) band edge energies, calculated, with respect to vacuum, as a function of: (mainframe) arm length L, for $D = 2.1$ nm; (inset) arm diameter D_{arm}, assuming the core diameter $D_{core} = D_{arm}$ (red symbols, bottom x axis) and core diameter D_{core} [1](for $D_{arm} = 2.1$ nm, blue symbols, upper x axis) for $L = 3.5$ nm. The solid lines are a guide to the eye. The dotted lines in the inset mark the position of CBM and VBM for $D = 2.1$ nm as a function of L from the mainframe, for a direct comparison of the dependences from the different geometrical parameters. This comparison highlights that the band edges position is most sensitive to the arm diameter D_{arm}, followed by core diameter D_{core} and is nearly independent on the arm length L.

A similar dependence on D and L was observed in elongated NCs (i.e., quantum rods, QRs), where electronic structure and optical properties were found to be dictated primarily by the arm's diameter [131]. Unlike in QRs, however, here this property derives from the peculiar

---

[1]Although for $D_{core>D_{arm}}$ the core/arm junction may appear spherical, in reality it is a junction between two flat atomic planes, as there are no curved surfaces in an atomistic description.
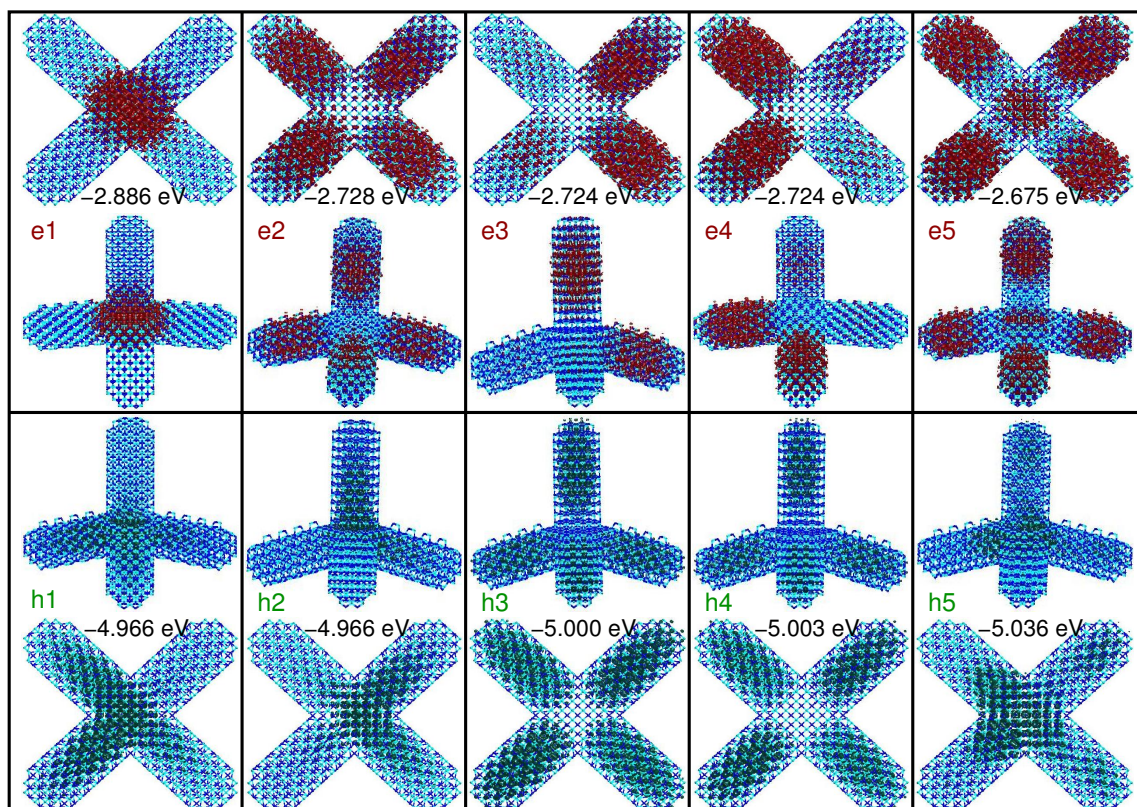
Figure 3.2: Charge densities for the uppermost 5 valence (green, bottom panels) and lowermost
5 conduction (red, top panels) band states, calculated for CdTe TPs with $D = 2.1$ nm and
$L = 3.5$ nm (two different views of the TP are presented). Also reported are the corresponding
energies, relative to vacuum. Blue and cyan dots represent Cd and Te atoms.

localisation of the band edges' wave function occurring in TPs made of one material: due to
the band alignment at the interface between zinc-blende core and wurtzite arms[41], [81], the
CBM is localised in the TP's core[82] (whose size depends on D but not on L).

This is clearly shown in Fig. 3.2 and Fig. 3.3, where we present the calculated electron density
distribution for conduction and valence states in TPs with $D = 2.1$ nm and, respectively, $L =$
3.5 nm and $L = 14$ nm. We see that in both nanostructures the CBM (e_1) is highly localised in
the core, whereas the doubly degenerate VBM ($h_{1,2}$) also extends to the arms, as was found to
be the case in CdSe TPs [82]. Deeper VB states' wave functions present, alternately, a node (i.e.,
zero amplitude) or a peak in the core region. The excited CB states' wave functions exhibit the
same behaviour in short-armed TPs (Fig. 3.2), but not in long-armed TPs (Fig. 3.3), where they
always have a node in the core. Their symmetry is σ-like, as in a QR [132], with zero (e_2-e_5),
one (e_6-e_9), two (e_{10}), ..., n nodes along each arm.

As a consequence, the band edges position, hence the TP's band gap, is most sensitive to the
arm diameter D_{arm} (Fig. 3.1 inset, red symbols), and the core diameter D_{core} (Fig. 3.1 inset, blue
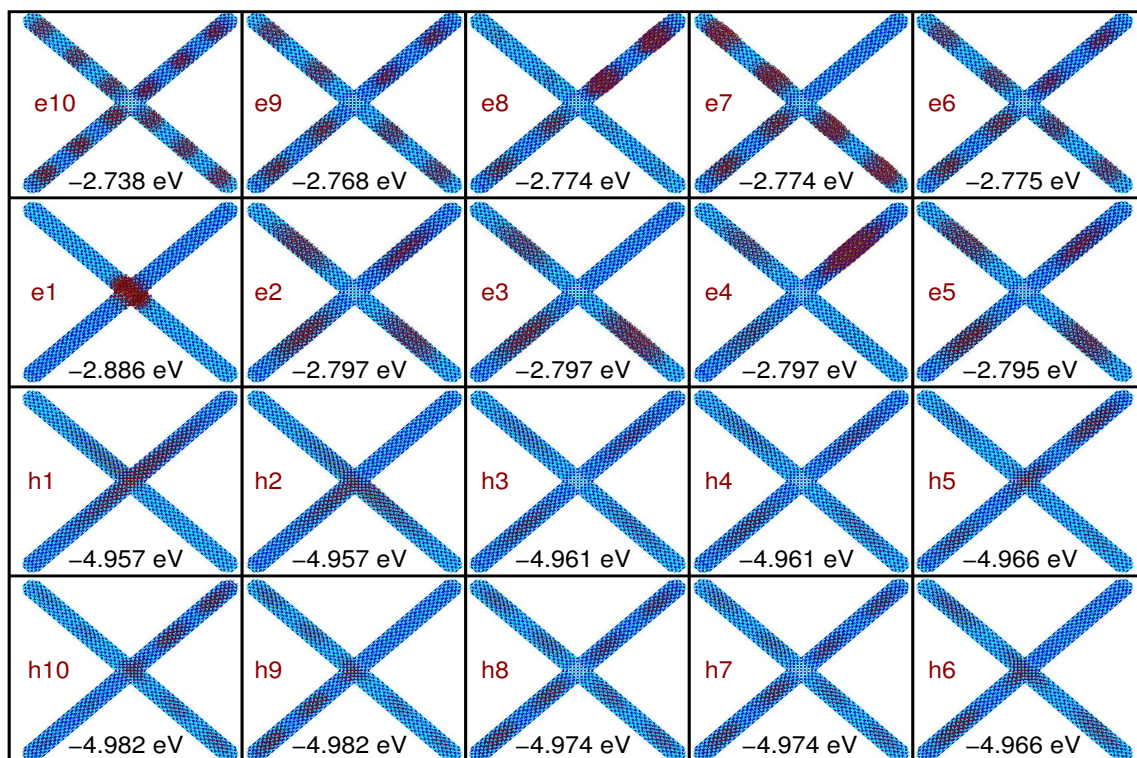
Figure 3.3: Charge densities (red) for the uppermost 10 valence (bottom 2 panels) and lowermost 10 conduction (top 2 panels) band states, with $D = 2.1$ nm and $L = 14$ nm. Also reported are the corresponding energies, relative to vacuum. Blue and cyan dots represent Cd and Te atoms.

symbols), and is nearly independent of the arm length L (Fig. 3.1 mainframe), in agreement with experimental observation [129].

Figure 3.4: Absorption spectra calculated for TPs with $D = 2.1$ nm and different values of the arm length L.

The latter property is reflected in the optical absorption spectra calculated for TPs with $D = 2.1$ nm and 1.75 nm $\leq L \leq 14$ nm (Fig. 3.4), where the position of the absorpt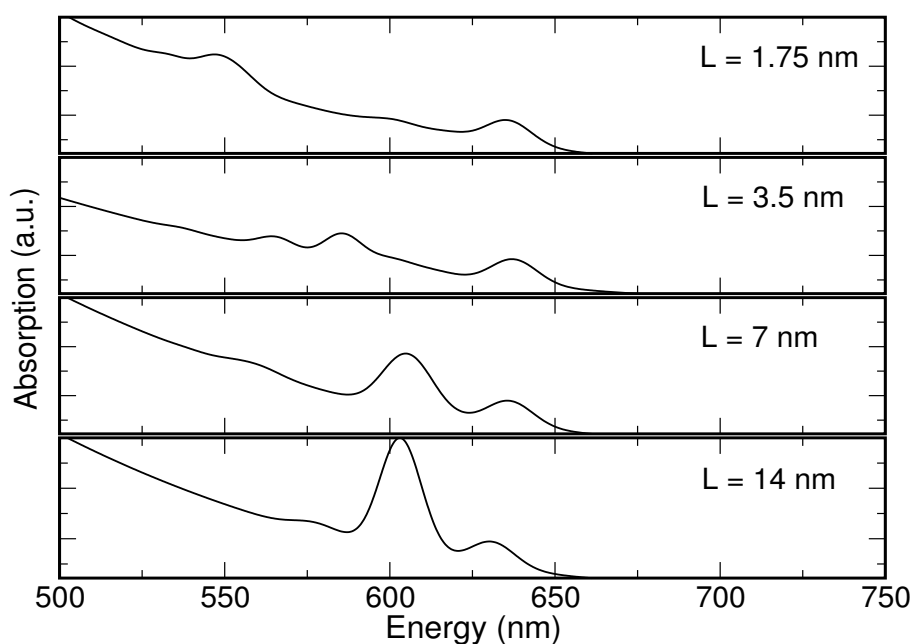ion edge, corresponding to the transition between the band edges, is independent of the arm length, as observed experimentally [41], [81].

Similarly, we find that the radiative lifetime is also independent of L, as shown in Fig. 3.5 (mainframe), but sensitive to D (Fig. 3.5 inset), where it increases by a factor of 4 for an increase in diameter from about 2 nm to 3.5 nm. In summary, our results show that the electronic structure and optical properties *associated to the band edges* are insensitive to the TP's arm length, for a wide range of aspect ratios.
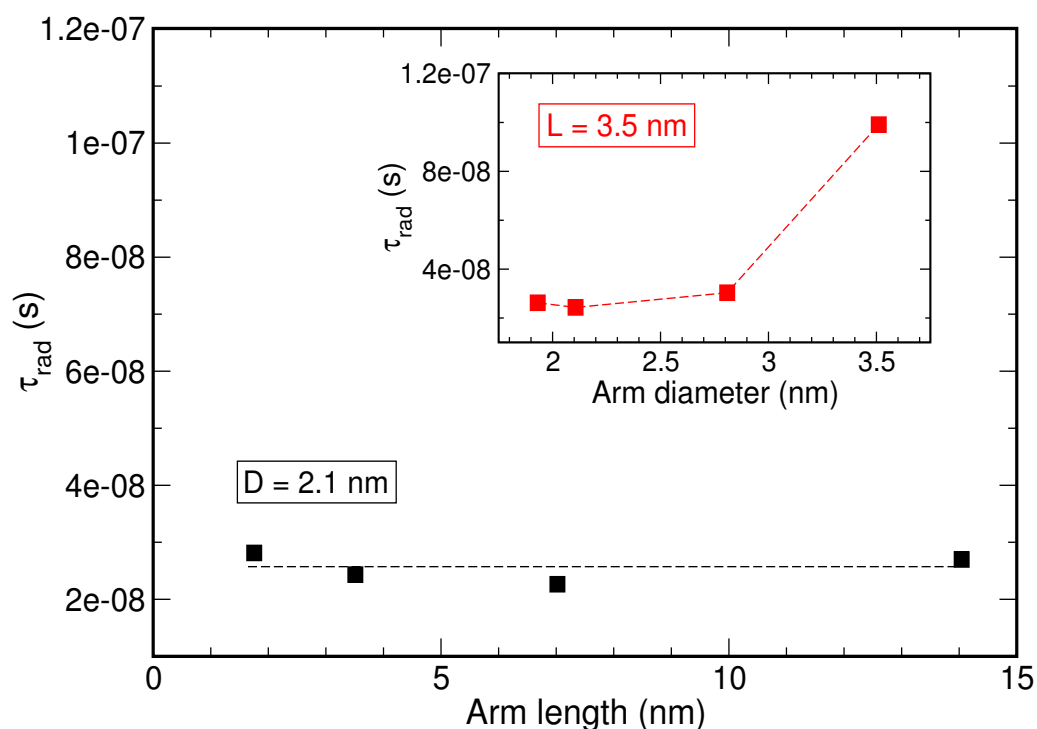
Figure 3.5: RR lifetimes calculated, at room temperature, as a function of arm diameter (inset, red symbols) for $L = 3.5$ nm, and as a function of arm length (mainframe, black symbols) for $D = 2.1$ nm. The lines are a guide to the eye.

The question we want to address now is whether this insensitivity also applies to properties connected to excited states, and mechanisms relevant for light-emission applications, such as the electron intra-band relaxation or the biexciton recombination, which, in these systems, are mediated by Auger processes.

The AC lifetimes τ_{AC} calculated for TPs with $D = 2.1$ nm and $L = 3.5$, 7 and 14 nm are presented in Fig. 3.6, together with that of a spherical nanocrystal with a similar absorption edge

($R = 1.7$ nm) as a reference. The lifetime is shown here as a function of ΔE (the variation in the electron transition energy around the energy calculated for the ideal tetrapod - corresponding to $\Delta E = 0$), to account for possible energy dephasing effects due to ensemble effects (size distribution or shape anisotropy) and the influence of electric fields or charges in the environment. τ_{AC} increases by ~ 2 orders of magnitude for an increase in L of a factor of 4, from 3.5 to 14 nm, and by about 3 orders of magnitude with respect to a spherical NC. In contrast with the behaviour observed in spherical NCs, where τ_{AC} was found to depend linearly on the NC radius [102], we find that, in TPs, the best fit to a power law yields a cubic dependence on L ($\tau_{AC} = A_0 L^3$, with $A_0 = 3.4 \times 10^{-3}$, black dashed line in Fig. 3.7a), whereas the best overall fit yields $\tau_{AC} = B_0 \exp(0.4L)$ ($B_0 = 4.6 \times 10^{-2}$, green dashed line in Fig. 3.7a). Similar dependences are also found on the volume (expressed as the total number of atoms, N_a), [2] i.e., $\tau_{AC} = C_0 N_a^{3.3}$ and $\tau_{AC} = D_0 \exp(N_a/1000)$ (with $C_0 = 1.8 \times 10^{-12}$ and $D_0 = 2.7 \times 10^{-2}$, black and green dashed lines in Fig. 3.7b), showing that, despite following a L^3 scaling, τ_{AC} does not depend linearly on the TP volume.
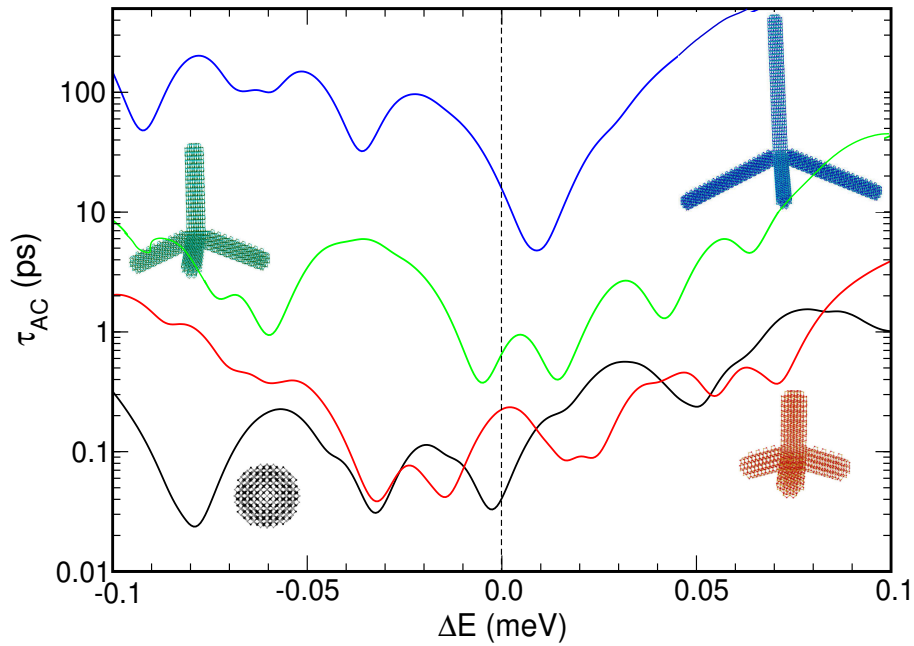
Figure 3.6: AC relaxation times in TPs with $D = 2.1$ nm and L=3.5 (red curve), 7 nm (green curve), and 14 nm (blue curve), as a function of ΔE (see main text). The black curve indicates the AC relaxation time calculated for a CdTe quantum dot with $R = 1.7$ nm for reference.

---

[2] We employ atom numbers to unequivocally express the volume, as opposed to using conventional units of nm^3, as volume estimates that use the latter are based on an assumed perfect geometrical (i.e., usually cylindrical) shape for the arms, that is never realised at the atomistic level.

Figure 3.7: AC relaxation times in CdTe TPs with $D = 2.1$ nm, calculated as a function of L (a) and as a function of the volume (b), expressed as the total number of atoms in the TP, N_a. Black and green dashed lines indicate fits to power (ax^p) and exponential (be^{cx}) functions, respectively. We find $A_0 = 3.4 \times 10^{-3}$, $B_0 = 4.6 \times 10^{-2}$, $C_0 = 1.8 \times 10^{-12}$, and $D_0 = 2.7 \times 10^{-2}$ give the best fits. The red symbol represents the AC lifetime calculated for a CdTe quantum dot with $R = 1.7$ nm for reference.
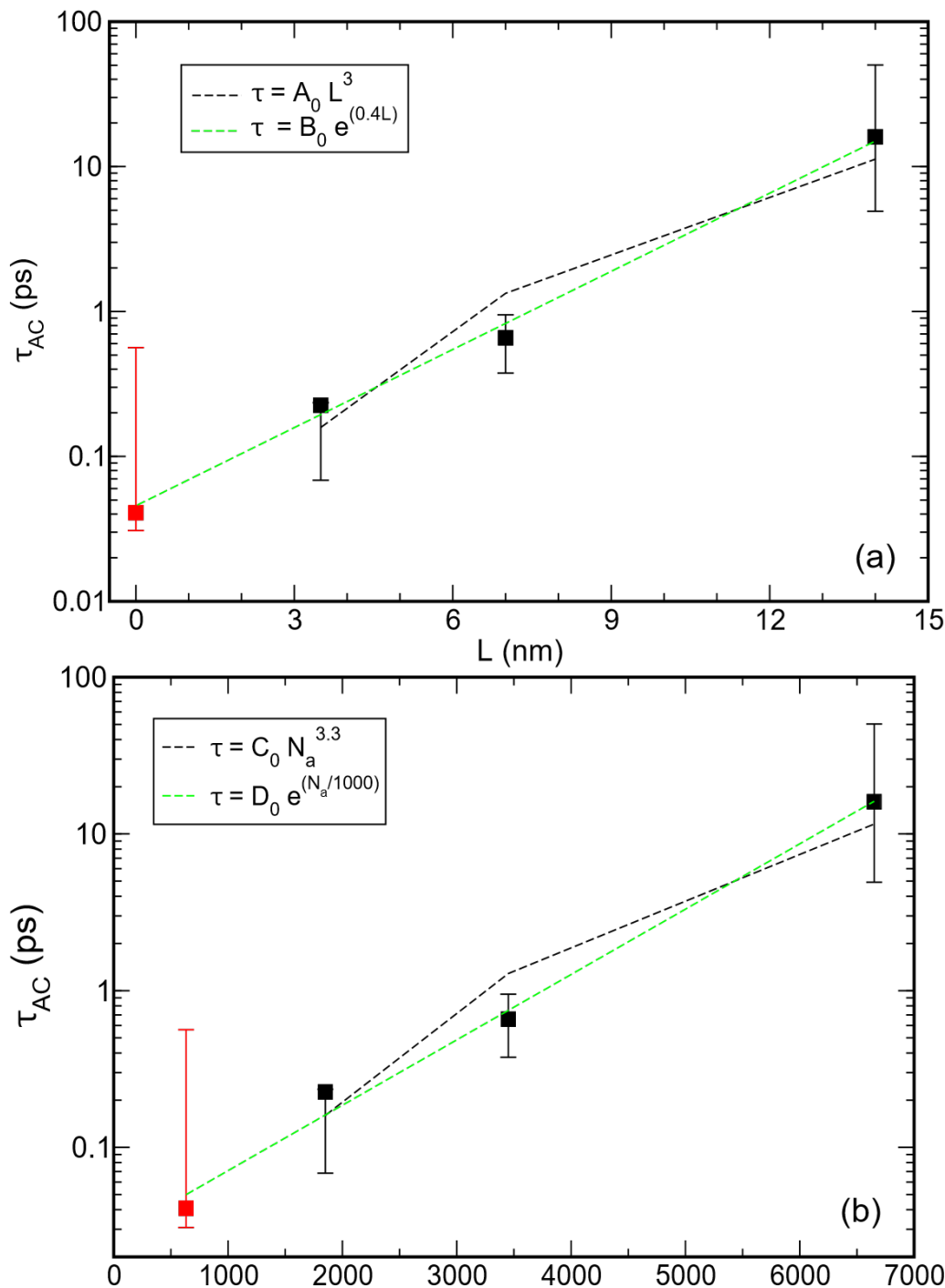
Figure 3.8: AR lifetimes in CdTe TPs with $D = 2.1$ nm, calculated as a function of L (a) and as a function of the volume (b), expressed as the total number of atoms in the TPs, N_a. Black and green dashed lines indicate fits to power (ax^p) and exponential (be^{cx}) functions, respectively. We find $A_1 = 106.6$, $B_0 = 28.3 \times 10^{-2}$, $C_1 = 3.2 \times 10^{-4}$, $t_0 = -97.7$, and $D_1 = 7 \times 10^{-2}$ give the best fits. The red symbol represents the AC lifetime calculated for a CdTe quantum dot with $R = 1.7$ nm for reference.
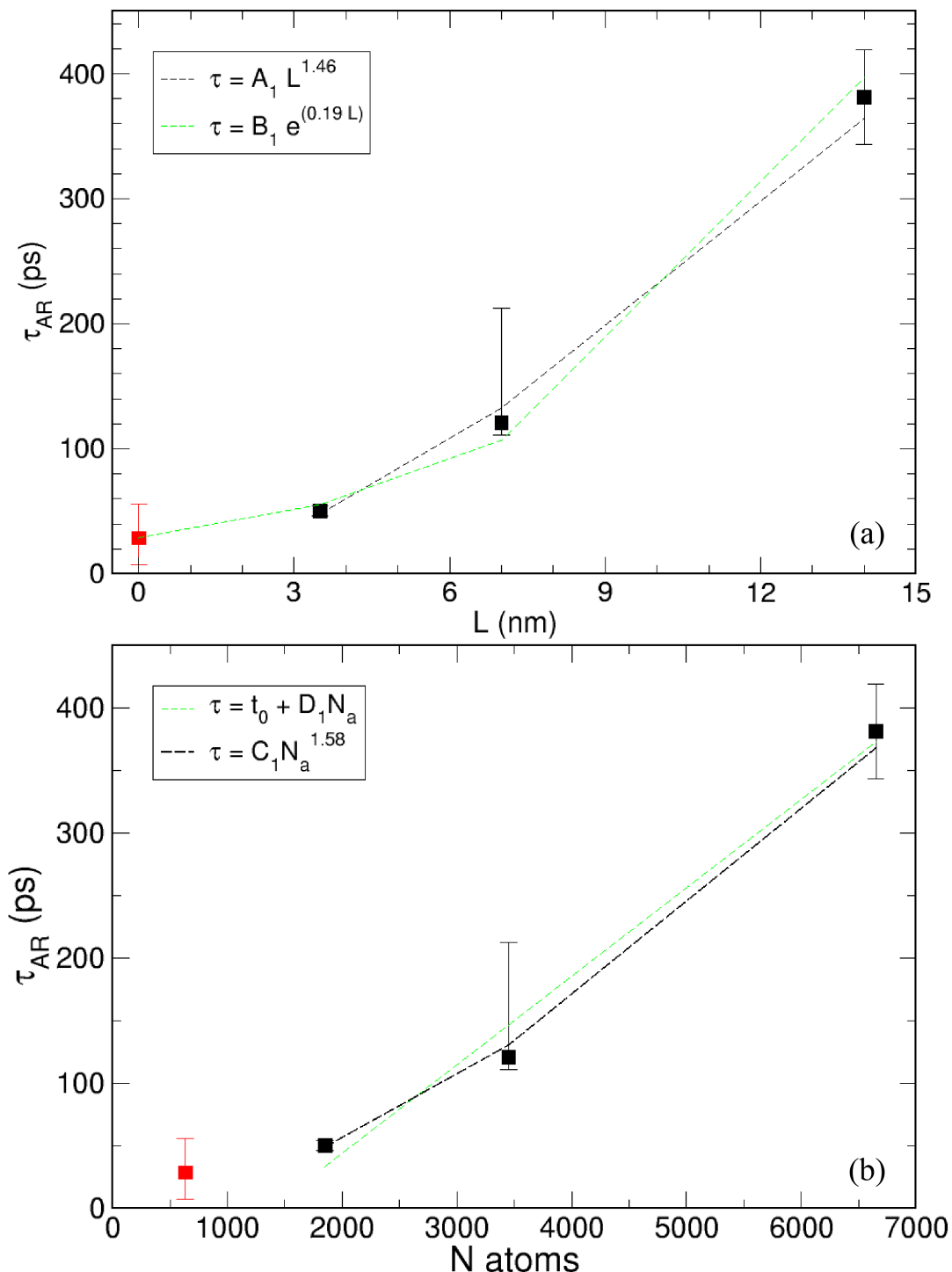
An approximately linear dependence on the volume has been observed for the AR lifetimes

in spherical NCs made of CdSe [133], [134], PbSe [135], Ge [136], HgTe [137], InAs [136], and

$FAPbBr_3$ [138], [139]. Interestingly, however, CdTe NCs have been reported to follow a V^{α} scaling[140] with α = 1.5 - 2.3, depending on the surface capping. For our calculated AR lifetimes, shown in Fig. 3.8, we find $\tau_{AR} = C_1 N_a^{1.6}$ (with $C_1 = 3.2 \times 10^{-4}$) to provide the best fit (see blue dashed line Fig. 3.8b), in agreement with the dependence on volume observed in spherical CdTe NCs. Furthermore the AR lifetime we calculate for a CdTe NC with $D = 3.4$ nm (red square in Fig. 3.8) is in excellent agreement with the values experimentally measured for NCs with similar sizes [140] (magenta circle in Fig. 3.9). In terms of dependence on L, we find a nearly one order of magnitude increase in the AR lifetimes, when L increases from 3.5 nm to 14 nm (while, at the same time, both band gap (Fig. 3.4) and radiative lifetime (Fig. 3.5) remain constant), for an overall $\tau_{AR} \propto L^{1.5}$ scaling (black dashed line in Fig. 3.8a). As it was the case for τ_{AC}, we find that an exponential function ($\tau_{AR} = B_1 \exp(0.2L)$ with $B_1 = 28.3$, green dashed line in Fig. 3.8a) fits the data well too.
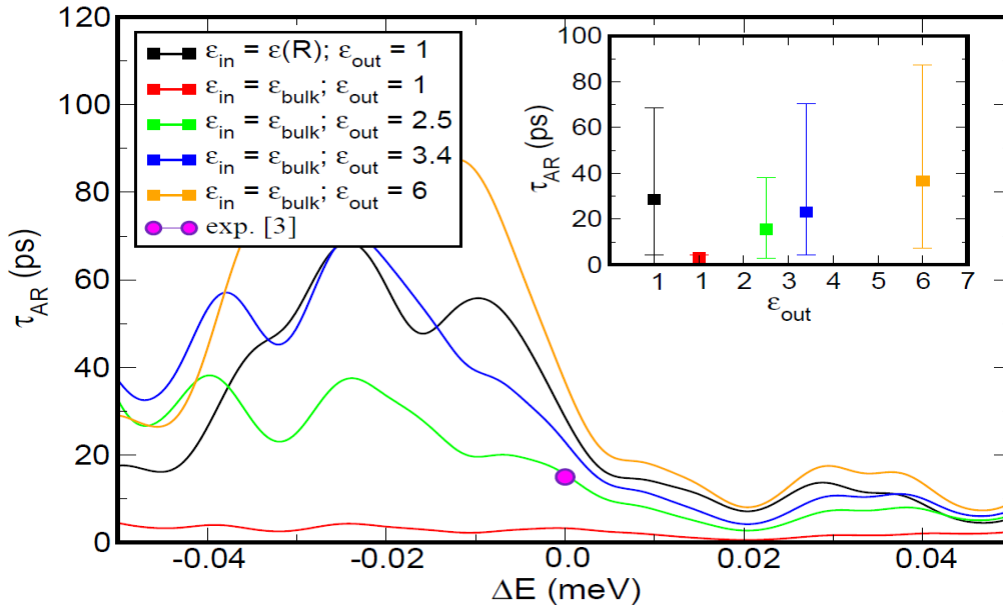
Figure 3.9: Comparison of the AR lifetimes calculated, as a function of the energy variation around the calculated single-particle gap (corresponding to $\Delta E = 0$), in a CdTe spherical nanocrystal with $r = 1.7$ nm, using the 'regional screening' approach of Wang *et al.* [55] (coloured lines and symbols), and the 'size-dependent screening' approach of Franceschetti *et al.* [105] (black line and symbols). Experimental data relative to a CdTe spherical dot with $D = 3.4$ nm (magenta circle) [140] are also included for comparison. In the 'regional screening' approach the dielectric constant inside the dot (ε_{in}) is assumed equal to the bulk dielectric constant. The variation to the external dielectric constant ε_{out} occurs via a smoothly decaying sine-like function [55]. The 'size-dependent screening' approach assumes ε_{in} to be size- and position- dependent [105] and $\varepsilon_{out} = 1$.

These results clearly show a complete decoupling between band edge optical properties, that

determine band gap radiative lifetimes and PL quantum yields, and excited-state relaxation mechanisms that characterise the efficiency of the Auger processes. The origin of this separation lies in the spatial localisation of the electronic states involved in the two groups of transitions: as discussed above, CBM and VBM are localised primarily in the TP's core [82] (whose size is independent of L), whereas the excited states are mostly localised in the TP's arms, with a charge density that decreases with increasing arm length. This guarantees that the wave function overlap is large between the band edges, for any value of L, but becomes increasingly weak between band edge states and excited states, when L increases. A link between AR suppression and a reduction in the effective carrier density, which is inversely proportional to the NC volume, was indeed suggested by Htoon *et al.* [141], to explain the increase in AR lifetimes they observed in QRs, compared to spherical NCs.

Our results are instead at odds with the hypothesis that slow AR is connected with decreased electron confinement [142], as, despite exhibiting a nearly constant CBM energy (indication of a similar degree of electron confinement, which, as observed experimentally and discussed above, is determined by the arm diameter), TPs with same D and increasing L display increased AR lifetimes.

So far we have considered perfectly symmetric structures, where all four arms are equal in diameter and length. Before we conclude, we would like to briefly discuss the effect on our results of the presence of the following structural modifications, that may realistically occur in experimental samples: (i) asymmetry in arm length L or diameter D, (ii) arm tapering, and (iii) crystal disorder. (i) Experimentally synthesized CdTe tetrapods have been reported [41] to have four arms that are equal to within a few percent. According to our calculations, a variation in D or L of up to 10% in one of the arms would not affect appreciably any of the decay times presented here, nor our conclusions. However, in the TPs with a stronger anisotropic arm (*e.g.* one of the arms is 25% longer/thicker than others), a significant influence on electronic and optical properties as well as the radiative and Auger rate is shown, which will be discuss in the next Chapter. (ii) Substantial tapering is observed in TPs with CdSe arms [85], but not in CdTe TPs [41]. According to atomistic SEPM calculations by Li and Wang [82], in case of asymmetric elongated shapes, where one end is wider than the other, (the situation found in TP arm tapering), the hole wave function would avoid the narrow region of the structure, as would that of the CBM, but not those of higher energy electronic states, which would, how-

ever, still retain some localisation in the wider region of the structure. Arm tapering would, therefore, not affect band edge recombination, but may lead to a partial reduction of AC rates in short armed TPs, due to the reduced wave function overlap between initial and final states. The extent of such a reduction, however, should decrease with increasing arm length L, as the electron wave function moves away from the core (see Fig. 3.3), leaving our conclusions largely unaffected. (iii) More problematic, from the point of view of its impact on our results, could be the possible presence, in experimental samples of tetrapods with CdTe arms, of structural disorder caused by the co-existence of both sphalerite and wurtzite domains. [85]. Due to the different position of the band edges in zinc-blende and wurtzite, the presence of such mixed phases would create local shallow potential wells that could trap the electron. This would not affect band gap radiative recombination (as both states involved reside in the TP core). Similarly, the presence of such defects should not affect AR rates either, as the states involved in this process are either CBM and VBM (localised in the TP core) or highly excited states, whose energy (about E_g above/below CBM/VBM) is much larger than the band edges' discontinuity.

3.3   Conclusions

We have presented a comprehensive theoretical characterisation of colloidal CdTe TPs with arm diameters D ranging from 1.9 nm to 2.8 nm, and arm lengths L from 1.75 nm to 14 nm, containing from about 1000 to over 6000 atoms. We have investigated the dependence on both these parameters of the electronic structure, the optical spectra, and the RR times. We found these nanostructures to have diameter-dependent and L-independent band edge energies, absorption onset and radiative lifetime. In contrast, Auger processes exhibit a marked dependence on the TP's arm length, as a consequence of the different spatial localisation of the excited states' wave functions compared to the band edges charge densities. This provides the ability to tune the TP's emission in the visible region of the electromagnetic spectrum, by selecting the appropriate arm diameter, while suppressing, at the same time, Auger cooling and recombination, by choosing a suitable value for the arms' length. In other words, these extremely versatile nanostructures enable, by virtue of their shape alone, a complete decoupling of Auger and RR. Furthermore, owing to their large volume, these systems also have the added benefits of an increased absorption cross section (directly dependent on the volume V), decreased thresholds for optical gain and for development of amplified spontaneous emission

(both inversely dependent on V) [141], and reduced photoinduced absorption (also inversely dependent on V) [143]. All these features make CdTe TPs ideally suited for applications as efficient light-emitting media.

This chapter was published in J. Phys. Chem. Lett. 2021, 12, 37, 9155–9161

Chapter 4

The Effects of Structural Asymmetries in Tetrapods

4.1 Introduction

The possibility of combining different material components in core/arms tetrapods (TPs) [85], [88], [144], [145], or, using the TPs as seeds for the growth of spherical nanoparticles on the tips of their arms, in metal- or semiconductor-tipped TP-shaped heterostructures [146], [147], has endowed these nanostructures with a wide functionality and applicability, and allowed a fine tuning of their properties. Another, so far little explored, degree of freedom that could lead to an even further refinement of the level of control over such properties is the introduction of anisotropies in the arm morphology. Indeed, variations in the length or diameter of one (or more) of the arms can occur either deliberately (i.e., by design [148]), or accidentally during the growth of these nanostructures [41], [83], [86], [88], [149]. Nevertheless, this aspect of shape engineering has received little attention in the literature.

In this chapter we aim to fill such a gap by addressing the following questions: (i) do shape anisotropies of the order of those that may occur accidentally during synthesis affect any of the TP properties? If so, (ii) what are their signatures? And (iii) can these anisotropies be exploited to widen the functionality of these nanostructures?

That shape anisotropies can indeed accidentally occur in experimental samples is suggested by the observation of pronounced emission anisotropies accompanied by a decrease in PL

intensity in CdSe/CdS TPs [149], which has been attributed [149] to the presence of asymmetric TPs with one arm thicker than the others, based on simple wave function overlap arguments within the effective mass approximation. This interpretation, however, has not been tested so far by more rigorous theoretical models, that account for both the atomistic nature of the nanostructure and the non trivial effects of electron-hole interactions.

To shed light on all these issues, we carried out a theoretical characterisation, based on same theoretical approach used in Chapter II and III Part II (SEPM), of TPs with anisotropic geometry (for simplicity, we consider variations in length or diameter of a single arm only, out of 4, i.e., TPs with one arm longer or thicker than the others). We consider TPs with two different aspect ratios (which include experimentally relevant ones[84]–[86], [150], [151]) $\rho = L_n/D_n = 1.7$ and 6.7 (henceforth referred to as small aspect ratio, SAR, and large aspect ratio, LAR, structures, respectively), of nominal (n) arm length (L_n) over arm diameter (D_n), for two values of the former ($L_n \sim 3.5$ nm and $L_n \sim 15$ nm) and a single diameter ($D_n \sim 2.1$ nm), containing from about 2000 to over 9500 atoms. The increase in the anisotropic arm length is 25% for LAR structures and 50% for SAR TPs, whereas the increase in arm thickness is 25% for both. This allows us to explore possible differences between the behaviour of SAR and LAR structures (or, in other words, between small, short-armed TPs and large long-armed ones), addressing the important question of whether it is possible to use the former to predict the properties of the latter, for both symmetric and asymmetric TPs.

We consider the TPs discussed in Chapter II and Chapter III: homogeneous (i.e., same-material) CdTe TPs [41] with a type I band structure, and heterostructured (i.e., core/arms) CdTe/CdSe TPs [152] with a type II band alignment at the core/arm interface [92]. This allows us to investigate the effects of anisotropies in branched nanocrystals with different band structures, exhibiting localisation of the charge carriers in different spatial locations, for both SAR and LAR nanostructures.

Our results show unexpected features in: (a) the emission polarization and its temperature dependence in anisotropic structures, suggesting a prominent role of excitonic effects over single-particle properties; (b) the localization of the charge density in equivalent structures with different aspect ratios, suggesting the need for extreme caution when extrapolating electronic and optical properties of large, long armed anisotropic TPs from those obtained from small, short-armed ones; (c) the rates of Auger processes in branched nanostructures with different

anisotropies. We also find that, although SAR structures surprisingly exhibit similar optical properties in TPs with type I and type II band structures, LAR structures present markedly different behaviours, dictated by the very different charge density distribution within their volume.

4.2 Results and Discussion

4.2.1 Charge distribution

We will start by analysing the charge density distribution in anisotropic structures and comparing it with that calculated for perfectly symmetric TPs. This will yield the first indication of the effect of reduced confinement along either the length or the width of the non-symmetrical arms.

CdTe TPs

As presented in Fig. 4.1, in SAR homogeneous TPs, the CBM ($e1$) charge density distribution is similar in all three types of nanostructures considered (symmetric, longer arm (LA) and thicker arm (TA) tetrapods), and is mainly localised in the core (leaking, however, considerably in the thick arm in TA TPs, where this reduction in confinement is also accompanied by a ~ 25 meV lowering of the energy). The greater difference in the CB charge densities is found in the next CB state, $e2$, which, in symmetric TPs, is nearly degenerate with $e3$ and $e4$ and is distributed uniformly on all four arms (with some small density also found in the core), whereas in LA TPs it has an energy ~ 30 meV lower and is all localised in the long arm, and in TA structures it is mainly localised in the thick arm and in the core, with an energy nearly 100 meV lower than in the symmetric structure. The CB state $e3$ is similar in TA and LA TPs, where it localises in the three equal arms but not in the different arm; in the symmetric TP, $e3$ is mainly in two arms with some localisation in the third arm and less in the fourth. The same considerations hold for $e4$ (which is degenerate with $e3$ in the symmetric TP and nearly degenerate with $e3$ in LA and TA), for which, however, in the symmetric TP the localisation is reversed (high in the arms where it was low in $e3$ and *vice versa*). $e5$ looks very similar in all structures, with charge delocalised on all arms and in the core.

The electron charge distribution in LAR symmetric and LA structures (See Fig. 4.2) exhibits very similar characteristics to that in SAR TPs with the difference that now $e2$-$e5$ are nearly de-

Figure 4.1: Charge densities (red) calculated for the lowermost 5 conduction band states in CdTe TPs with $D_n = 2.2$ nm and $L_n = 3.7$ nm and 4 symmetric arms (top panels), one longer arm ($L = 5.6$ nm, middle panels), and one thicker arm ($D = 2.8$ nm, bottom panels). Also reported are the corresponding energies, relative to vacuum. Blue and cyan dots represent Cd and Te atoms. The direction of each arm is shown in the first panels on the left-hand side.

Figure 4.2: Charge densities (red) calculated for the lowermost 5 conduction band states in CdTe TPs with $D_n = 2.2$ nm and $L_n = 15$ nm and 4 symmetric arms (top panels), one longer arm ($L = 18.7$ nm, middle panels), and one thicker arm ($D = 2.8$ nm, bottom panels). Also reported are the corresponding energies, relative to vacuum. Blue and cyan dots represent Cd and Te atoms. The direction of each arm is shown in the first panels on the left-hand side.

generate. In both, the CBM is localised mainly in the core, whereas *e*2-*e*5 are all localised in the long arms and far away from the core. Completely different is, instead, the charge distribution in the TA TP, which is concentrated in the TA for states *e*1-*e*5 (and also extends to the core in states *e*2-*e*4), resembling that of a quantum rod with σ-like symmetry [132], exhibiting 0, 1, 2, and 3 nodes along the arm. Most importantly, unlike in any other CdTe TP, the CBM of the TA structure has no density in the core.

The holes' charge density is much less confined to the core and tends to expand more into the arms than the electrons' for all states in both SAR and LAR structures (see Fig. 4.3 and Fig. 4.4). It is also more localised inside the TP than on its surface compared with the electrons'. As in the case of the electron energies, elongation or thickening of one arm lifts the degeneracy of the VBM in SAR TPs, increasing its energy by 4 meV and 39 meV in LA and TA structures, respectively. In LAR TPs, instead, arm elongation does not alter the VBM energies, whereas arm thickening leads to a 67 meV increase in the VBM energy and to a lifting of degeneracies.
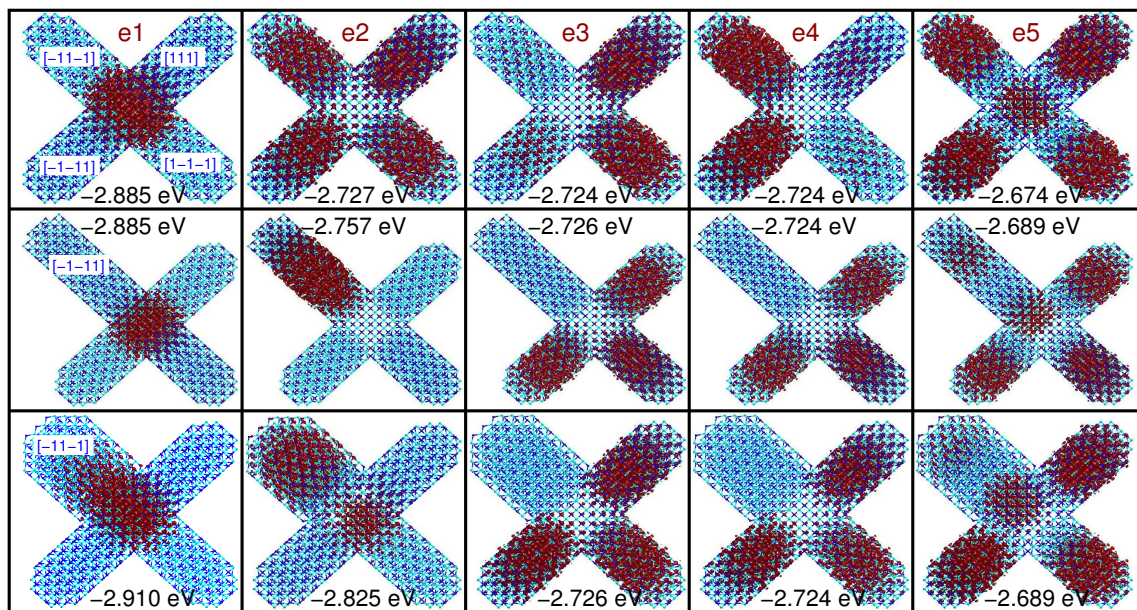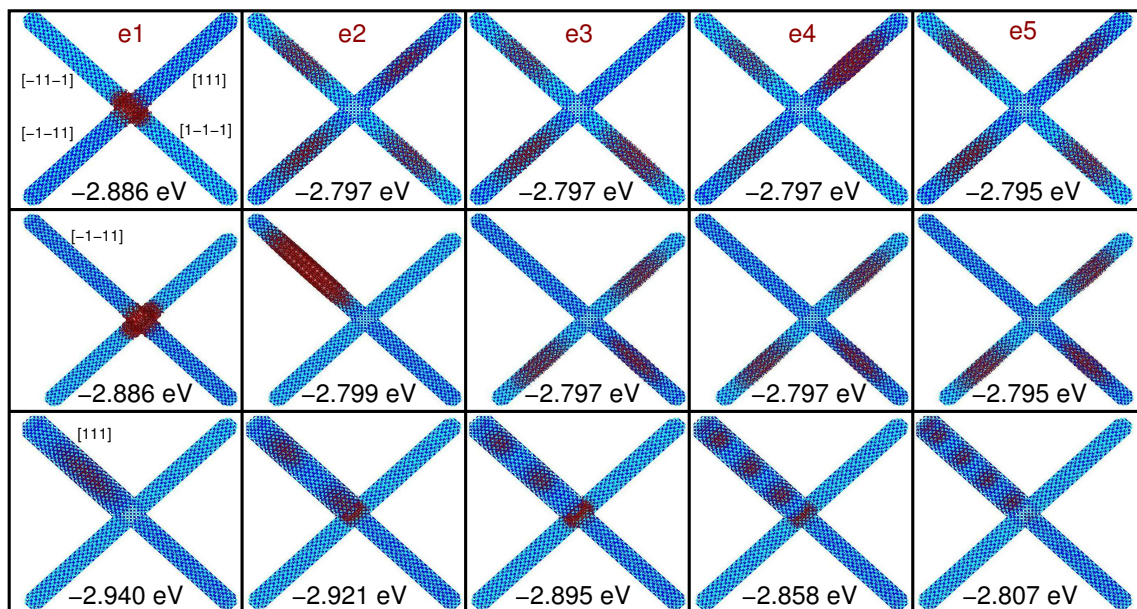

Figure 4.3: Charge densities (red) calculated for the uppermost 5 valence band states in CdTe TPs with $D_n = 2.2$ nm and $L_n = 3.7$ nm and 4 symmetric arms (top panels), one longer arm ($L = 5.6$ nm, middle panels), and one thicker arm ($D = 2.8$ nm, bottom panels). Also reported are the corresponding energies, relative to vacuum. Blue and cyan dots represent Cd and Te atoms. The direction of the arms is the same as shown in Fig. 4.1.
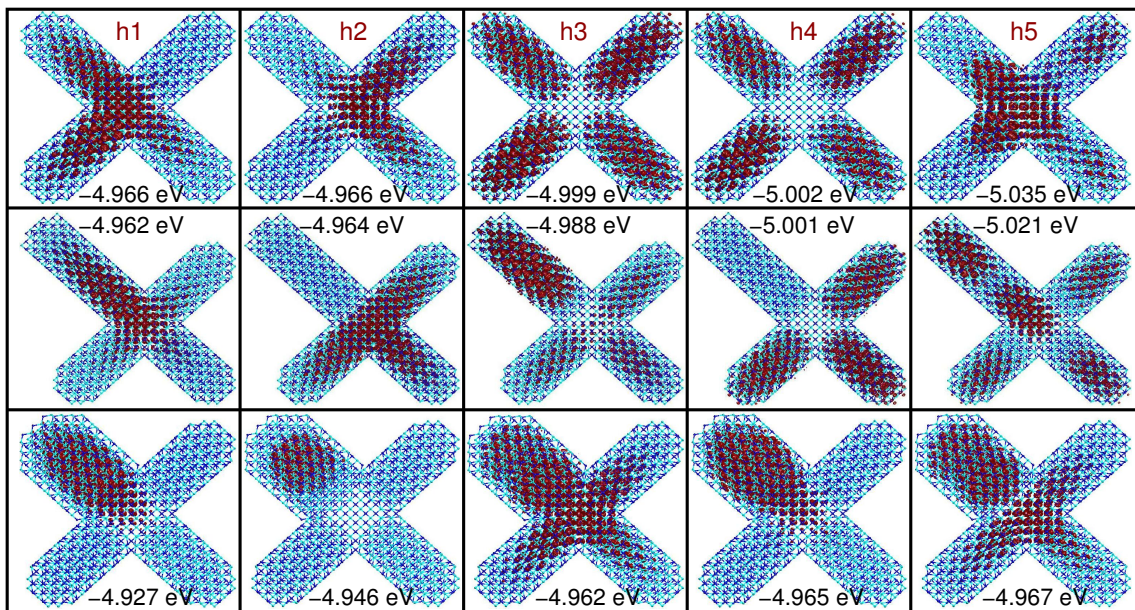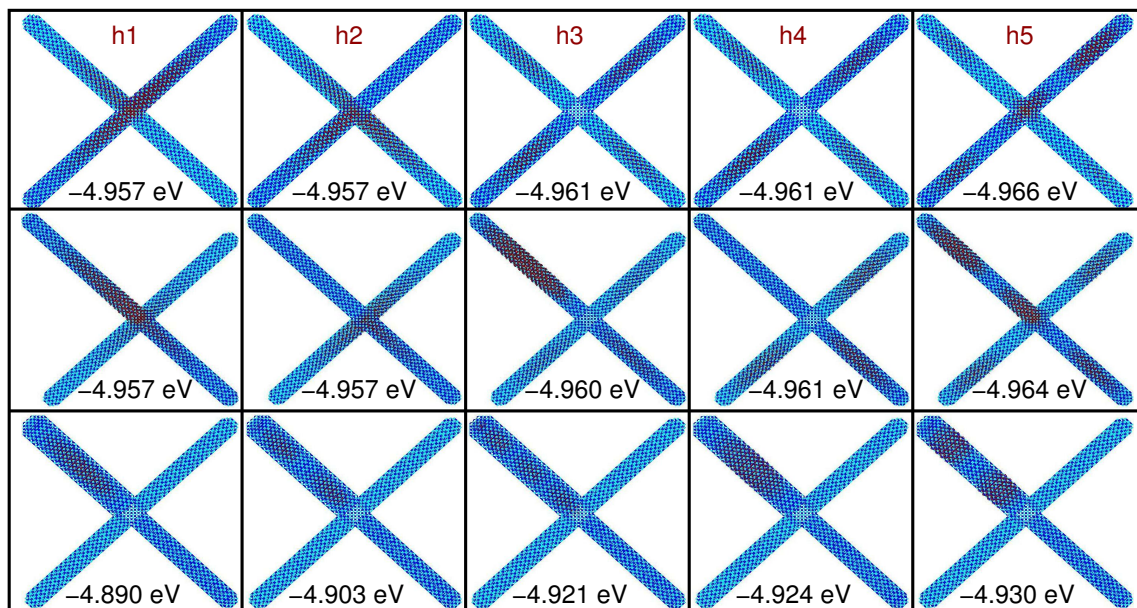
Figure 4.4: Charge densities (red) calculated for the uppermost 5 valence band states in CdTe TPs with $D_n = 2.2$ nm and $L_n = 15$ nm and 4 symmetric arms (top panels), one longer arm ($L = 18.7$ nm, middle panels), and one thicker arm ($D = 2.8$ nm, bottom panels). Also reported are the corresponding energies, relative to vacuum. Blue and cyan dots represent Cd and Te atoms. The direction of each arm is shown in the first panels on the left-hand side.

CdTe/CdSe core/arms TPs

The main difference between the charge densities in CdTe/CdSe and CdTe TPs is that the CBM is always localised in the core in the latter (with the exception just discussed), whereas, due to the band alignment at the CdTe/CdSe interface, it is confined to the arms in the former, resulting in the localization on the asymmetric arm in anisotropic structures. As presented in Fig. 4.5, in all SAR CdTe/CdSe TPs the charge distribution of state en is similar to that of $e(n+1)$ (for $n = 1, 2, 3$) in the corresponding SAR CdTe TPs. Similarly for LAR LA structures. In the case of LAR TA TPs (see Fig. 4.6), the charge distribution for $e1$-$e4$ is very similar in both CdTe/CdSe and CdTe (apart from some sampling of the core occurring in the latter), both displaying 0 and 3 nodes along the TA. Furthermore, $e1$-$e5$ have also similar densities in LAR symmetric and LA TPs (including the presence of a node along the arm in $e5$, although the charge density is confined to the long arm only, in LA TPs, and spread across all 4 arms in symmetric structures). In symmetric LAR TPs $e1$-$e4$ are nearly degenerate (their energies all lie within less than 0.15 meV from each other), whereas we find that the relaxation of confinement along the arm length in LA structures leads to an energy lowering of the CBM of about 8 meV (that however leaves the degeneracy of $e2$-$e4$ intact), which become 155 meV in the case of

Figure 4.5: Charge densities (red) calculated for the lowermost 5 conduction band states in CdTe/CdSe TPs with $D_n = 2.1$ nm and $L_n = 3.5$ nm and 4 symmetric arms (top panels), one longer arm ($L = 5.26$ nm, middle panels), and one thicker arm ($D = 2.6$ nm, bottom panels). Also reported are the corresponding energies, relative to vacuum. Blue dots represent Cd atoms and cyan dots Te and Se atoms. The direction of each arm is shown in the first panels on the left-hand side.
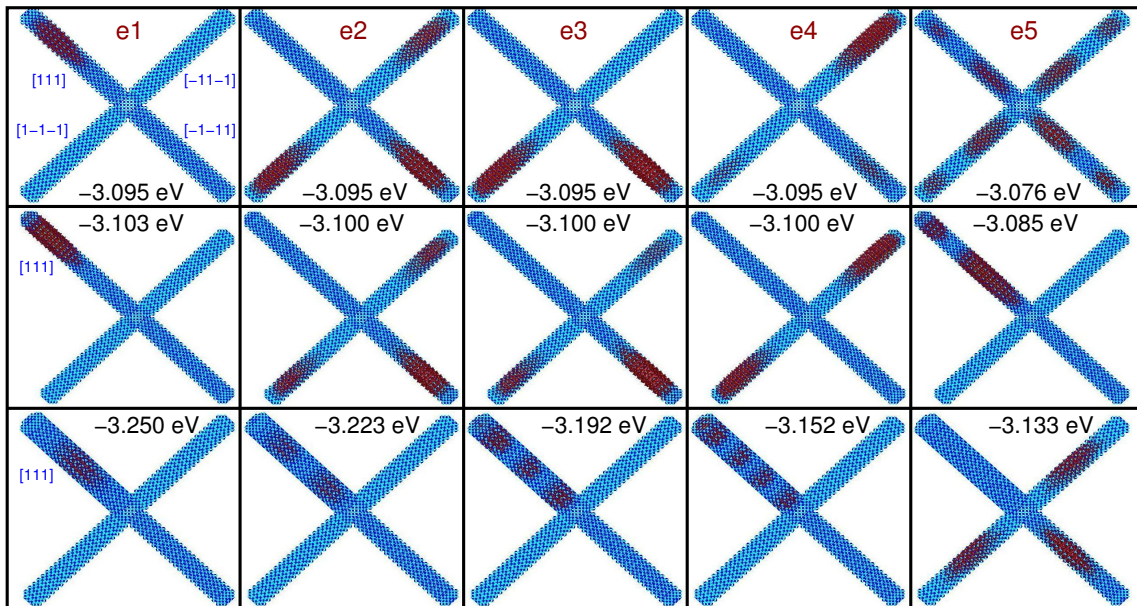
Figure 4.6: Charge densities (red) calculated for the lowermost 5 conduction band states in CdTe/CdSe TPs with $D_n = 2.1$ nm and $L_n = 14$ nm and 4 symmetric arms (top panels), one longer arm ($L = 17.55$ nm, middle panels), and one thicker arm ($D = 2.6$ nm, bottom panels). Also reported are the corresponding energies, relative to vacuum. Blue dots represent Cd atoms and cyan dots Te and Se atoms. The direction of each arm is shown in the first panels on the left-hand side.

an increase in the arm diameter. The latter increase also leads to a complete lifting of the degeneracy of $e1$-$e4$ resulting in four completely separate rod-like states with σ-like symmetry and different number of nodes along the arm, as in the case of type I TPs.
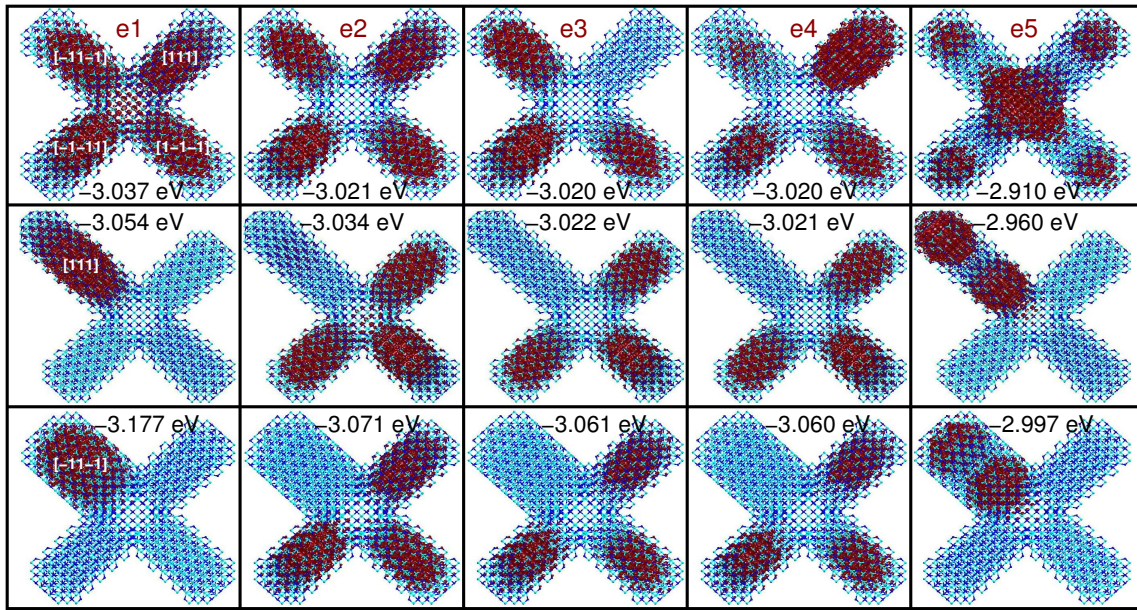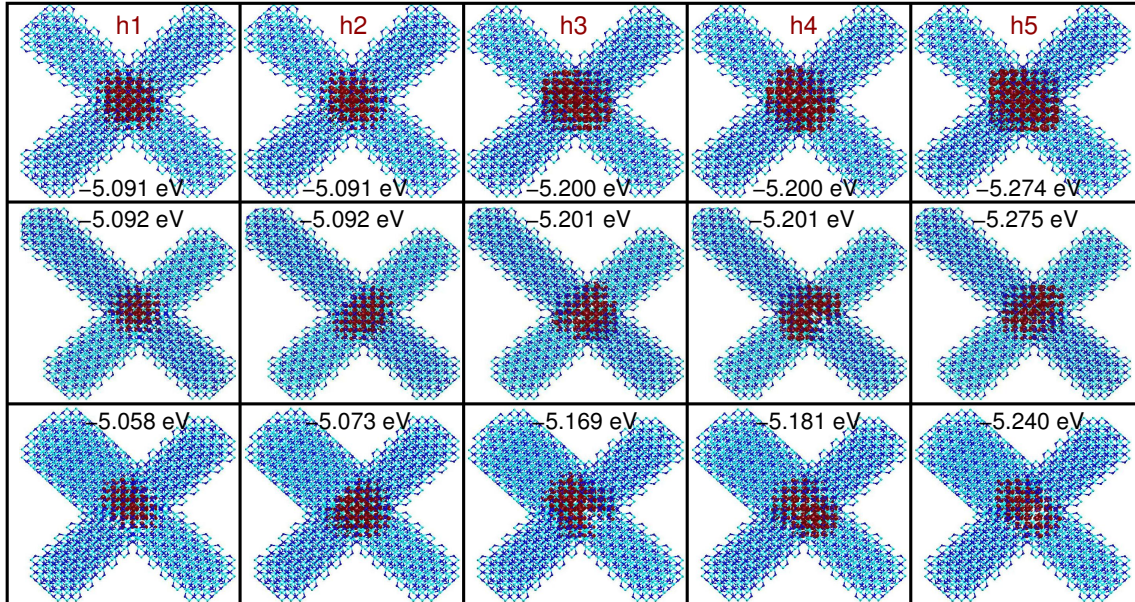

Figure 4.7: Charge densities (red) calculated for the uppermost 5 valence band states in CdTe/CdSe TPs with $D_n = 2.1$ nm and $L_n = 3.5$ nm and 4 symmetric arms (top panels), one longer arm ($L = 5.26$ nm, middle panels), and one thicker arm ($D = 2.6$ nm, bottom panels). Also reported are the corresponding energies, relative to vacuum. Blue dots represent Cd atoms and cyan dots Te and Se atoms. The direction of each arm is shown in the first panels on the left-hand side.

The biggest difference between CdTe and CdTe/CdSe TPs is, however, in the hole charge distribution, which is strictly confined to the core in the latter (at least for $h1$-$h5$, see Fig. 4.7 and Fig. 4.8), and allowed everywhere in the former nanostructures (Fig. 4.3 and Fig. 4.4). This difference determines the magnitude of electron-hole overlaps and dipole matrix elements, which affect the optical properties of the system.
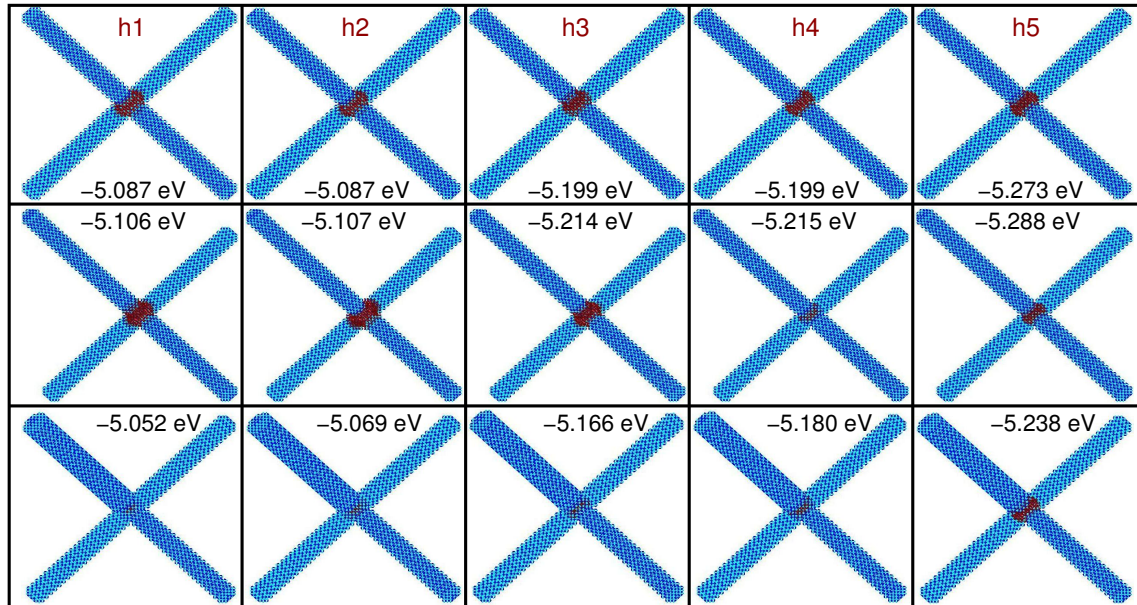
Figure 4.8: Charge densities (red) calculated for the uppermost 5 valence band states in CdTe/CdSe TPs with $D_n = 2.1$ nm and $L_n = 14$ nm and 4 symmetric arms (top panels), one longer arm ($L = 17.55$ nm, middle panels), and one thicker arm ($D = 2.6$ nm, bottom panels). Also reported are the corresponding energies, relative to vacuum. Blue dots represent Cd atoms and cyan dots Te and Se atoms. The direction of each arm is shown in the first panels on the left-hand side.

4.2.2 Optical properties

The position of the first absorption peak is nearly identical in both symmetric and LA structures, whereas in TA TPs it is red-shifted in all materials (Fig. 4.9), according to the observed dependence of the band gap on the width but not the length of the TP arms [129]. A similar behavior is also found for the PL peak position. The room temperature radiative lifetimes (τ_{rad}) are all very similar (ranging between 23 and 29 ns) in CdTe TPs with both short (SAR, empty symbols in Fig. 4.9c) and long (LAR, solid symbols in Fig. 4.9c) arms, reflecting the similar extent of the electron-hole overlaps in these systems (Fig. 4.10a). In SAR CdTe/CdSe TPs, τ_{rad} is about a factor of 2 longer and is nearly identical in symmetric and LA structures (~ 46 ns) and about a factor of 2.5 larger (112 ns) in TA TPs (see empty symbols in Fig. 4.9f). Unfortunately, the excessive supercell sizes of anisotropic LAR CdTe/CdSe TPs forced us to use a reduced basis set (rbCI) in our excitonic modelling [105], [153], [154] of these structures, instead of the larger set that was employed in the case of CdTe TPs. In this approximation, τ_{rad}^{rbCI} was found to be fastest (940 ns) in TA, nearly two orders of magnitude slower in symmetric (67140 ns), and slowest in LA (105100 ns) TPs (see orange, cyan and dark green symbols - slightly shifted to the right for clarity - in Fig. 4.9f, for symmetric, LA and TA structures, respectively).
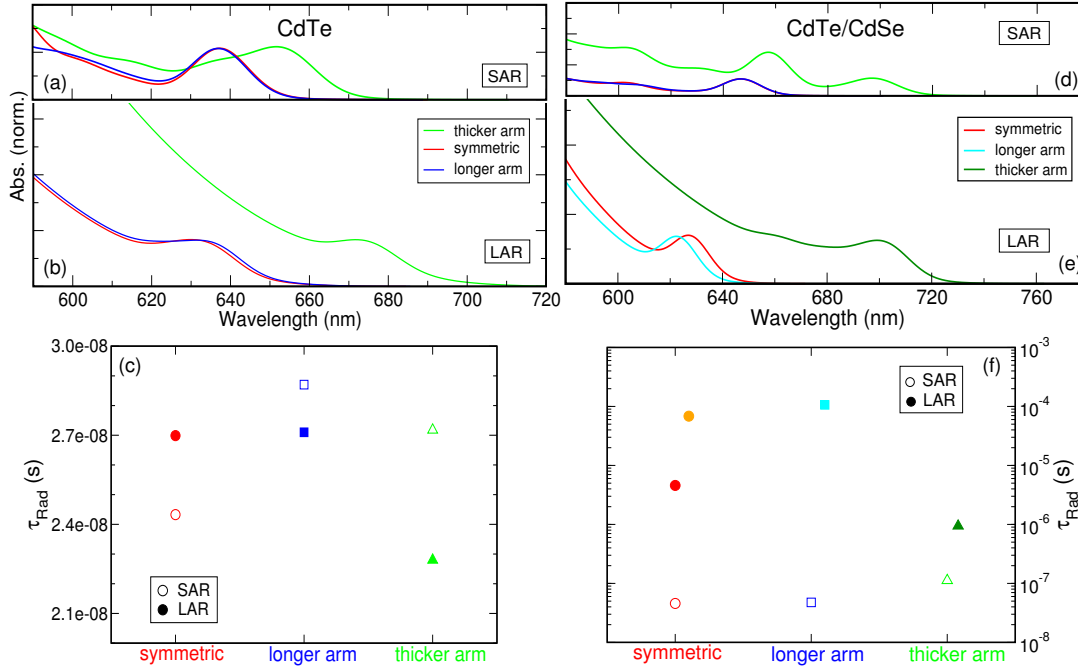
Figure 4.9: Optical properties: Absorption spectra [(a), (b), (d), (e)] and room temperature radiative recombination times [(c) and (f)], calculated for SAR [(a) and empty symbols in (c): $L_n = 3.7$ nm; (d) and empty symbols in (f): $L_n = 3.5$ nm] and LAR [(b) and solid symbols in (c): $L_n = 15$ nm, (e) and solid symbols in (f): $L_n = 14$ nm] CdTe TPs with $D = 2.2$ nm [(a), (b) and (c)], and CdTe/CdSe TPs with $D = 2.1$ nm [(d), (e) and (f)], and symmetric (red and orange symbols and lines), LA (blue and cyan symbols and lines) and TA (green symbols and lines) morphology. Results obtained within the reduced-basis-set approximation are displayed in a different shade (orange, cyan and dark green for symmetric, LA and TA structures, respectively), and shifted slightly to the right in panels (c) and (f) for clarity.

A wide basis set configuration interaction (CI) calculation [153], [154], which could be performed only for symmetric TPs, yielded radiative lifetimes a factor ~ 15 faster ($\tau_{rad}^{CI} = 4574$ ns - solid red circle in Fig. 4.9f - vs $\tau_{rad}^{rbCI} = 67140$ ns - solid orange circle in Fig. 4.9f), than obtained in the rbCI approximation. Assuming the same scaling constant applied to the other shapes, we estimated $\tau_{rad} \approx 64$ ns in TA, and 7160 ns in LA TPs.

Let's consider the reliability of such an assumption. In the case of CdTe TPs, two similar (rbCI)/CI scaling constants were found for symmetric and TA LAR TPs (equal to 1.5 and 1.4, respectively), whereas for SAR structures the calculated scaling constants in symmetric, LA and TA TPs ranged from 1.25 to 1.6. Finally, in CdTe/CdSe SAR TPs the variation in the scaling constant was within a factor of about 1.6 (from 2.1 to 3.4) for all geometries. These results suggest the above estimates to be reasonable, as the scaling constants of TPs of a specific material and aspect ratio were all found to be very similar, differing by a factor of at most 1.6.
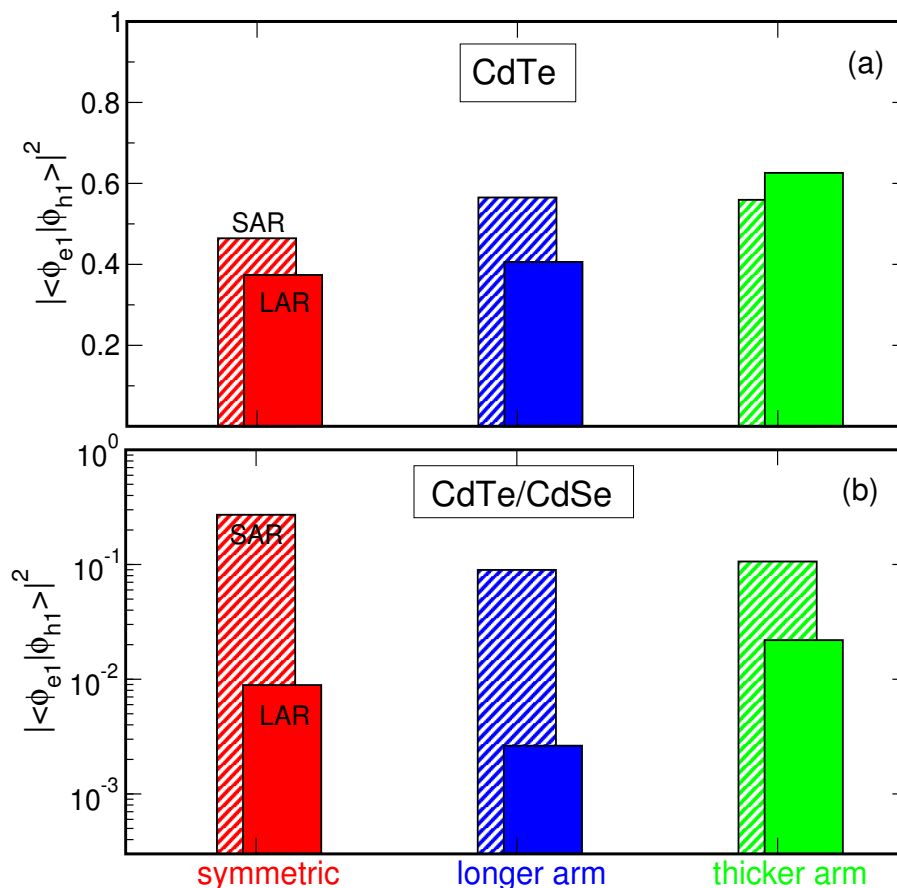
Figure 4.10: Overlaps between CBM (e1) and VBM (h1) calculated for CdTe [(a)] and CdTe/CdSe [(b)] SAR (dashed bars) and LAR (solid bars) structures with symmetric (red bars), LA (blue bars) and TA (green bars) morphology. The bars relative to LAR TPs are slightly shifted to the right for clarity. For comparison, the e1-h1 overlap calculated for a spherical CdTe nanocrystal with $D = 2.4$ nm is 0.62 (and 0.60 for a CdSe NC with $D = 2.0$).

Emission from a highly symmetric and isotropic structure is expected to be unpolarised and temperature-independent (according to Ref.[149] we define emission polarization as $P = (I_{max} - I_{min})/(I_{max} + I_{min})$ where I is the emission intensity along any TP arm).

This assumption is confirmed by our findings for all structures except for LAR CdSe/CdTe TPs (see red circles in Fig. 4.11). This surprising result is due to the fact that these are the only structures where the CBM is four-fold degenerate, with each of the states exhibiting a non-symmetric electron charge distribution (see Fig. 4.6). With the doubly degenerate VBM (Fig. 4.8), this yields a 32-fold degenerate ground state exciton, which is split by exchange interaction into multiplets laying within 6 meV from the ground state, so that, at low temperature, only part of them are occupied and can contribute to the PL, yielding emission with similar intensity from all but one of the arms. At room temperature all states are accessible, resulting in the expected unpolarised emission.
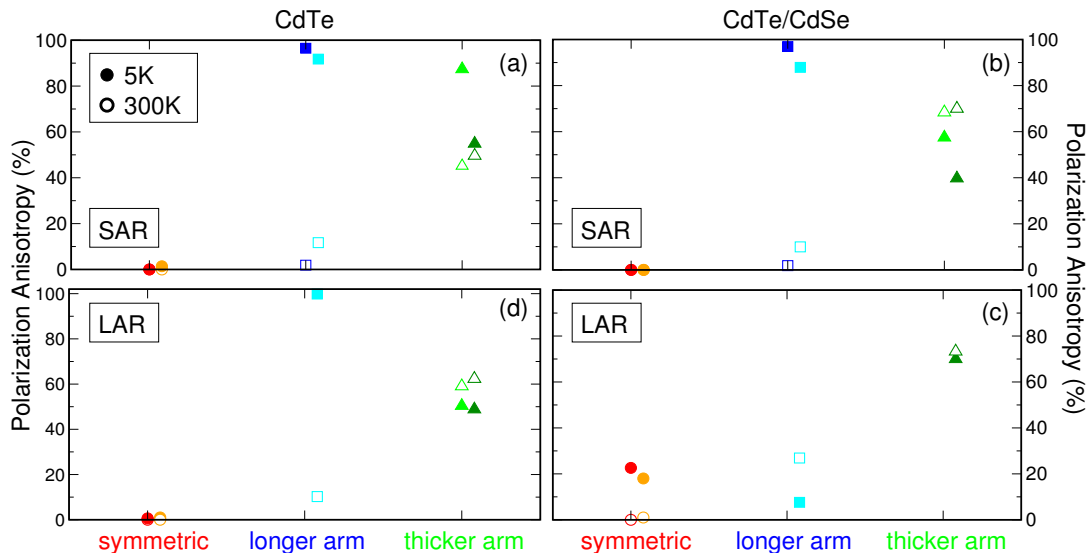
Figure 4.11: Emission polarization calculated for SAR [(a) and (b)], and LAR [(c) and (d)], CdTe [(a) and (d)], and CdTe/CdSe [(b) and (c)] TPs with symmetric (circles), LA (squares) and TA (triangles) morphology. The results obtained with a reduced basis set (rbCI) relative to each shape are displayed (in a different shade - orange, cyan and dark green, for symmetric, LA and TA, respectively - and slightly shifted to the right for clarity) for comparison. In the case of LAR structures of both materials it was not possible to perform a full CI calculation for the long arm (LA) TPs, so only rbCI results are presented (cyan squares). Similarly for the LAR TA CdTe/CdSe TP (dark green triangles). Where only one symbol is visible for the two temperatures (e.g., the solid red circle in CdTe SAR TPs), the polarization is temperature-independent.

In the case of LA SAR structures we find nearly 100% polarised emission at 5 K and nearly unpolarized emission at room temperature (see blue squares in Fig. 4.11a and b). The former, surprisingly, is due to a *weaker* PL along the long arm, compared to the other (same-sized) arms, which exhibit equally strong emission. Again the explanation of this unexpected behaviour is found in the details of the excitonic structure: in the case of CdTe TPs, the lowermost excitonic multiplet is contributed to mostly by $|h_2; e_1\rangle$ and only the following multiplet, higher in energy, and only accessible at room temperature, receives large contributions from $|h_1; e_1\rangle$. Considering the nearly isotropic distribution of the CBM charge density (Fig. 4.1), it is clear that the strength of the emission along the different arms is dictated by the VB charge densities shown in Fig. 4.3, where h_2 is distributed isotropically through the 3 equal arms (with little or no density in the long arm), whereas h_1 is localised mainly in the long arm and the core. Similarly, in the case of CdTe/CdSe, the weaker emission we find along the long arm is the result of the different contributions from $|h_1; e_1\rangle$ and $|h_1; e_2\rangle$ (where now it is the electron charge distribution that dictates the PL strength along the different arm directions, see Fig. 4.5) to the

lowermost excitonic manifolds.

A similar temperature-dependent emission polarization, also due to a weaker PL from the long arm at all T, is exhibited by CdTe LA LAR TPs, whose ground state excitons receive their main contribution from $|h_2; e_1\rangle$ (see Fig. 4.4), like SAR structures.

The only exception to this strong temperature dependence in the PL polarization of LA TPs was found in CdTe/CdSe LAR structures, whose anisotropy, unlike in all other LA structures, is larger at room temperature (with a weaker emission along the long arm) than at 5 K (when the emission along the long arm is stronger).

Quite different is the situation for all TA TPs considered in this study, which we find to exhibit polarized PL at all temperatures (see green triangles in Fig. 4.11). However, the details of their emission anisotropy vary with material and aspect ratio: in CdTe SAR structures, whilst at room temperature the emission is strongest along the thick arm direction [-11-1], at 5 K the opposite is true; similarly in CdTe/CdSe SAR TPs, with the important difference that P is larger at room temperature than at 5 K in this material; in CdTe and CdTe/CdSe LAR structures emission is found to be stronger along the thick arm at all temperatures, yielding a weakly temperature-dependent polarization anisotropy, which is larger at room temperature in both materials.

Unfortunately, as we mentioned above, for LAR asymmetric structures it was not always possible to carry out a complete excitonic modelling of the emission, owing to the large size of the supercell. In those cases (CdTe and CdTe/CdSe LA TPs, and CdTe/CdSe TA structures), rbCI was used in the calculations. In order to estimate the accuracy and reliability of such an approximation, we carried out calculations using the same approach for all structures considered and presented the results (displayed in a different shade - orange, cyan and dark green, for symmetric, LA and TA, respectively - and slightly shifted to the right for clarity) next to those obtained with a complete excitonic treatment in Fig. 4.11. We find that, in general, the two sets of results are close, suggesting rbCI to be a reasonable approximation to estimate anisotropies in the emission of these nanostructures.

structure	CdTe				CdTe/CdSe			
	SAR		LAR		SAR		LAR	
	5 K	300K	5 K	300K	5 K	300K	5 K	300K
LA								
Direction	3 arms	all arms	3 arms*	3 arms*	3 arms	all arms	LA*	3 arms*
Magnitude	97%	unpol.	100%	10%	97%	unpol.	8%	27%
TA								
Direction	3 arms	TA	TA	TA	3 arms	TA	TA*	TA*
Magnitude	88%	45%	52%	60%	58%	68%	70%	73%

Table 4.1: Summary of origins of PL anisotropies found in all asymmetric structures considered (LA and TA in SAR and LAR TPs, including polarization values from Fig. 4.11), identifying the directions (LA = along the long arm; TA = along the thick arm; 3 arms = equally along the directions of the same-sized arms) of the stronger emission, both at 5 K and at room temperature.
* obtained with a reduced-basis-set approximation (rbCI), due to the impossibility of carrying out a complete excitonic modelling (see text), owing to the large size of the structure.

A summary of the results just discussed, indicating the different directions where PL is stronger in different structures, materials and temperatures, is presented in Table 4.1. It is interesting to compare these results with the (normalized) dipole matrix elements calculated between single-particle states $P_j = |\langle \psi_{cbm}|p_j|\psi_{vbm}\rangle|$ (where j represents a specific arm direction, e.g. [111], and ψ_{cbm} and ψ_{vbm} are the band edges' wave functions. The matrix elements also include a sum over degenerate CBM and/or VBM states, depending on the structure), presented in Fig. 4.12. It is clear that, whilst the dipole matrix elements' anisotropy reflects the asymmetries exhibited by the charge density distribution (Figs. 4.1-4.8) the anisotropy found in PL, and, more in particular, its temperature dependence, is the result of more subtle and often unexpected effects, whose origin lies in the excitonic nature of emission. It is therefore not straightforward to predict the direction of the strongest PL in an anisotropic TP just from simple arguments based on the symmetry of the band edges' wave functions.

The polarization anisotropy in the light emitted by 200 single CdSe/CdS TPs ($D = 4$-6 nm and $L = 14$-20 nm) at 5 K and at room temperature was measured by Mauser et al. [149]. They found that at 5 K more than 50% of the TPs showed over 50% polarization, with the most probable values peaking at 70%, whereas at 300 K the anisotropy peak shifted to 30%. They explained such a surprising result invoking a wave function symmetry breaking originating from the prevalence of TPs with one asymmetric arm (with increased diameter compared to the other arms) in their sample, based on a simplistic effective mass modelling.
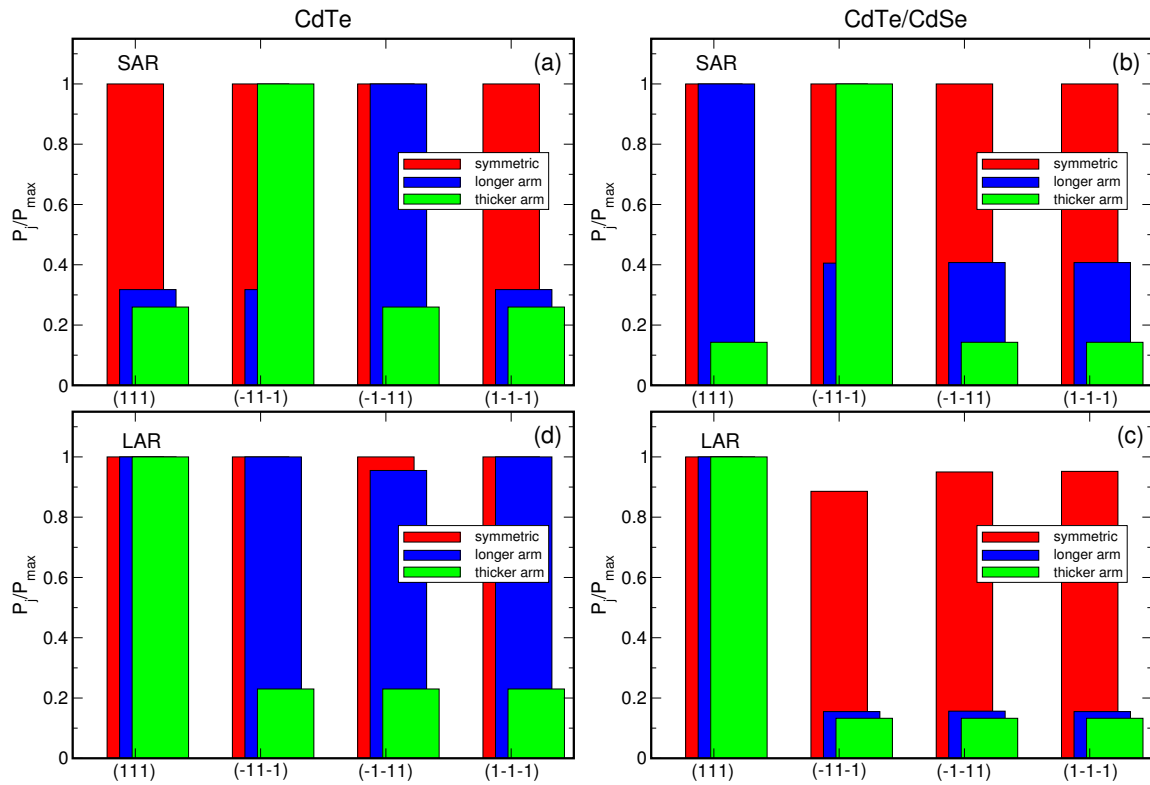
Figure 4.12: Single-particle normalized dipole matrix elements calculated for SAR [(a) and (b)], and LAR [(c) and (d)], CdTe [(a) and (d)], and CdTe/CdSe [(b) and (c)] TPs with symmetric (red bars), LA (blue bars) and TA (green bars) morphology. The bars relative to each direction are slightly shifted for clarity. In panel (a) the long arm is along (-1-11), and the thick arm is along (-11-1); in (b) the long arm is along (111), and the thick arm is along (-11-1); in (c) both the long arm and the thick arm are along (111); in (d) the long arm is along (-1-11), and the thick arm is along (111).

The dipole matrix elements in LAR symmetric CdTe/CdSe TPs are not isotropic, as the CBM is 4-fold degenerate in that structure and the charge distribution in the arms are different in the different states e_1-e_4. The arm (direction) in which the matrix element is larger is where e_1 is localised. The matrix elements of all other structures are consistent with the charge density distributions shown in Figs. 4.1-4.8.

Considering that in a CdSe/CdS TP the hole is confined to the core whereas the electron is delocalized throughout the structure, the system that better approximates its properties, among the ones studied here, is a CdTe TP, since in CdTe/CdSe TPs the CBM electron has no access to the core region. As it is shown in Fig. 4.11, however, we find no strong temperature dependence in the polarization anisotropy of TA structures of either material for arm lengths in the experimental range (L_n = 14-15 nm in our LAR structures), in contrast to the experimental findings [149]. Furthermore, even the weak temperature dependence exhibited by CdTe TA TPs is reversed compared to experiment, with the larger polarization ($\sim$ 60%) occurring at room temperature. Only CdTe SAR TA structures show a temperature dependence comparable

to what was observed in CdSe/CdS TPs, with a nearly 90% polarization at low temperature, decreasing to about 45% at 300 K. However, the size of these nanostructures (L_n = 3.7 nm) is too small to be comparable with that of the experimental samples (L_n = 14-20 nm) [149]. Finally, the observed decrease in PL intensity with increased polarization [149] is not found in our CdTe TPs, where the PL intensity at 5K is nearly the same for symmetric (unpolarized emission) and LA structures ($\sim$ 100% polarized emission), and much larger for TA ($\sim$ 50% polarized emission).

Interestingly, effective mass calculations [149] predicted (i) a 100% overlap between electron and hole wave functions in a symmetric TP, which (ii) decreased to about 65% for an increase in the arm diameter of 1.5 nm, and (iii) an increase in the length of one arm to induce a negligible asymmetry in electron and hole wave functions, implying therefore unpolarized emission in LA TPs, as in the case of symmetric structures. In stark contrast with these predictions we find that: (i) the electron-hole overlap does not exceed 60% even in spherical CdSe NCs (or 70% in spherical CdTe NCs); (ii) it *increases* with increasing arm diameter (see Fig. 4.10), due to the localization of both carriers in the thick arm; (iii) LA structures exhibit the strongest temperature dependence in emission polarization anisotropy, ranging from a nearly 100% polarized PL at 5 K, to nearly unpolarized emission at room temperature, for nearly all materials and aspect ratios.

Our results therefore suggest that a more complex picture may lie behind the optical properties of the branched structures grown by Mauser et al. [149] than that provided by their single-particle effective-mass-based modelling.

4.2.3 Auger processes

Auger recombination

We will now shift our attention to Auger recombination (AR) processes, to see whether shape anisotropies can be detected from differences in their lifetimes.

We find that the AR lifetimes in the different SAR structures of type II (CdTe/CdSe) TPs are all similar and of the order of a few tens of picoseconds (ranging from 32 to 50 ps, see Fig. 4.13a). This is mainly the lifetime associated with excess holes (τ_h) which is about one order of magnitude (or more, in the case of TA structures) faster than that associated with excess electrons (τ_e). The latter is of the order of 1 ns for both LA and TA structures, compared to $\sim$ 200 ps in

symmetric TPs, making its measurement a reliable test of the presence of anisotropic structures in the sample.
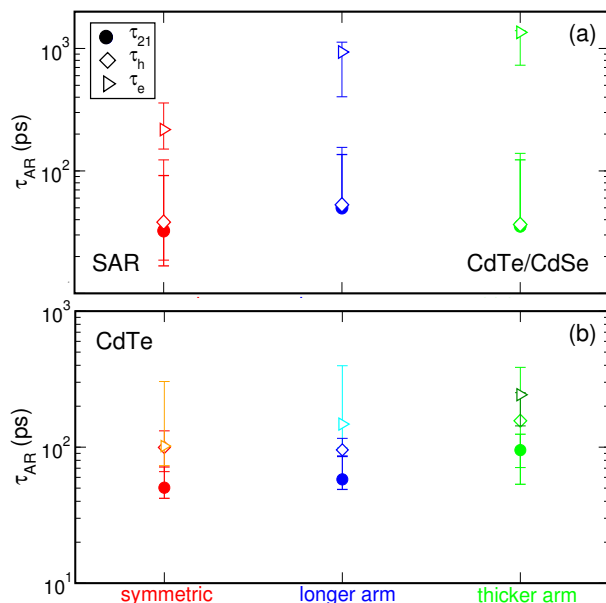
Figure 4.13: Auger recombination times calculated for CdTe/CdSe (a) and CdTe (b) SAR TPs with symmetric (red and orange symbols), LA (blue and cyan symbols) and TA (green symbols) morphology: the biexciton recombination times (solid circles) have been decomposed into the contributions from the recombination of a negative trion (open right triangles) and a positive trion (open diamonds). In the case of CdTe, the contributions from the negative trion have been marked with orange, cyan and dark green triangles to better distinguish them from the positive trion decay times.

In type I (CdTe) SAR TPs the decay times are slightly slower than in type II TPs, and range from about 50 ps (for both symmetric and LA structures), to 95 ps (for TA TPs). This difference could be too small to provide a clear signature of the presence of asymmetric TA TPs. The situation is completely different in CdTe LAR structures, where AR lifetimes of symmetric (380 ps) and TA (7.6 ns) TPs are separated by over one order of magnitude (unfortunately, we could not calculate AR times for LA structures). It is worth noting here that this twenty-fold increase is not due to a simple volume scaling, as the increase in AR times observed in spherical CdSe nanocrystals for a similar volume increase (i.e. less than 13%) is only of a factor of about 2 [102]. This effect is the result of a symmetry breaking in the electronic wave functions, that leads to a decreased overlap between excited states and band edges wave functions. For comparison, typical AR lifetimes in CdTe spherical dots with diameters of 2.1 nm are of the order of a few picoseconds [155], and decrease with decreasing dot size. The asymmetric growth of branched structures with one thicker arm leads therefore to a dramatic suppression of AR, yielding decay
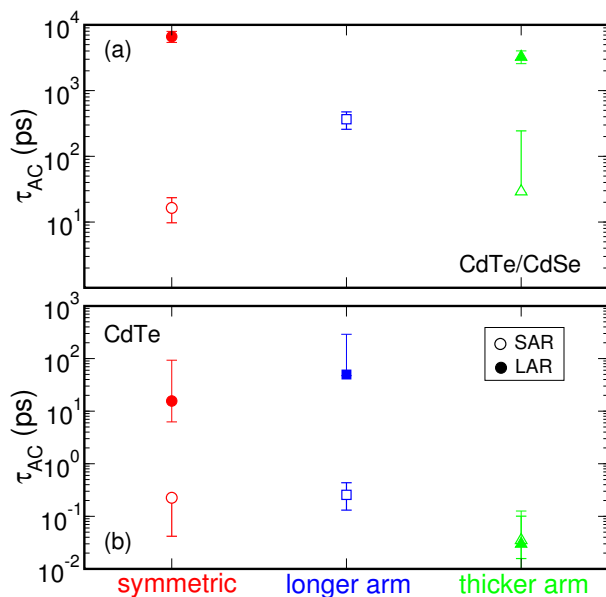
Figure 4.14: Auger cooling (AC) times calculated for SAR (empty symbols) and LAR (solid symbols) CdTe/CdSe (a) and CdTe (b) TPs with symmetric (red symbols), LA (blue symbols) and TA (green symbols) morphology.

times that are two to over three orders of magnitude longer than in spherical nanostructures with similar diameters, and increase with arm length from about 100 ps (for $L = 3.7$ nm) to about 10 ns (for $L = 15$ nm).

In contrast to the case of SAR asymmetric structures and LAR symmetric TPs, in CdTe LAR TA TPs it is the lifetime associated with excess electrons that determines the total AR time, as $\tau_h > \tau_e$ in these systems.

Auger electron cooling

Another interesting mechanism, which can allow the excited electron to overcome the phonon bottleneck and bridge energy gaps larger than 10 phonon energies in sub-picosecond times [156], is Auger electron cooling (AC). Typical AC times in spherical CdSe NCs with $D = 2.2$ nm are faster than 100 fs and increase with increasing radius, following a linear dependence [102]. In SAR CdTe TPs with $D = 2.2$ nm we also find sub-picosecond electron cooling times (see Fig. 4.14b), which are of a similar magnitude in symmetric and LA structures, but, in contrast to the case of spherical structures, are one order of magnitude *faster* in TPs in which one arm has a *larger* radius (TA TPs), reflecting a stronger Auger coupling between initial and final states that are all localised in the same arm. Interestingly, although AC times in SAR and LAR differ by nearly two orders of magnitude for symmetric and LA TPs, they are essentially the same (~ 30 fs) in TA structures, as a result of the peculiar carrier localisation achieved in

these TPs. We conclude that the presence of a sub-100 fs electron decay component in type I TPs of any aspect ratio should be considered as a clear signature of the presence of TA asymmetric structures.

In type II CdTe/CdSe TPs, instead, it is a slower electron decay that signals the presence of LA structures in SAR TPs (see Fig. 4.14a), whereas symmetric and TA structures exhibit similar AC lifetimes for all aspect ratios considered. As expected, owing to the weak overlap between band-edge electron and hole wave functions in these systems, the calculated AC times are at least two orders of magnitude longer than in type I TPs, leading to extremely long-lived electron excited states in the nanosecond range. This characteristic makes LAR type II TPs well suited for achieving population inversion build-up.

4.3   Conclusions

In summary, in this chapter we aimed to address: (i) the effects of shape anisotropies on the TP properties; (ii) the signatures of their presence; (iii) their possible exploitation to widen the functionality of these nanostructures; (iv) the differences between the behaviour of small, short-armed TPs with a relatively small number of constituent atoms and large, long-armed ones, with tens of thousands of atoms; (v) the possibility of using the former to predict the properties of the latter (for both symmetric and asymmetric TPs).

We found that many of the properties (i) and signatures (ii) are material-dependent, and vary between branched structures with type I and type II band structure, although there are some common features in both materials (a summary is provided in Table. 4.2). In terms of the optical properties, both absorption onset and emission peak positions are nearly identical in both symmetric and LA structures of all sizes and materials (the small difference in their position found in some CdTe/CdSe TPs would be masked by the experimental inhomogeneous broadening of the ensemble spectra), whereas in TA TPs they are clearly red-shifted in all materials, making these features ideal signatures to identify the presence of TA (but not LA) structures in an experimental sample. Measurements of radiative lifetimes cannot distinguish between symmetric and anisotropic structures or even between the different anisotropies (LA vs TA) in TPs with a type I band structure; this also holds in TPs with type II band structure for symmetric and LA structures, but not for TA TPs, which exhibit over one order of magnitude faster recombination times in LAR structures, and a factor of ~ 2 slower lifetimes in SAR TPs.

	Type I CdTe				Type II CdTe/CdSe			
	SAR		LAR		SAR		LAR	
	LA	TA	LA	TA	LA	TA	LA	TA
El. structure								
E(CBM)	=	<	=	<	<	≪	≈	≪
DoS(CB)	>	<	=	>	>	≪	≈	≪
E(VBM)	≈	>	=	>	=	>	<	>
DoS(VB)	≈	>	=	>	=	>	≈	<
Optical properties								
Absorption edge	=	<	≈	≪	=	≪	>	≪
PL energy	=	<	≈	≪	=	≪	>	≪
τ_{rad}	≈	≈	=	≈	≈	>	≫	<
Auger processes								
τ_{AC}	=	≪	>	≪≪	≫	>	?	≈
τ_{AR}	≈	>	?	≫	>	=	?	?

Table 4.2: Comparison of some of the properties (CB and VB band edge energies, and density of states [DoS]; position of absorption edge and PL, radiative recombination time [τ_{rad}]; Auger cooling [AC] and recombination [AR] times) of type I and type II SAR and LAR asymmetric structures with those of the corresponding symmetric TPs, showing when they are the same (=), similar (≈), larger/smaller (>/<), or much larger/smaller (≫/≪).

Another distinguishing feature of asymmetric TPs is their strong emission polarisation (with all of our TA structures showing a polarization ≥ 45% along the TA at room temperature), especially at low temperature (where nearly all of our LA TPs are ∼ 100% polarized), which makes them particularly well suited for orientation-sensitive applications (iii).

For temperature-independent polarized emission applications (iii), TA LAR TPs of either type I or type II TPs are equally well suited, as their strongest PL is always along the TA, and with a degree of polarization nearly constant with varying temperature, as in the case of quantum rods [157]. Indeed, this property is a consequence of the close resemblance of their electron charge density distribution to that of elongated nanocrystals [132]. In general, however, the direction of the strongest PL in an anisotropic TP is the result of non-trivial electron-hole interactions and cannot be predicted from simple arguments based on the symmetry of the band edges' wave functions.

The increase in diameter of a single arm in CdTe TPs leads to increases in AR decay times by a factor of 2 - for SAR structures - to 20 - in LAR TPs - (with the potential for greater increases in structures with longer arms), providing a simple strategy to achieve a strong AR suppression of over 3 orders of magnitude, compared to NCs of the same material with similar diameters, which would benefit applications in solar energy harvesting such as PV and photocatalysis

(iii). It also leads to a one (in SAR TPs) to 3 (in LAR structures) orders of magnitude decrease in the Auger electron cooling times, resulting in faster decays than in spherical dots with similar diameters. Furthermore, compared to the latter, in these structures the AC lifetimes exhibit an opposite trend with size, decreasing when the diameter of a single arm is increased. In contrast, type II LAR TPs are ideally suited for applications that require the build-up of population inversion, as their excited electron lifetimes approach the 10 ns mark.

	Type I			Type II		
	Symm	LA	TA	Symm	LA	TA
El. structure						
E(CBM)	✓	✓	✗	✗	✗	✗
DoS(CB)	✗	✗	✗	✗	✗	✗
CB charge density	✓	✓	✗	✗	✓	✗
E(VBM)	✓	✓	✗	✓	✓	✓
DoS(VB)	✗	✗	✗	✓	✓	✓
VB charge density	✓	✓	✗	✓	✓	✓
Optical properties						
Absorption edge	✓	✓	✗	✓	✓	✗
PL energy	✓	✓	✗	✓	✓	✗
PL pol. and T dep.	✓	✓	✗	✗	✗	✓
τ_{rad}	✓	✓	✓	✗	✗	✗
Auger processes						
τ_{AC}	✗	✗	✓	✗		✗
τ_{AR}	✗		✗	✗		

Table 4.3: Summary of LAR TP properties (CB and VB band edge energies, density of states [DoS], and charge densities; position of absorption edge and PL, emission polarization and its temperature [T] dependence, radiative recombination time [τ_{rad}]; Auger cooling [AC] and recombination [AR] times) that can (✓) and cannot (✗) be predicted from those in SAR structures, for TPs with type I and type II band structures. For some LAR asymmetric structures it was not possible to compute the Auger lifetimes, owing to the exceedingly large supercell size. The corresponding place in the table is therefore empty.

Finally, differences and similarities between LARs and SARs TPs (iv) are summarized in Table 4.3, which provides clear guidelines about when and how it is possible to predict specific properties in large, long-armed branched structures with tens of thousands of atoms based on those observed in (or theoretically calculated for) small, short-armed TPs (v). Such guidelines will be be extremely helpful for theorists performing expensive *ab-initio* modelling, who often extrapolate their results obtained for small systems with a limited number of atoms to much larger nanostructures, without a formal justification [158], [159], as well as for experimentalists trying to optimize specific properties (such as the absorption cross section, the chemical

reactivity or the catalytic efficiency) by changing the aspect ratio of their branched structures.

This chapter was published in ACS Appl. Nano Mater. 2022, 5, 12, 18986-18997

Conclusions

In this part, I have shown CdTe/CdSe core/arms TPs with specific size to be potential building blocks for photo-catalytic cells for efficient CO_2 reduction because of the following properties: 1) large absorption cross section in the visible part of the spectrum, 2) long carriers' lifetimes, 3) large expected reactant adsorption due to the large surface area rich in coordinatively unsaturated metal atoms, 4) high selectivity for CO_2 reduction vs the competing H_2O reduction, and 5) provision of eight isoenergetic electrons for the redox reaction at one time.

Next I investigated the dependence of the electronic structure, the optical spectra, and the radiative recombination times on arms' diameter and length in homogeneous CdTe TPs. I found that band edge structure, absorption onset and radiative lifetime only depend on the diameter but not the length. In contrast, Auger processes (Auger recombination and electron cooling) exhibit a marked dependence on the TP's arm length. Furthermore, owing to their large volume, these systems also have the added benefits of an increased absorption cross section (directly dependent on the volume V), decreased thresholds for optical gain and for development of amplified spontaneous emission (both inversely dependent on V), and reduced photoinduced absorption (also inversely dependent on V). These properties allow strong selective suppression of Auger processes by shape engineering alone, without affecting radiative recombination, making CdTe TPs ideally suited for applications as efficient light-emitting media.

In contrast to the last two chapters, where the TPs discussed are assumed to have an ideal structural configuration, where all the arms have equal length and diameter, in Chapter IV, CdTe/CdSe core/arms TPs and CdTe TPs with asymmetrical structure (where one of the four arms is thicker (TA) or longer (LA)) are discussed. TPs with two different aspect ratios, referred to as small aspect ratio (SAR) and large aspect ratio (LAR) respectively, of nominal arm

length over arm diameter were considered. We found that many of the properties characteristic of anisotropic TPs (apart from the emission polarization and its temperature dependence), that make them particularly suitable for specific applications, were found to originate from their peculiar charge density distribution, which, crucially, may differ in SAR and LAR structures with the same anisotropy. In particular, the degree of wave function localization found in LAR TA structures, could be exploited to enhance the electron collection efficiency in single-tetrapod devices: taking advantage of the large absorption cross section of long-armed TPs, electrons photoexcited in the other arms would be funnelled toward a single arm where type I TPs would provide fast exciton recombination for efficient light emission, whereas type II structures would ensure long electron lifetimes for applications in electronics, PV and photo-catalysis.

Future work

1) Recent development in the synthesis of branched nanostructures have allowed the growth of single-crystalline InP TPs with a uniform zinc-blende crystal structure. Considering that InP/ZnSe quantum dots have exhibited reduced Auger recombination rates and increased PL quantum yields, it would be interesting to investigate if these effects can be enhanced in InP/ZnSe TPs.

2) Another possible line of enquiry would be to continue to investigate the effects of structural anisotropy, by considering structures with:

  (i) two longer or thicker arms (also in different positions on the TP - close or opposite);

  (ii) a combination of one longer and one thicker arm (again in different positions);

  (iii) tapered arms;

  (iv) structural disorder caused by the co-existence of both sphalerite and wurtzite domains.

Appendix A

Turbo Lanczos

For calculating Eq. (1.3.21) in Part I, an $n \times n$ linear system needs to be solved for each value of ω, which is computationally very expensive for a large system with hundreds of occupied bands. The Turbo Lanczos algorithm, derived from the *Lanczos biorthogonalization algorithm* (LBOA), is introduced to solve this problem. The main idea underlying LBOA is to build a specific tridiagonal matrix, $^m T_j$, to solve Eq. (1.3.21) in Part I with only two vectors (β and γ) saving calculation cost. $^m T_j$ is the $m \times m$ tridiagonal matrix given as:

$$
{}^m T_j = \begin{pmatrix}
0 & \gamma_j^2 & & & 0 \\
\beta_j^2 & 0 & \gamma_j^3 & & \\
& \beta_j^3 & \ddots & \ddots & \\
& & \ddots & 0 & \gamma_j^m \\
0 & & & \beta_j^m & 0
\end{pmatrix} \tag{A.0.1}
$$

The elements in the matrix are two sets of vectors generated from the following LBOA recursion algorithm:

1. Set the initial pair of vectors:

   $v_j^0 = u_j^0 = 0$;

   $v_j^1 = u_j^1 = y_j$;

   $\beta_j^1 = \gamma_j^1 = 0$;

   $l = 1$.

2. Let:

$$\alpha_j^l = (u_j^l, Lv_j^l);$$

$$\overline{v} = Lv_j^l - \alpha_j^l v_j^l - \gamma_j^l v_j^{l-1};$$

$$\overline{u} = L^\dagger u_j^l - \alpha_j^l u_j^l - \beta_j^l u_j^{l-1}.$$

3. Define the new pair of vectors:

$$\beta_j^{l+1} = \sqrt{(\overline{u}, \overline{v})};$$

$$\gamma j^{l+1} = sgn(\overline{u}, \overline{v}) \times \beta_j^{l+1};$$

$$v_j^{l+1} = \overline{v}/\beta_j^{l+1};$$

$$u_j^{l+1} = \overline{u}/\gamma_j^{l+1};$$

$$l \leftarrow l + 1.$$

4. Repeat steps 2 and 3.

Then, Eq. (1.3.21) is approximated as:

$$\alpha_{ij}(\omega) \approx 4 \left({}^m z_{ij}, \left(\omega - {}^m T_j \right)^{-1} \cdot {}^m e_1 \right), \tag{A.0.2}$$

where ${}^m z_{ij} = {}^m V_j^\top \cdot x_i$ is an m-dimensional column array with ${}^m V_j = [v_j^1, v_j^2, ..., v_j^m]$ an $n \times m$ matrix whose elements are generated from the LBOA recursion described above, and x_i is the same one defined in Eq. (1.3.22) in Part I. Hence, the components of ${}^m z_{ij}$ calculated from every iteration l are written as:

$$Z_{ij}^l = (x_i, v_j^l). \tag{A.0.3}$$

With construction of ${}^m z_{ij}$ from Eq. (A.0.3), the frequency-dependent polarizability $\alpha_{ij}(\omega)$ is calculated from Eq. (A.0.2).

Appendix B

Turbo Davidson

The inner product on the right side of Eq. (1.3.20) in Part I is obtained by solving Casida's equation:

$$(\omega - \mathcal{L}) \cdot \hat{\rho}'_j(\omega) = \left[\hat{X}_j, \hat{\rho}^0\right],$$

(B.0.1)

whose eigenvalues, in the absence of external perturbations, are the excitation energies. Hence:

$$\mathcal{L} \cdot \hat{\rho}'_j(\omega) = \omega \hat{\rho}'_j(\omega).$$

(B.0.2)

The SBR of Eq. (B.0.2) is written as:

$$\hat{\rho}' \xrightarrow{\text{SBR}} \begin{pmatrix} \{q_v\} \\ \{p_v\} \end{pmatrix},$$

(B.0.3)

$$L \begin{pmatrix} \{q_v\} \\ \{p_v\} \end{pmatrix} = L \begin{pmatrix} Q \\ P \end{pmatrix} = \omega \begin{pmatrix} Q \\ P \end{pmatrix},$$

(B.0.4)

where

$$q_v(\mathbf{r}) = \frac{1}{2} \left(\tilde{\psi}'_v(\mathbf{r}, \omega) + \tilde{\psi}'^*_v(\mathbf{r}, -\omega) \right),$$

(B.0.5)

$$p_v(\mathbf{r}) = \frac{1}{2} \left(\tilde{\psi}'_v(\mathbf{r}, \omega) - \tilde{\psi}'^*_v(\mathbf{r}, -\omega) \right),$$

(B.0.6)

and $P = \{p_v\}$, $Q = \{q_v\}$. The non-Hermitian L could be forced to be Hermitian in the format of the Random-phase Approximation (RPA) Hamiltonian [160], which is generally presented

as:

$$L = \begin{pmatrix} 0 & B \\ A & 0 \end{pmatrix} \tag{B.0.7}$$

By solving Casida's equation (Eq. (B.0.4)), the oscillation frequency and eigenvectors are obtained. Based on that, the dynamical response functions are represented, and the absorption coefficient can be calculated. However, the large dimension of the operator L makes the calculation heavy. Hence, the matrix is divided into several smaller subspaces. The Turbo-Davidson algorithm is one of several subspace approaches employed to solve large Hermitian eigenproblems. Before introducing how this method works, let's define a new matrix $C \equiv AB$, where A and B are defined in Eq. (B.0.7). Combining Eq. (B.0.4) and Eq. (B.0.7) yields:

$$L \begin{pmatrix} Q \\ P \end{pmatrix} = \begin{pmatrix} 0 & B \\ A & 0 \end{pmatrix} \begin{pmatrix} Q \\ P \end{pmatrix} = \begin{pmatrix} BP \\ AQ \end{pmatrix} = \omega \begin{pmatrix} Q \\ P \end{pmatrix}. \tag{B.0.8}$$

Hence, we have

$$BP = \omega Q, \tag{B.0.9}$$

$$AQ = \omega P. \tag{B.0.10}$$

Multiplying Eq. (B.0.9) by Eq. (B.0.10) gives:

$$(BA)Q = CQ = \omega^2 Q, \tag{B.0.11}$$

$$(BA)^T P = C^T P = \omega^2 P. \tag{B.0.12}$$

Namely, Q and P are the right and left eigenvectors of C whose eigenvalue is the square of the eigenvalue of L.

The procedures based on the Turbo-Davidson algorithm for finding the eigen-triplet $k = (p, q, \omega)$ are the following:

1. Build a trial matrix $^mW = [\omega_1, \omega_2, ..., \omega_m]$ with orthonormal elements $\{\omega_m\}$, where $m = 2k$, and set $j = 1$ for initialization.

2. Do the orthonormalization:

$$^mW^{\dagger m}W = {}^mI, \tag{B.0.13}$$

where ^mI is the identity matrix with size $m \times m$.

3. Define

$$^mA = {}^mW^\dagger A {}^mW,$$

(B.0.14)

$$^mB = {}^mW^\dagger B {}^mW,$$

(B.0.15)

and do the diagonalization to get the smaller-size matrix as:

$$^mC = {}^mB {}^mA.$$

(B.0.16)

4. Solve

$$^mC^\dagger \overline{p}_i = \overline{\omega}_i^2 \overline{p}_i,$$

(B.0.17)

$$^mC \overline{q}_i = \overline{\omega}_i^2 \overline{q}_i$$

(B.0.18)

to obtain $\{p_m\}$ and $\{q_m\}$, respectively.

5. Sort the eigen-triplets $\{p_i, q_i, \omega_i^2\}$ in ascending order of $|\overline{\omega}_i - \omega_{ref}|$ to target the interior eigenvalue.

6. Define the left l_j and right r_j residuals as

$$l_j = Bp_j - (p_j, Bp_j)q_j$$

(B.0.19)

and

$$r_j = Aq_j - (q_j, Aq_j)p_j$$

(B.0.20)

respectively. If both $|l_j|$ and $|r_j|$ are less than the error ϵ, then p_j and q_j are deemed converged. Then increase j by 1 and repeat this step until $j = k$. If $|l_j|$ or $|r_j|$ is greater than ϵ, the eigen-triplets need to be updated according to:

$$[p_j, q_j, \omega_m] = \begin{cases} m \leftarrow m+1; \omega_m = Gl_j; p_j \leftarrow {}^mW\overline{p}_j, & \text{if } |l_j| > \epsilon \\ m \leftarrow m+1; \omega_m = Gr_j; q_j \leftarrow {}^mW\overline{q}_j, & \text{if } |r_j| > \epsilon \end{cases}$$

where G is defined as the preconditioner acting on $Q = \{q_v\}$, according to:

$$Gq = \{\hat{Q}\hat{g}(\varepsilon_v)q^v\}.$$

(B.0.21)

$$\hat{g}\left(\varepsilon_v\right) = \left(\text{diag}\left(\hat{H}_{KS}^0 - \epsilon_v - \omega_{ref}\right)\right)^{-1}. \tag{B.0.22}$$

Then, repeat this step with increasing j by 1 until $j = k$.

7. Repeat steps 2-6 until the first k eigen-triplets are converged.

References

[1] L. J. Bartolotti and K. Flurchick, "An introduction to density functional theory," *Rev. Comput. Chem.*, vol. 7, pp. 187–216, 2009.

[2] P. Hohenberg and W. Kohn, "Inhomogeneous electron gas," *Phys. Rev.*, vol. 136, no. 3B, B864, 1964.

[3] H. Rydberg, M. Dion, N. Jacobson, *et al.*, "Van der Waals density functional for layered structures," *Phys. Rev. Lett*, vol. 91, no. 12, p. 126 402, 2003.

[4] M. Dion, H. Rydberg, E. Schröder, D. C. Langreth, and B. I. Lundqvist, "Van der Waals density functional for general geometries," *Phys. Rev. Lett*, vol. 92, no. 24, p. 246 401, 2004.

[5] T. J. Giese and D. M. York, "Density-functional expansion methods: Evaluation of LDA, GGA, and meta-GGA functionals and different integral approximations," *J. Chem. Phys.*, vol. 133, no. 24, p. 244 107, 2010.

[6] E. Runge and E. K. Gross, "Density-functional theory for time-dependent systems," *Phys. Rev. Lett*, vol. 52, no. 12, p. 997, 1984.

[7] R. J. Bartlett, "Many-body perturbation theory and coupled cluster theory for electron correlation in molecules," *Annu. Rev. Phys. Chem.*, vol. 32, no. 1, pp. 359–401, 1981.

[8] O. B. Malcıoğlu, R. Gebauer, D. Rocca, and S. Baroni, "turboTDDFT–A code for the simulation of molecular spectra using the Liouville–Lanczos approach to time-dependent density-functional perturbation theory," *Comput. Phys. Commun.*, vol. 182, no. 8, pp. 1744–1754, 2011.

[9] X. Ge, "Seeing colors with TDDFT: theoretical modeling of the optical properties of natural dyes," Ph.D. dissertation, SISSA, 2013.

[10]   Y. Im, S. Y. Byun, J. H. Kim, *et al.*, "Recent progress in high-efficiency blue-light-emitting materials for organic light-emitting diodes," *Adv. Funct. Mater.*, vol. 27, no. 13, p. 1 603 007, 2017.

[11]   S. Kim, B. Kim, J. Lee, H. Shin, Y.-I. Park, and J. Park, "Design of fluorescent blue light-emitting materials based on analyses of chemical structures and their effects," *Mater. Sci. Eng. R Rep.*, vol. 99, pp. 1–22, 2016.

[12]   X. Yang, X. Xu, and G. Zhou, "Recent advances of the emitters for high performance deep-blue organic light-emitting diodes," *J. Mater. Chem. C*, vol. 3, no. 5, pp. 913–944, 2015.

[13]   W.-C. Chen, C.-S. Lee, and Q.-X. Tong, "Blue-emitting organic electrofluorescence materials: progress and prospective," *J. Mater. Chem. C*, vol. 3, no. 42, pp. 10 957–10 963, 2015.

[14]   M. Zhu and C. Yang, "Blue fluorescent emitters: design tactics and applications in organic light-emitting diodes," *Chem. Soc. Rev.*, vol. 42, no. 12, pp. 4963–4976, 2013.

[15]   J. Lee, H.-F. Chen, T. Batagoda, *et al.*, "Deep blue phosphorescent organic light-emitting diodes with very high brightness and efficiency," *Nat. Mater.*, vol. 15, no. 1, pp. 92–98, 2016.

[16]   J. A. Osaheni and S. A. Jenekhe, "Efficient blue luminescence of a conjugated polymer exciplex," *Macromolecules*, vol. 27, no. 3, pp. 739–742, 1994.

[17]   K. Pichler, D. Halliday, D. Bradley, P. Burn, R. Friend, and A. Holmes, "Optical spectroscopy of highly ordered poly (p-phenylene vinylene)," *J. Condens. Matter Phys.*, vol. 5, no. 38, p. 7155, 1993.

[18]   M. Day and D. Wiles, "Photochemical degradation of poly (ethylene terephthalate). II. Effect of wavelength and environment on the decomposition process," *J. Appl. Polym. Sci.*, vol. 16, no. 1, pp. 191–202, 1972.

[19]   G. Puppels, J. Olminkhof, G. Segers-Nolten, C. Otto, F. De Mul, and J. Greve, "Laser irradiation and Raman spectroscopy of single living cells and chromosomes: sample degradation occurs with 514.5 nm but not with 660 nm laser light," *Exp. Cell Res.*, vol. 195, no. 2, pp. 361–367, 1991.

[20]   K. K. Pandey, "Study of the effect of photo-irradiation on the surface chemistry of wood," *Polym. Degrad. Stab.*, vol. 90, no. 1, pp. 9–20, 2005.

[21]   S. J. Xiao, X. J. Zhao, P. P. Hu, Z. J. Chu, C. Z. Huang, and L. Zhang, "Highly photolu-
       minescent molybdenum oxide quantum dots: one-pot synthesis and application in 2,
       4, 6-trinitrotoluene determination," *ACS Appl. Mater. Interfaces*, vol. 8, no. 12, pp. 8184–
       8191, 2016.

[22]   L. Yuan, Y. Niu, R. Li, *et al.*, "Molybdenum oxide quantum dots prepared via a one-step
       stirring strategy and their application as fluorescent probes for pyrophosphate sensing
       and efficient antibacterial materials," *J. Mater. Chem. B.*, vol. 6, no. 20, pp. 3240–3245,
       2018.

[23]   A. B. Kama, R. Dessapt, H. Serier-Brault, M. Sidibe, C. A. Diop, and R. Gautier, "Stabi-
       lization of β-octamolybdate with large counterions," *J. Mol. Struct.*, vol. 1141, pp. 698–
       702, 2017.

[24]   C. Baffert, J. F. Boas, A. M. Bond, *et al.*, "Experimental and theoretical investigations of
       the sulfite-based polyoxometalate cluster redox series: α-and β-[Mo$_{18}$O$_{54}$ (SO$_3$)$_2$]$^{4-/5-/6-}$,"
       Chem. Eur. J., vol. 12, no. 33, pp. 8472–8483, 2006.

[25]   V. Gavriliuc, R. Ahumada-Lazo, S. Hardman, *et al.*, "Ultrabright, stable metal-organic
       blue quantum dots," unpublished.

[26]   T. Yamase, "Photoredox chemistry of polyoxometalates as a photocatalyst," *Catal. Surv.
       Asia.*, vol. 7, no. 4, pp. 203–217, 2003.

[27]   V. Coué, R. Dessapt, M. Bujoli-Doeuff, M. Evain, and S. Jobic, "Synthesis, characteri-
       zation, and photochromic properties of hybrid organic- inorganic materials based on
       molybdate, DABCO, and piperazine," *Inorg. Chem.*, vol. 46, no. 7, pp. 2824–2835, 2007.

[28]   J. M. Schins, M. T. Trinh, A. J. Houtepen, and L. D. Siebbeles, "Probing formally for-
       bidden optical transitions in PbSe nanocrystals by time-and energy-resolved transient
       absorption spectroscopy," *Phys. Rev. B*, vol. 80, no. 3, p. 035 323, 2009.

[29]   B. Walker, A. M. Saitta, R. Gebauer, and S. Baroni, "Efficient approach to time-dependent
       density-functional perturbation theory for optical spectroscopy," *Phys. Rev. Lett.*, vol. 96,
       no. 11, p. 113 001, 2006.

[30]   E. Bitzek, P. Koskinen, F. Gähler, M. Moseler, and P. Gumbsch, "Structural relaxation
       made simple," *Phys. Rev. Lett*, vol. 97, no. 17, p. 170 201, 2006.

[31]   S. Roorda, W. Sinke, J. Poate, *et al.*, "Structural relaxation and defect annihilation in pure
       amorphous silicon," *Phys. Rev. B*, vol. 44, no. 8, p. 3702, 1991.

[32] A. J. Bridgeman and G. Cavigliasso, "Electronic Structure of the α and β Isomers Of $[Mo_8O_{26}]^{4-}$," *Inorg. Chem.*, vol. 41, no. 13, pp. 3500–3507, 2002.

[33] P. Giannozzi, S. Baroni, N. Bonini, *et al.*, "QUANTUM ESPRESSO: a modular and open-source software project for quantum simulations of materials," *J. Condens. Matter Phys.*, vol. 21, no. 39, p. 395 502, 2009.

[34] G. Kresse and J. Hafner, "Norm-conserving and ultrasoft pseudopotentials for first-row and transition elements," *J. Phys. Condens. Matter.*, vol. 6, no. 40, p. 8245, 1994.

[35] G. Kresse and D. Joubert, "From ultrasoft pseudopotentials to the projector augmented-wave method," *Phys. Rev. B.*, vol. 59, no. 3, p. 1758, 1999.

[36] J. Perdew, K. Burke, and M. Ernzerhof, "Perdew, burke, and ernzerhof reply," *Phys. Rev. Lett.*, vol. 80, no. 4, p. 891, 1998.

[37] M. Ernzerhof and G. E. Scuseria, "Assessment of the Perdew–Burke–Ernzerhof exchange-correlation functional," *J. Chem. Phys.*, vol. 110, no. 11, pp. 5029–5036, 1999.

[38] G. J. Martyna and M. E. Tuckerman, "A reciprocal space based method for treating long range interactions in ab initio and force-field-based calculations in clusters," *J. Chem. Phys.*, vol. 110, no. 6, pp. 2810–2821, 1999.

[39] D. J. Carter and A. L. Rohl, "Noncovalent interactions in SIESTA using the vdW-DF functional: S22 benchmark and macrocyclic structures," *J. Chem. Theory Comput.*, vol. 8, no. 1, pp. 281–289, 2012.

[40] Y. Gao, L.-K. Yan, W. Guan, and Z.-M. Su, "How do transition-metal-substituted POMs modify the photoanode of dye-sensitized solar cells? A DFT study," *Inorg. Chem. Front.*, vol. 6, no. 4, pp. 969–974, 2019.

[41] L. Manna, D. J. Milliron, A. Meisel, E. C. Scher, and A. P. Alivisatos, "Controlled growth of tetrapod-branched inorganic nanocrystals," *Nat. Mater.*, vol. 2, no. 6, pp. 382–385, 2003.

[42] N. Mishra, V. Vasavi Dutt, and M. P. Arciniegas, "Recent progress on metal chalcogenide semiconductor tetrapod-shaped colloidal nanocrystals and their applications in optoelectronics," *Chem. Mater.*, vol. 31, no. 22, pp. 9216–9242, 2019.

[43] L.-W. Wang and A. Zunger, "Local-density-derived semiempirical pseudopotentials," *Phys. Rev. B*, vol. 51, no. 24, p. 17 398, 1995.

[44] M. L. Cohen and V. Heine, "The fitting of pseudopotentials to experimental data and their subsequent application," in *Solid state physics*, vol. 24, Elsevier, 1970, pp. 37–248.

[45] L.-W. Wang and A. Zunger, "Local-density-derived semiempirical pseudopotentials," *Phys. Rev. B*, vol. 51, no. 24, p. 17 398, 1995.

[46] G. Bester, "Electronic excitations in nanostructures: an empirical pseudopotential based approach," *J. Condens. Matter Phys.*, vol. 21, no. 2, p. 023 202, 2008.

[47] J. R. Chelikowsky and M. L. Cohen, "Nonlocal pseudopotential calculations for the electronic structure of eleven diamond and zinc-blende semiconductors," *Phys. Rev. B*, vol. 14, no. 2, p. 556, 1976.

[48] G. Weisz, "Band structure and Fermi surface of white tin," *Phys. Rev.*, vol. 149, no. 2, p. 504, 1966.

[49] M. S. Hybertsen and S. G. Louie, "Spin-orbit splitting in semiconductors and insulators from the ab initio pseudopotential," *Phys. Rev. B*, vol. 34, no. 4, p. 2920, 1986.

[50] A. Szabo and N. S. Ostlund, *Modern quantum chemistry: introduction to advanced electronic structure theory*. North Chelmsford: Courier Corporation, 2012.

[51] A. Franceschetti, H. Fu, L. Wang, and A. Zunger, "Many-body pseudopotential theory of excitons in InP and CdSe quantum dots," *Phys. Rev. B*, vol. 60, no. 3, p. 1819, 1999.

[52] Y. Peter and M. Cardona, *Fundamentals of semiconductors: physics and materials properties*. New York: Springer Science & Business Media, 2010.

[53] G. A. Narvaez, G. Bester, and A. Zunger, "Excitons, biexcitons, and trions in self-assembled (In, Ga) As/ GaAs quantum dots: Recombination energies, polarization, and radiative lifetimes versus dot height," *Phys. Rev. B*, vol. 72, no. 24, p. 245 318, 2005.

[54] D. Dexter, *Theory of the optical properties of imperfections in nonmetals*. New York: Elsevier, 1958, vol. 6, pp. 353–411.

[55] L.-W. Wang, M. Califano, A. Zunger, and A. Franceschetti, "Pseudopotential theory of Auger processes in CdSe quantum dots," *Phys. Rev. Lett*, vol. 91, no. 5, p. 056 404, 2003.

[56] J. Ayres, B. Forsberg, I. Annesi-Maesano, *et al.*, "Climate change and respiratory disease: European Respiratory Society position statement," *Eur. Respir. J.*, vol. 34, no. 2, pp. 295–302, 2009.

[57] "Ar5 climate change 2014:mitigation of climate change," IPCC. (2014), [Online]. Available: https://www.epa.gov/ghgemissions/global-greenhouse-gas-emissions-data.

[58] T. Boden, G. Marland, and R. Andres, "Global, regional, and national fossil-fuel CO_2 emissions. carbon dioxide information analysis center, Oak Ridge National Labora-

tory," *US Department of Energy, Oak Ridge, Tenn., USA 2009. doi 10.3334/CDIAC*, vol. 1, 2017.

[59] S. Wang, X. Han, Y. Zhang, N. Tian, T. Ma, and H. Huang, "Inside-and-out semiconductor engineering for CO_2 photoreduction: from recent advances to new trends," *Small Structures*, vol. 2, no. 1, p. 2 000 061, 2021.

[60] J. Fu, K. Jiang, X. Qiu, J. Yu, and M. Liu, "Product selectivity of photocatalytic CO_2 reduction reactions," *Mater. Today*, vol. 32, pp. 222–243, 2020.

[61] S. Xie, Q. Zhang, G. Liu, and Y. Wang, "Photocatalytic and photoelectrocatalytic reduction of CO_2 using heterogeneous catalysts with controlled nanostructures," *ChemComm*, vol. 52, no. 1, pp. 35–59, 2016.

[62] J. Jasieniak, M. Califano, and S. E. Watkins, "Size-dependent valence and conduction band-edge energies of semiconductor nanocrystals," *ACS Nano*, vol. 5, no. 7, pp. 5888–5902, 2011.

[63] D. V. Talapin, J.-S. Lee, M. V. Kovalenko, and E. V. Shevchenko, "Prospects of colloidal nanocrystals for electronic and optoelectronic applications," *Chem. Rev.*, vol. 110, no. 1, pp. 389–458, 2010.

[64] G. Li, S. Ciston, Z. V. Saponjic, *et al.*, "Synthesizing mixed-phase TiO_2 nanocomposites using a hydrothermal method for photo-oxidation and photoreduction applications," *J. Catal.*, vol. 253, no. 1, pp. 105–110, 2008.

[65] J. Zhang, Q. Xu, Z. Feng, M. Li, and C. Li, "Importance of the relationship between surface phases and photocatalytic activity of TiO_2," *Angew. Chem.*, vol. 120, no. 9, pp. 1790–1793, 2008.

[66] X. Wang, Q. Xu, M. Li, *et al.*, "Photocatalytic overall water splitting promoted by an α–β phase junction on Ga_2O_3," *Angew. Chem.*, vol. 124, no. 52, pp. 13 266–13 269, 2012.

[67] M. Grätzel, "Photoelectrochemical cells," *Nature*, vol. 414, no. 15, pp. 338–344, 2001.

[68] M. A. Fox and M. T. Dulay, "Heterogeneous photocatalysis," *Chem. Rev.*, vol. 93, no. 1, pp. 341–357, 1993.

[69] L. Kavan, M. Grätzel, S. Gilbert, C. Klemenz, and H. Scheel, "Electrochemical and photoelectrochemical investigation of single-crystal anatase," *J. Am. Chem. Soc.*, vol. 118, no. 28, pp. 6716–6723, 1996.

[70] P. Maity, O. F. Mohammed, K. Katsiev, and H. Idriss, "Study of the bulk charge carrier dynamics in anatase and rutile TiO_2 single crystals by femtosecond time-resolved spectroscopy," *J. Phys. Chem. C*, vol. 122, no. 16, pp. 8925–8932, 2018.

[71] Y. Yamada and Y. Kanemitsu, "Determination of electron and hole lifetimes of rutile and anatase TiO_2 single crystals," *Appl. Phys. Lett.*, vol. 101, no. 13, p. 133 907, 2012.

[72] "The inverse problem in material discovery: Given a target property, find the material," University of Colorado. (2015), [Online]. Available: https://www.colorado.edu/faculty/zunger-matter-by-design/inverse-design.

[73] C. Vogt, M. Monai, G. J. Kramer, and B. M. Weckhuysen, "The renaissance of the Sabatier reaction and its applications on Earth and in space," *Nat. Catal.*, vol. 2, no. 3, pp. 188–197, 2019.

[74] S. Kattel, P. Liu, and J. G. Chen, "Tuning selectivity of CO_2 hydrogenation reactions at the metal/oxide interface," *J. Am. Chem. Soc.*, vol. 139, no. 29, pp. 9739–9754, 2017.

[75] W. Tu, Y. Zhou, Q. Liu, *et al.*, "Robust hollow spheres consisting of alternating titania nanosheets and graphene nanosheets with high photocatalytic activity for CO_2 conversion into renewable fuels," *Adv. Funct. Mater.*, vol. 22, no. 6, pp. 1215–1221, 2012.

[76] T. Yui, A. Kan, C. Saitoh, K. Koike, T. Ibusuki, and O. Ishitani, "Photochemical reduction of CO_2 using TiO_2: effects of organic adsorbates on TiO_2 and deposition of Pd onto TiO_2," *ACS Appl. Mater. Interfaces.*, vol. 3, no. 7, pp. 2594–2600, 2011.

[77] A. Vasileff, C. Xu, Y. Jiao, Y. Zheng, and S.-Z. Qiao, "Surface and interface engineering in copper-based bimetallic materials for selective CO_2 electroreduction," *Chem*, vol. 4, no. 8, pp. 1809–1831, 2018.

[78] S. Xie, Y. Wang, Q. Zhang, W. Deng, and Y. Wang, "MgO-and Pt-promoted TiO_2 as an efficient photocatalyst for the preferential reduction of carbon dioxide in the presence of water," *ACS Catal.*, vol. 4, no. 10, pp. 3644–3653, 2014.

[79] K. Kočí, L. Obalová, L. Matějová, *et al.*, "Effect of TiO_2 particle size on the photocatalytic reduction of CO2," *Appl. Catal. B: Environ.*, vol. 89, no. 3-4, pp. 494–502, 2009.

[80] J. An, A. Franceschetti, S. Dudiy, and A. Zunger, "The peculiar electronic structure of PbSe quantum dots," *Nano Lett.*, vol. 6, no. 12, pp. 2728–2735, 2006.

[81] L. Manna, E. C. Scher, and A. P. Alivisatos, "Synthesis of soluble and processable rod-, arrow-, teardrop-, and tetrapod-shaped CdSe nanocrystals," *J. Am. Chem. Soc.*, vol. 122, no. 51, pp. 12 700–12 706, 2000.

[82] J. Li, "Shape effects on electronic states of nanocrystals," *Nano Lett.*, vol. 3, no. 10, pp. 1357–1363, 2003.

[83] R. Xie, U. Kolb, and T. Basché, "Design and synthesis of colloidal nanocrystal heterostructures with tetrapod morphology," *Small*, vol. 2, no. 12, pp. 1454–1457, 2006.

[84] L. Carbone, C. Nobile, M. De Giorgi, *et al.*, "Synthesis and micrometer-scale assembly of colloidal CdSe/CdS nanorods prepared by a seeded growth approach," *Nano Lett.*, vol. 7, no. 10, pp. 2942–2950, 2007.

[85] A. Fiore, R. Mastria, M. G. Lupo, *et al.*, "Tetrapod-shaped colloidal nanocrystals of II-VI semiconductors prepared by seeded growth," *J. Am. Chem. Soc.*, vol. 131, no. 6, pp. 2274–2282, 2009.

[86] D. V. Talapin, J. H. Nelson, E. V. Shevchenko, S. Aloni, B. Sadtler, and A. P. Alivisatos, "Seeded growth of highly luminescent CdSe/CdS nanoheterostructures with rod and tetrapod morphologies," *Nano Lett.*, vol. 7, no. 10, pp. 2951–2959, 2007.

[87] Y.-H. Li, A. Walsh, S. Chen, *et al.*, "Revised ab initio natural band offsets of all group IV, II-VI, and III-V semiconductors," *Appl. Phys. Lett.*, vol. 94, no. 21, p. 212 109, 2009.

[88] M. J. Enright, F. Y. Dou, S. Wu, *et al.*, "Seeded growth of nanoscale semiconductor tetrapods: generality and the role of cation exchange," *Chem. Mater.*, vol. 32, no. 11, pp. 4774–4784, 2020.

[89] R. E. Bailey and S. Nie, "Alloyed semiconductor quantum dots: tuning the optical properties without changing the particle size," *J. Am. Chem. Soc.*, vol. 125, no. 23, pp. 7100–7106, 2003.

[90] S. Link, Z. L. Wang, and M. El-Sayed, "Alloy formation of gold- silver nanoparticles and the dependence of the plasmon absorption on their composition," *J. Phys. Chem. B*, vol. 103, no. 18, pp. 3529–3533, 1999.

[91] M. P. Mallin and C. J. Murphy, "Solution-phase synthesis of sub-10 nm Au- Ag alloy nanoparticles," *Nano Lett.*, vol. 2, no. 11, pp. 1235–1237, 2002.

[92] S. Kim, B. Fisher, H.-J. Eisler, and M. Bawendi, "Type-II quantum dots: CdTe/CdSe (core/shell) and CdSe/ZnTe (core/shell) heterostructures," *J. Am. Chem. Soc.*, vol. 125, no. 38, pp. 11 466–11 467, 2003.

[93] Y. Liao, S.-W. Cao, Y. Yuan, Q. Gu, Z. Zhang, and C. Xue, "Efficient CO_2 capture and photoreduction by amine-functionalized TiO_2," *Chem. Eur. J.*, vol. 20, no. 33, pp. 10 220–10 222, 2014.

[94] D. V. Talapin, A. L. Rogach, A. Kornowski, M. Haase, and H. Weller, "Highly luminescent monodisperse CdSe and CdSe/ZnS nanocrystals synthesized in a hexadecylamine-trioctylphosphine oxide- trioctylphospine mixture," *Nano Lett.*, vol. 1, no. 4, pp. 207–211, 2001.

[95] X. Chen, Y. Zhou, Q. Liu, Z. Li, J. Liu, and Z. Zou, "Ultrathin, single-crystal WO_3 nanosheets by two-dimensional oriented attachment toward enhanced photocatalystic reduction of CO_2 into hydrocarbon fuels under visible light," *ACS Appl. Mater. Interfaces.*, vol. 4, no. 7, pp. 3372–3377, 2012.

[96] S. Feng, X. Chen, Y. Zhou, *et al.*, "$Na_2V_6O_{16}$· x H_2O nanoribbons: large-scale synthesis and visible-light photocatalytic activity of CO_2 into solar fuels," *Nanoscale*, vol. 6, no. 3, pp. 1896–1900, 2014.

[97] A. Li, T. Wang, C. Li, Z. Huang, Z. Luo, and J. Gong, "Adjusting the reduction potential of electrons by quantum confinement for selective photoreduction of CO_2 to methanol," *Angew. Chem. Int. Ed.*, vol. 58, no. 12, pp. 3804–3808, 2019.

[98] K. Ozawa, M. Emori, S. Yamamoto, *et al.*, "Electron–hole recombination time at TiO_2 single-crystal surfaces: influence of surface band bending," *J. Phys. Chem. Lett.*, vol. 5, no. 11, pp. 1953–1957, 2014.

[99] X.-F. Yang, A. Wang, B. Qiao, J. Li, J. Liu, and T. Zhang, "Single-atom catalysts: a new frontier in heterogeneous catalysis," *Acc. Chem. Res.*, vol. 46, no. 8, pp. 1740–1748, 2013.

[100] R. García-Muelas and N. López, "Statistical learning goes beyond the d-band model providing the thermochemistry of adsorbates on transition metals," *Nat. Commun.*, vol. 10, no. 1, pp. 1–7, 2019.

[101] Y. Zhao, G. Chen, T. Bian, *et al.*, "Defect-rich ultrathin ZnAl-layered double hydroxide nanosheets for efficient photoreduction of CO_2 to CO with water," *Adv. Mater.*, vol. 27, no. 47, pp. 7824–7831, 2015.

[102] V. I. Klimov, "Optical nonlinearities and ultrafast carrier dynamics in semiconductor nanocrystals," *J. Phys. Chem. B*, vol. 104, no. 26, pp. 6112–6123, 2000.

[103] N. Mishra, N. J. Orfield, F. Wang, *et al.*, "Using shape to turn off blinking for two-colour multiexciton emission in CdSe/CdS tetrapods," *Nat. Commun.*, vol. 8, no. 1, pp. 1–9, 2017.

[104] A. A. Lutich, C. Mauser, E. Da Como, *et al.*, "Multiexcitonic dual emission in CdSe/CdS tetrapods and nanorods," *Nano Lett.*, vol. 10, no. 11, pp. 4646–4650, 2010.

[105] A. Franceschetti, H. Fu, L. Wang, and A. Zunger, "Many-body pseudopotential theory of excitons in InP and CdSe quantum dots," *Phys. Rev. B*, vol. 60, no. 3, p. 1819, 1999.

[106] M. Bruchez Jr, M. Moronne, P. Gin, S. Weiss, and A. P. Alivisatos, "Semiconductor nanocrystals as fluorescent biological labels," *Science*, vol. 281, no. 5385, pp. 2013–2016, 1998.

[107] V. L. Colvin, M. C. Schlamp, and A. P. Alivisatos, "Light-emitting diodes made from cadmium selenide nanocrystals and a semiconducting polymer," *Nature*, vol. 370, no. 6488, pp. 354–357, 1994.

[108] V. Klimov, A. Mikhailovsky, S. Xu, *et al.*, "Optical gain and stimulated emission in nanocrystal quantum dots," *Science*, vol. 290, no. 5490, pp. 314–317, 2000.

[109] M. V. Kovalenko, L. Manna, A. Cabot, *et al.*, "Prospects of nanoscience with nanocrystals," *ACS Nano*, vol. 9, no. 2, pp. 1012–1057, 2015.

[110] C. R. Kagan, E. Lifshitz, E. H. Sargent, and D. V. Talapin, "Building devices from colloidal quantum dots," *Science*, vol. 353, no. 6302, aac5523, 2016.

[111] C. Murray, D. J. Norris, and M. G. Bawendi, "Synthesis and characterization of nearly monodisperse CdE (E= sulfur, selenium, tellurium) semiconductor nanocrystallites," *J. Am. Chem. Soc.*, vol. 115, no. 19, pp. 8706–8715, 1993.

[112] A. L. Rogach, T. Franzl, T. A. Klar, *et al.*, "Aqueous synthesis of thiol-capped CdTe nanocrystals: state-of-the-art," *J. Phys. Chem. C*, vol. 111, no. 40, pp. 14 628–14 637, 2007.

[113] A. B. Greytak, P. M. Allen, W. Liu, *et al.*, "Alternating layer addition approach to CdSe/CdS core/shell quantum dots with near-unity quantum yield and high on-time fractions," *Chem. Sci.*, vol. 3, no. 6, pp. 2028–2034, 2012.

[114] D. Chepic, A. L. Efros, A. I. Ekimov, *et al.*, "Auger ionization of semiconductor quantum drops in a glass matrix," *J. Lumin.*, vol. 47, no. 3, pp. 113–127, 1990.

[115] M. Nirmal, B. O. Dabbousi, M. G. Bawendi, *et al.*, "Fluorescence intermittency in single cadmium selenide nanocrystals," *Nature*, vol. 383, no. 6603, pp. 802–804, 1996.

[116] I. Vurgaftman and J. Singh, "Effect of spectral broadening and electron-hole scattering on carrier relaxation in GaAs quantum dots," *Appl. Phys. Lett.*, vol. 64, no. 2, pp. 232–234, 1994.

[117] Z. Deng, K. S. Jeong, and P. Guyot-Sionnest, "Colloidal quantum dots intraband photodetectors," *ACS Nano*, vol. 8, no. 11, pp. 11 707–11 714, 2014.

[118] W. A. Tisdale, K. J. Williams, B. A. Timp, D. J. Norris, E. S. Aydil, and X.-Y. Zhu, "Hot-electron transfer from semiconductor nanocrystals," *Science*, vol. 328, no. 5985, pp. 1543–1547, 2010.

[119] H. Htoon, J. Hollingsworth, R. Dickerson, and V. Klimov, "Effect of zero-to one-dimensional transformation on multiparticle auger recombination in semiconductor quantum rods," *Phys. Rev. Lett*, vol. 91, no. 22, p. 227 401, 2003.

[120] M. Zavelani-Rossi, M. G. Lupo, F. Tassone, L. Manna, and G. Lanzani, "Suppression of biexciton Auger recombination in CdSe/CdS dot/rods: role of the electronic structure in the carrier dynamics," *Nano Lett.*, vol. 10, no. 8, pp. 3142–3150, 2010.

[121] P. Spinicelli, S. Buil, X. Quelin, B. Mahler, B. Dubertret, and J.-P. Hermier, "Bright and grey states in CdSe-CdS nanocrystals exhibiting strongly reduced blinking," *Phys. Rev. Lett*, vol. 102, no. 13, p. 136 801, 2009.

[122] J. Vela, H. Htoon, Y. Chen, *et al.*, "Effect of shell thickness and composition on blinking suppression and the blinking mechanism in 'giant' CdSe/CdS nanocrystal quantum dots," *J. Biophotonics*, vol. 3, no. 10-11, pp. 706–717, 2010.

[123] D. Oron, M. Kazes, and U. Banin, "Multiexcitons in type-II colloidal semiconductor quantum dots," *Phys. Rev. B*, vol. 75, no. 3, p. 035 330, 2007.

[124] J. P. Philbin and E. Rabani, "Auger recombination lifetime scaling for type I and quasi-type II core/shell quantum dots," *J. Phys. Chem. Lett.*, vol. 11, no. 13, pp. 5132–5138, 2020.

[125] Y. Chen, J. Vela, H. Htoon, *et al.*, ""Giant" multishell CdSe nanocrystal quantum dots with suppressed blinking," *J. Am. Chem. Soc.*, vol. 130, no. 15, pp. 5026–5027, 2008.

[126] M. Califano, "Suppression of Auger recombination in nanocrystals via ligand-assisted wave function engineering in reciprocal space," *J. Phys. Chem. Lett.*, vol. 9, no. 8, pp. 2098–2104, 2018.

[127] J. Müller, J. Lupton, P. Lagoudakis, *et al.*, "Wave function engineering in elongated semiconductor nanocrystals with heterogeneous carrier confinement," *Nano Lett.*, vol. 5, no. 10, pp. 2044–2049, 2005.

[128] S. Malkmus, S. Kudera, L. Manna, W. J. Parak, and M. Braun, "Electron- Hole Dynamics in CdTe Tetrapods," *J. Phys. Chem. B*, vol. 110, no. 35, pp. 17 334–17 338, 2006.

[129] D. Tarì, M. De Giorgi, F. D. Sala, *et al.*, "Optical properties of tetrapod-shaped CdTe nanocrystals," *Appl. Phys. Lett.*, vol. 87, no. 22, p. 224 101, 2005.

[130] L. Fang, J. Y. Park, Y. Cui, *et al.*, "Mechanical and electrical properties of CdTe tetrapods studied by atomic force microscopy," *J. Chem. Phys.*, vol. 127, no. 18, p. 184 704, 2007.

[131] D. Katz, T. Wizansky, O. Millo, E. Rothenberg, T. Mokari, and U. Banin, "Size-dependent tunneling and optical spectroscopy of CdSe quantum rods," *Phys. Rev. Lett*, vol. 89, no. 8, p. 086 801, 2002.

[132] J. Hu, L.-W. Wang, L.-S. Li, W. Yang, and A. P. Alivisatos, "Semiempirical pseudopotential calculation of electronic states of CdSe quantum rods," *J. Phys. Chem. B*, vol. 106, no. 10, pp. 2447–2452, 2002.

[133] V. I. Klimov, A. A. Mikhailovsky, D. McBranch, C. A. Leatherdale, and M. G. Bawendi, "Quantization of multiparticle Auger rates in semiconductor quantum dots," *Science*, vol. 287, no. 5455, pp. 1011–1013, 2000.

[134] A. Pandey and P. Guyot-Sionnest, "Multicarrier recombination in colloidal quantum dots," *J. Chem. Phys.*, vol. 127, no. 11, p. 111 104, 2007.

[135] V. Klimov, J. McGuire, R. Schaller, and V. Rupasov, "Scaling of multiexciton lifetimes in semiconductor nanocrystals," *Phys. Rev. B*, vol. 77, no. 19, p. 195 324, 2008.

[136] I. Robel, R. Gresback, U. Kortshagen, R. D. Schaller, and V. I. Klimov, "Universal size-dependent trend in Auger recombination in direct-gap and indirect-gap semiconductor nanocrystals," *Phys. Rev. Lett*, vol. 102, no. 17, p. 177 404, 2009.

[137] C. Melnychuk and P. Guyot-Sionnest, "Slow Auger relaxation in HgTe colloidal quantum dots," *J. Phys. Chem. Lett.*, vol. 9, no. 9, pp. 2208–2211, 2018.

[138] J. A. Castaneda, G. Nagamine, E. Yassitepe, *et al.*, "Efficient biexciton interaction in perovskite quantum dots under weak and strong confinement," *ACS Nano*, vol. 10, no. 9, pp. 8603–8609, 2016.

[139] Y. Li, T. Ding, X. Luo, Y. Tian, X. Lu, and K. Wu, "Synthesis and spectroscopy of monodispersed, quantum-confined FAPbBr3 perovskite nanocrystals," *Chem. Mater.*, vol. 32, no. 1, pp. 549–556, 2019.

[140] Y. Kobayashi, L. Pan, and N. Tamai, "Effects of size and capping reagents on biexciton auger recombination dynamics of CdTe quantum dots," *J. Phys. Chem. C*, vol. 113, no. 27, pp. 11 783–11 789, 2009.

[141] H. Htoon, J. Hollingworth, A. Malko, R. Dickerson, and V. Klimov, "Light amplification in semiconductor nanocrystals: Quantum rods versus quantum dots," *Appl. Phys. Lett.*, vol. 82, no. 26, pp. 4776–4778, 2003.

[142] C. Melnychuk and P. Guyot-Sionnest, "Multicarrier dynamics in quantum dots," *Chem. Rev.*, vol. 121, no. 4, pp. 2325–2372, 2021.

[143] V. I. Klimov, *Semiconductor and metal nanocrystals: synthesis and electronic and optical properties*. New York: CRC Press, 2003.

[144] B. Kim, K. Kim, Y. Kwon, *et al.*, "CuInS2/CdS-heterostructured nanotetrapods by seeded growth and their photovoltaic properties," *ACS Appl. Nano Mater.*, vol. 1, no. 6, pp. 2449–2454, 2018.

[145] W.-Y. Wu, M. Li, J. Lian, *et al.*, "Efficient color-tunable multiexcitonic dual wavelength emission from type II semiconductor tetrapods," *ACS Nano*, vol. 8, no. 9, pp. 9349–9357, 2014.

[146] T. Mokari, E. Rothenberg, I. Popov, R. Costi, and U. Banin, "Selective growth of metal tips onto semiconductor quantum rods and tetrapods," *Science*, vol. 304, no. 5678, pp. 1787–1790, 2004.

[147] M. Samadi Khoshkhoo, P. Zhang, K. Hiekel, *et al.*, "Semiconductor Nanocrystal Heterostructures: Near-Infrared Emitting PbSe-Tipped CdSe Tetrapods," *Chem. Mater.*, vol. 32, no. 9, pp. 4045–4053, 2020.

[148] X. Wang, S. Chen, S. Thota, *et al.*, "Anisotropic arm growth in unconventional semiconductor CdSe/CdS nanotetrapod synthesis using core/shell CdSe/CdS as seeds," *J. Phys. Chem. C*, vol. 123, no. 31, pp. 19 238–19 245, 2019.

[149] C. Mauser, T. Limmer, E. Da Como, *et al.*, "Anisotropic optical emission of single CdSe/CdS tetrapod heterostructures: Evidence for a wavefunction symmetry breaking," *Phys. Rev. B*, vol. 77, no. 15, p. 153 303, 2008.

[150] Q. Pang, L. Zhao, Y. Cai, *et al.*, "CdSe nano-tetrapods: controllable synthesis, structure analysis, and electronic and optical properties," *Chem. Mater.*, vol. 17, no. 21, pp. 5263–5267, 2005.

[151] N. Mishra, W.-Y. Wu, B. M. Srinivasan, R. Hariharaputran, Y.-W. Zhang, and Y. Chan, "Continuous shape tuning of nanotetrapods: Toward shape-mediated self-assembly," *Chem. Mater.*, vol. 28, no. 4, pp. 1187–1195, 2016.

[152] M. Califano and Y. Zhou, "Inverse-designed semiconductor nanocatalysts for targeted CO_2 reduction in water," *Nanoscale*, vol. 13, no. 22, pp. 10 024–10 034, 2021.

[153] M. Califano, A. Franceschetti, and A. Zunger, "Temperature dependence of excitonic radiative decay in CdSe quantum dots: the role of surface hole traps," *Nano Lett.*, vol. 5, no. 12, pp. 2360–2364, 2005.

[154] M. Califano, A. Franceschetti, and A. Zunger, "Lifetime and polarization of the radiative decay of excitons, biexcitons, and trions in CdSe nanocrystal quantum dots," *Phys. Rev. B*, vol. 75, no. 11, p. 115 401, 2007.

[155] L. Wang, Y. Tian, T. Okuhata, and N. Tamai, "Charge transfer dynamics and Auger recombination of CdTe/CdS core/shell quantum dots," *J. Phys. Chem. C*, vol. 119, no. 31, pp. 17 971–17 978, 2015.

[156] M. Califano, "Electron Relaxation Following UV Excitation in CdSe Nanocrystals: Sub-Picosecond-Fast Population of the 1 P States Across a Gap Wider Than 10 Phonon Energies," *J. Phys. Chem. C*, vol. 113, no. 46, pp. 19 859–19 862, 2009.

[157] J. Hu, L.-S. Li, W. Yang, L. Manna, L.-W. Wang, and A. P. Alivisatos, "Linearly polarized emission from colloidal semiconductor quantum rods," *Science*, vol. 292, no. 5524, pp. 2060–2063, 2001.

[158] M. Voros, G. Galli, and G. T. Zimanyi, "Colloidal nanoparticles for intermediate band solar cells," *ACS Nano*, vol. 9, no. 7, pp. 6882–6890, 2015.

[159] M. Rusishvili, S. Wippermann, D. V. Talapin, and G. Galli, "Stoichiometry of the core determines the electronic structure of core–shell III–V/II–VI nanoparticles," *Chem. Mater.*, vol. 32, no. 22, pp. 9798–9804, 2020.

[160] D. J. Thouless, "Stability conditions and nuclear rotations in the Hartree-Fock theory," *Nucl. Phys.*, vol. 21, pp. 225–232, 1960.